CHALMERS

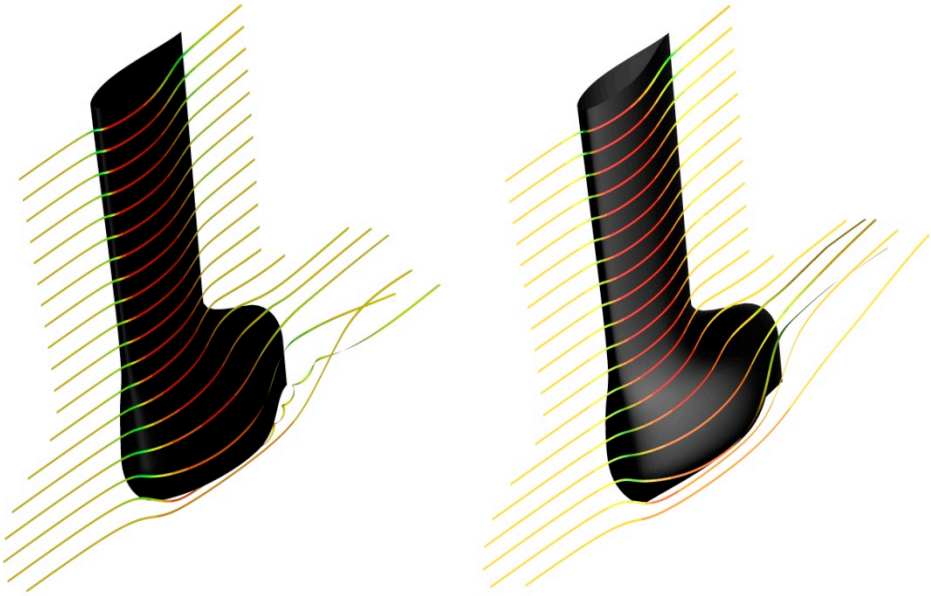

Shape optimisation of an integrated bulb-keel

Thesis subtitle

Master of Science Thesis

KASPER LJUNGQVIST

Department of Shipping and Marine Technology
Division of Ship Design
CHALMERS UNIVERSITY OF TECHNOLOGY
Gothenburg, Sweden, 2011
Report No. X-11/268

A THESIS FOR THE DEGREE OF MASTER OF SCIENCE

Shape optimisation of an integrated bulb-keel

Thesis subtitle

KASPER LJUNGQVIST

Department of Shipping and Marine Technology
CHALMERS UNIVERSITY OF TECHNOLOGY
Gothenburg, Sweden 2011

Shape optimisation of an integrated bulb-keel

Thesis subtitle

KASPER LJUNGQVIST

Report No. X-11/268

[1]Chalmers University of Technology
SE-412 96 Gothenburg
Sweden
Telephone +46 (0)31-772 1000

Printed by Chalmers Reproservice
Gothenburg, Sweden, 2011

Shape optimisation of an integrated bulb-keel
Thesis subtitle

KASPER LJUNGQVIST
Department of Shipping and Marine Technology
Division of Ship Design
Chalmers University of Technology

Abstract:

The objective of the thesis was to shape optimise an integrated bulb-keel using a numerical optimisation method and to validate how well the used methods suit this kind of problem. The algorithm used for the optimisation was a Non-dominated Sorting Genetic Algorithm, NSGA-II. The optimisation was limited to the bulb part of the keel and 7 design variables were used together with 4 inequality constraints. The hydrodynamic performance of the keel was evaluated using a RANS viscous solver and the objective function used in the optimisation was the ratio of drag coefficient over lift coefficient CD/CL.

The numerical CFD calculations were validated with experimental wind tunnel tests, which is a crucial part when investigating new types of numerical flow problems. The CFD calculations were also verified using a Least Square Root method in order to obtain the numerical error. The comparison between the wind tunnel results and the CFD results showed that the CL/CD-ratio was predicted very similarly for the numerical and experimental tests.

The optimised keel design had a CD/CL-ratio improvement of around 4% compared to the initial keel design. Finally the keels were mounted on a hull of a 40-foot yacht and tested in a velocity prediction program (VPP) in order to get a more understandable performance indicator of the keels.

Keywords: Keel, Bulb, NSGA-II, Optimisation, CFD, RANS, Integrated bulb-keel

Preface

The thesis was carried out at Chalmers University of Technology in Gothenburg, Sweden, in cooperation with Aalto University, School of Science and Technology in Espoo, Finland. The thesis has therefore been published from both Universities.

I would like to acknoledge some people who have been helping me throughout the thesis. Firstly I would like to like to express great gratitude to my examiner at Chalmers University of Technology Professor Lars Larsson for letting me carry out my thesis at Chalmers University of Technology even if I was not registered at the master's program. I would also like to thank him for all his input in my work and his great knowledge in hydrodynamics and yacht design.

Secondly I would like to thank my supervisors Master of Science (Tech.) Florian Vesting and Master of Science (Tech.) Michał Orych. Florian's knowledge in the Friendship System and in optimisation and Michal's knowledge in both CFD and yacht design have been have helped me a lot in throughout the thesis.

Further I would like to thank supervisor at Aalto University Professor Jerzy Matusiak for being so flexible and letting me carry out the thesis at another university. He has also been very supportive throughout the project with both help concerning hydrodynamic issues but also with practical issues

Finally I would like to thank my fellow students Björn Axfors and Hanna Tunander for the help in the wind tunnel and interchange of ideas, Friendship Framework's software engineer Arne Bergmann for software support, Tommi Mikkola for improvement suggestions and Lotta Olsson for the help with all practical arrangements.

Gothenburg, August, 2011
Kasper Ljungqvist

Contents

Nomenclature

Symbols

A	Cross-section area of a control volume
AR	Aspect ratio
AR_e	Effective aspect ratio
B	Centre of buoyancy
BG	Distance between B and G
BM	Metacentric radius
C	Mean chord length, Cross sectional area of wind tunnel
C_1	Root chord length
C_2	Tip chord length
C_D	Drag coefficient
C_{Di}	Induced drag coefficient
C_{D0}	Profile drag coefficient, Drag coefficient at zero degrees leeway
C_f	Local skin friction coefficient
C_F	Total skin friction coefficient
C_L	Lift coefficient
D	Drag force, Experimental solution
D_f	Friction drag
D_i	Induced drag
D_0	Form drag
E	Validation comparison error
F_s	Safety factor for numerical uncertainty
$F_{x,y,z}$	Body force in x-, y- and z-direction
Fx	Force in x-direction
Fx_p	Pressure force in x-direction
Fx_f	Frictional force in x-direction
Fy	Force in y-direction
Fy_p	Pressure force in y-direction
Fy_f	Frictional force in y-direction
F(X)	Objective function
G	Centre of gravity

g	Acceleration of gravity
GM	Metacentric height
GZ	Righting arm
h_1	Typical cell size for the finest grid
h_i	Typical cell size
I_T	Transverse moment of inertia
k	Turbulent kinetic energy, blockage factor
L	Characteristic length, Lift force
LCG	Longitudinal centre of gravity
L_{OA}	Length over all
L_{WL}	Length water line
M	Metacentre
m	Mass
n_g	Number of grids
N_{cells}	Number of grid cells
P	Distance metric
p	Pressure
p_a	Atmospheric pressure
p_{RE}	Observer order of accuracy
p_{th}	Theoretical order of accuracy
p_∞	Undisturbed pressure
R	Convergence ratio
R_{ij}	Reynolds stress tensor
RM	Righting moment
R_n	Reynolds number
r	Refinement ratio
S	Planform area
SA	Sail area
S_{ij}	Rate of strain tensor
S_W	Wetted surface area
T	Span
T_e	Effective span
T_K	Keel span

t	Time
TR	Taper ratio
u	Time averaged flow velocity component in x-direction
u_τ	Friction velocity
$\mathbf{U}$	Free stream velocity
U_ϕ	Numerical uncertainty
U_D	Experimental uncertainty
U_G	Grid discretization uncertainty
U_i	Instantaneous velocity component in i:th direction
U_I	Iterative uncertainty
U_{input}	Parameter uncertainty
U_j	Instantaneous velocity component in j:th direction
U_n	Flow velocity's normal component to a surface
U_S	Standard deviation of the numerical uncertainty's curve fit
$\mathbf{V}$	Ship velocity
$\mathbf{v}$	Flow velocity
v	Time averaged flow velocity component in y-direction
v_n	Normal velocity
$v_{particle}$	Particle velocity
VCG_{keel}	Vertical centre of gravity for the keel (from the root chord)
w	Time averaged flow velocity component in z-direction
W_{ij}	Rotation rate
X	Design variable vector
y^+	Nondimensional wall distance

Greek symbols

α	A constant for estimating the discretization error
β^*	Modelling constant
Γ	Diffusion coefficient
ρ	Density
Δ_x	Grid spacing
δ_{ij}	Kronecker delta
δ_{RE}	Discretization error

ε_{sb}	Solid blockage correction
ε_{wb}	Wake blockage correction
μ	Dynamic viscosity
μ_t	Turbulent viscosity
ν	Kinematic viscosity
ξ_B	Parameter direction crossing the boundary
ρ	Density
σ_{ij}	Stress tensor
τ_w	Wall shear stress
φ	Heel angle
ϕ	Dependent variable
Φ_B	Distance function
Φ_{exact}	Exact solution
Φ_i	Integral of local quantity
Φ_o	Estimated exact solution
ω	Specific rate of dissipation of turbulent energy
∇	Volumetric displacement

Abbreviations

CAD	Computer-Aided Design
CFD	Computational Fluid Dynamics
EASM	Explicit Algebraic Stress Model
FEM	Finite Element Method
FDM	Finite Difference Method
FS	Factory of Safety
FVM	Finite Volume Method
GA	Genetic Algorithm
ITTC	International Towing Tank Conference
LSR	Least Square Root
NACA	National Advisory Committee for Aeronautics
NSGA-II	Non-dominated Sorting Genetic Algorithm II
RANS	Reynolds Average Navier-Stokes
VPP	Velocity Prediction Program

1. Introduction

1.1 Background

Yacht design has for long been more of an experience knowledge than an actual science. Little advanced research has been made compared to naval architecture for large ships. Keels, rudders and other parts of the yacht have often been selected based on experience and rules of thumb and the calculations have been more approximations than in depth analysis. It has mostly been racing yacht projects with large budgets that have been able to use advanced design tools in their analysis. Little of the results have been published for the public due to the rivalry between the racing teams. However, in the last years more research has been conducted in yacht design and the cruising yacht industry has become more involved in the academic research field. Computational Fluid Dynamics (CFD) has also become a more accepted method for hydrodynamic calculations mainly in the ship industry but it has slowly also become more accepted in the sailing yacht industry.

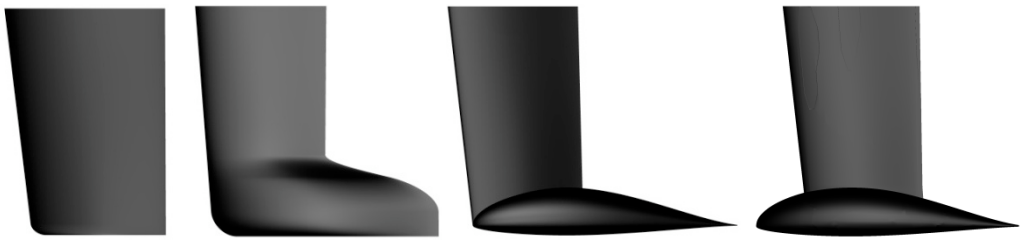

Figure 1.1 The 4 different keels used in the bachelor thesis. The fin keel, the integrated bulb-keel, the L-bulb keel and the T-bulb keel [1]

In the spring of 2010 Bergman et al. [1] carried out a bachelor thesis project at Chalmers University of Technology. In their thesis "Investigation of keel bulbs for sailing yachts" the students compared with CFD calculations the hydrodynamic performance of 4 different sailing yacht keels. The keels chosen in the investigation were 4 commonly used keel types (see Figure 1.1), a conventional fin keel, an integrated bulb-keel, an L-bulb keel and a T-bulb keel. The interested reader is directed to reference [1] for the complete description of all keels.

The conclusion from the thesis was that the integrated bulb-keel had the best hydrodynamic performance of the 3 bulb keels; the fin keel had the best performance but it cannot provide the same righting moment as the bulb keels if all keels were made out of the same material. The keels were designed in a CAD program together with professional yacht designer Stefan Qviberg. Even if the keel types used in the investigation have been commonly used, little knowledge exists about their optimum shape. Hence the interest in optimising the keels evoked the idea of this thesis. It would be very interesting to optimise all the keels but due to time limitation and work load only one keel could be chosen. The integrated bulb-keel was chosen based on the results from the bachelor thesis and this keel is a very convenient choice even if the results have been questioned by Axfors & Tunander [2]. An integrated bulb-keel is practical because of its robustness, which makes the keel more impact resistant and less risk of getting items tangled up around it.

Bergman et al. used the same CFD solver as the one that has been used in thesis, however the grid generator and the grid structure were different.

This thesis is divided into 7 chapters. First the introduction of the whole thesis will be presented together with the objective, methodology and limitation of the work. The theories behind the thesis are introduced in the second chapter followed by the investigated cases in chapter 3, where all the configurations for the calculations will be presented together with the setup of the wind tunnel. In chapter 4 the results from the calculations and from the experimental test of the wind tunnel are displayed and the discussion is carried out in chapter 5. Finally a summary of the thesis is presented in chapter 6 and the thesis is finished by some recommendations from the author for future study.

1.2 Objective of the investigation

The major aim of this thesis is to optimise the shape of a particular integrated bulb-keel. In this particular case shape optimisation means to improve the keels lifting force while decreasing its drag and maintaining a sufficient righting moment.

Another objective of the thesis is to validate the numerical methods used in the process. The calculations are validated with experimental wind tunnel tests. Additionally an objective is to investigate whether the optimisation method used is sufficient for the problem of the thesis with the set limitations and constraints.

1.3 Methodology

The CFD solver that has been used is in this thesis is SHIPFLOW 4.4.04 and more specifically XCHAP, which is method for solving the Reynolds Average Navier-Stokes equations. XCHAP is using a finite volume method as discretization method and an EASM turbulence model has been implemented.

Two methods have been used for the uncertainty analysis namely the Factor of Safety method and the Least Square Root method and the results have been compared and validated.

A tool called Friendship Framework has been used for the optimisation. Friendship Framework integrates a number of useful computer programs needed in hydrodynamic optimisation. In this thesis, Friendship Framework's CAD tool, generic integration tool and optimisation tool were used together with the integration of SHIPFLOW 4.4.04. The Non-dominated Sorting Genetic Algorithm-II (NSGA-II) was used for the optimisation algorithm.

A velocity prediction program VPP has been used in order to get a more understandable performance indicator of the keels. The velocity prediction program takes also the stability aspect of the keels into account. WinDesign VPP developed by the Wolfson Unit was the chosen velocity prediction program for this thesis.

Validation of results is a very important process when numerical calculations are carried out. Therefore wind tunnel tests were carried out in order to validate the CFD results calculated with SHIPFLOW. The wind tunnel tests were performed in the wind tunnel at the Department of Applied Mechanics at Chalmers University of Technology in Gothenburg, Sweden.

1.4 Limitations

In order to increase the quality of the thesis and to fulfil the requirements set for the thesis some limitations have been set.

1) The optimisation will be done for one angle of attack, since it would require too much computational effort to take more angles of attack into account.
2) The heeling angle was set to zero in both the numerical tests and in the experimental tests.
3) The fin part of the keel was not optimised in the optimisation process, since the optimisation was limited to the bulb part of the keel. The bulb was the part that was the focus in this thesis, although a global optimisation would be interesting.
4) Neither the strength aspect of the keels nor the manufacturing possibilities have been taken into account when designing the keels.

2. Theory

The theory of a yacht keel and the bulb will be presented in this chapter, together with optimisation theory and the computational hydrodynamics that has been used are explained.

2.1 Introduction

In this section the theory of the keel and the bulb will be presented. The hydrodynamic phenomena that occur around the keel will be introduced together with the stability aspects of the keel.

The keel on a sailing yacht has two major tasks. The first one is to provide sufficient stability when the boat heels and the second one to counteract the aerodynamic force of the sail. The hydrodynamic force that counteracts the aerodynamic force is called lift L and it is developed by the pressure difference on the keel, the rudder and the hull. However the keel is the biggest contributor to the lift force in most cases. When a yacht sails upwind it will drift sideways due to the wind. Thus the yacht moves in a direction different from the longitudinal direction of the hull and the angle between the two directions is called leeway angle. The pressure difference on the keel is caused by the leeway angle. The keel will also develop a resistance component, which is called drag D [3]. The lift and drag forces will be explained in more detail in section 2.1.1.

A sailing yacht has a significant difference compared to other seagoing vessels, since it heels considerably more. The reason for the large heel is the aerodynamic force acting on the sails of the boat. The aerodynamic force heels the boat over and this heeling moment has to be counteracted. Thus a righting moment RM is required. The righting moment is defined according to Rossell & Chapman in Principles of Naval Architecture [4] with equation (2.1), where m is the mass of the yacht, g the acceleration of gravity and GZ the righting arm. Equation (2.2) and (2.4) are also taken from Principles of Naval Architecture [4]. The righting arm is the distance between the centre of gravity of the boat G and the Z point in Figure 2.1.

$$\overline{RM} = m * g * \overline{GZ} \tag{2.1}$$

The righting arm (2.2) is dependent on the heel angle φ and on the metacentric height GM. The metacentric height is the distance between the centre of gravity and the metacentre M, see Figure 2.1, and it is also a measurement of the initial stability of the boat. Equation (2.2) is only valid for small heel angles for floating bodies that do not have circular or spherical cross-sections [4]. However, the curve for the righting arm for most sailing yachts follows a sinusoidal path longer than the curve for large ships, because of the rounder transversal cross-section of the sailing yachts. Hence the equation is valid for larger angles of attack for most sailing yachts.

$$\overline{GZ} = \overline{GM} * \sin\varphi \tag{2.2}$$

The metacentre is dependent on the shape of the hull and a high metacentre will give a high form stability. The exact formulation of the metacentric height can be seen in

equation (2.3), where BM is the distance between the metacentre and the centre of buoyancy and BG is the distance between the centre of gravity and centre of buoyancy B. BM is called the metacentric radius and is calculated with equation (2.4), where I_T is the transverse moment of inertia of the water plane and ∇ is the volumetric displacement. The centre of buoyancy B will move to B' when the boat heels and the buoyancy force will act at B', see Figure 2.1.

$$\overline{GM} = \overline{BM} - \overline{BG} \tag{2.3}$$

$$\overline{BM} = \frac{I_T}{\nabla} \tag{2.4}$$

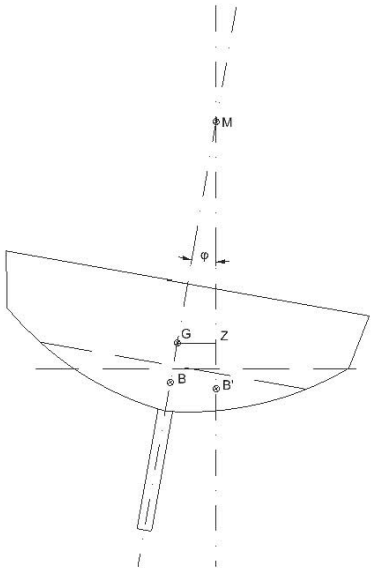

Figure 2.1 Transverse stability [3]

The stability of the yacht can be increased by increasing the height of the metacentre or by lowering the centre of gravity. The metacentre can be difficult to move since it depends on the hull shape. Hence, a more convenient way of increasing the GM value is to lower the centre of gravity. The keel has a significant role of the yacht's stability since it is has its centre of gravity very low. Therefore the keel is often made of material with high density in order to have a higher effect on the total centre of gravity. The total centre of gravity can further be lowered if a bulb is mounted on the keel [3].

2.1.1 Lift and drag

A keel can be seen as a wing and the fundamental aerodynamic theories can be applied. The lift is caused by the pressure difference on the keel as described above. Larsson & Eliasson [3] explain that when the flow meets the keel at an angle of attack (leeway angle) the flow becomes asymmetric over the keel. The point where the flow meets the keel is called the stagnation point and the velocity is zero at that point. The flow separates into two directions from that point, some of the flow flows around the upper side (suction side) of the wing (see Figure 2.2) and the rest of the flow follows the lower side (pressure side). The flow on the suction side is faster

than the flow on the pressure side and a higher velocity gives a lower pressure and a lower velocity gives a higher pressure respectively. Therefore the pressure difference is developed and the lift force L is created. The direction of the lift force is perpendicular to the flow direction. The lift force can be nondimensionalized with equation (2.5), where C_L is the lift coefficient, U the velocity of the flow, ρ the density of the fluid and S is the planform area according to Abbot & von Doenhoff [5].

$$C_L = \frac{L}{0.5*\rho*U^2*S} \tag{2.5}$$

The planform area is taken as mean chord length multiplied by the keel span.

The resistance of the keel can be divided into three components, the induced drag D_i, the form drag D_0 and the frictional resistance D_F. The induced drag is dependent on the pressure difference together with the aspect ratio. The form drag is an effect of the shape of the keel and the frictional resistance is caused by the friction between the keel and the water.

According to Larsson & Eliasson [3] the pressure difference, which is caused by the leeway angle, makes the flow move from the pressure side to the suction side around the tip and this creates a slight upward flow on the suction side and a slight downward flow on the pressure side. The upward and downward flow are strongest close to the tip and weakest at the root. When the flow from the pressure and section side meet at the trailing edge they will have different directions due to the upward and downward flows and this will create vortices, which will be strongest close to the tip because the vertical motions are strongest in that area. All vortices merge into one big vortex, which has a lot of rotational energy. The rotational energy corresponds to the induced resistance for the keel. The drag D is nondimensionalized in the same way as the lift and the drag coefficient C_D is given by equation (2.6) according to reference [5].

$$C_D = \frac{D}{0.5*\rho*U^2*S} \tag{2.6}$$

The lift and the drag are dependent on the planform of the keel. The main parameters for a keel planform are the aspect ratio AR, the taper ratio TR and the sweep angle (the sweep angle for the 25% chord). The aspect ratio is defined by equation (2.7) according to Abbot & von Doenhoff [5] and the efficiency of the keel is very dependent on the aspect ratio. T_K is the span of the keel and S is the planform area.

$$AR = \frac{{T_K}^2}{S} \tag{2.7}$$

The taper ratio on the other hand is the ratio between the length of the root chord C_1 and the tip chord C_2 [3].

$$TR = \frac{C_2}{C_1} \tag{2.8}$$

An elliptical force distribution over a wing is the optimal one (Abbot & von Doenhoff [5]). A keel with an elliptical force distribution over the span will have an effective aspect ratio AR_e which is equal to the geometrical aspect ratio defined in

equation (2.7), any force distribution that differs from an elliptical will have a decreased effective aspect ratio. The location of the trailing vortex left behind the keel has an effect on the effective aspect ratio, since a higher vortex will decrease the effective aspect ratio. Thus the effective aspect ratio is ruled by the vortex and not the geometrical span of the keel. However the keel depth will have an effect on the vortex. The effective keel depth, which is dependent on the effective aspect ratio, can be calculated with equation (2.9) according to reference [6]

$$T_e = \sqrt{\frac{AR_e * S}{2}} \tag{2.9}$$

The effective aspect ratio is further calculated with equation (2.10), where C_{Di} is the induced drag.

$$AR_e = \frac{C_L^2}{\pi * C_{Di}} \tag{2.10}$$

The tip of the keel (on a fin keel) has also an effect on the efficiency of the keel. Different shapes of the tip have an effect on the location of the trailing vortex. The best tip shape is a square tip according to Larsson & Eliasson [3]. The square tip moves the vortex below the tip due to the sharp edge, thus the flow that is created around the tip separates quite early. Compared to a rounded tip that allows the flow to move around the tip and this will cause the flow to separate above the tip and decrease the effective aspect ratio.

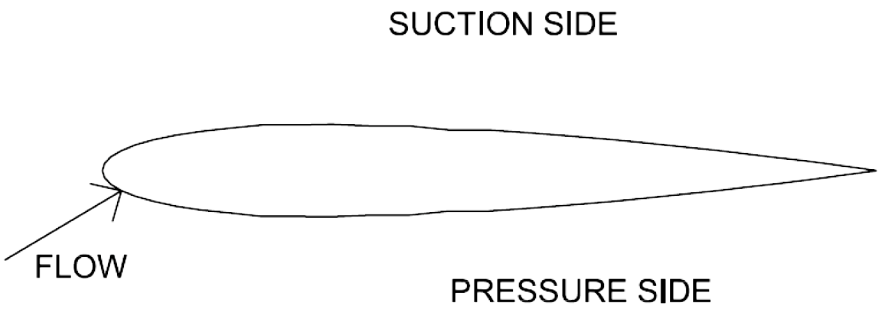

Figure 2.2 Concept picture of the pressure and suction side on a wing section

There has been conducted much research on the sectional shapes of wings and there are recommendations which sections to use in different circumstances. The NACA-series are especially well known and their advantages and disadvantages are well documented. The NACA-series were developed for aircraft wings by the National Advisory Committee for Aeronautics [5].

2.1.2 Bulb

A bulb is attached to the fin keel if the keel itself does not have enough weight to give sufficient stability to the boat. A fin keel is the most typical keel type, since the keel looks like an airplane wing. The first keel in Figure 1.1 is a fin keel. The bulb will lower the vertical centre of gravity of a keel and thereby increase the stability. A bulb will in most cases have a negative effect on the hydrodynamic performance of the keel but the loss in hydrodynamic performance is compensated with the increase

in stability. There are many rules and theories (Larsson & Eliasson [3]) for yacht keels but most of the rules are for fin keels or for long keels. Rules and theories on the effect of the bulb has on the efficiency of a keel are rare.

The frictional resistance is naturally increased if a bulb is mounted on a keel, due to the increased wetted surface. Another effect that bulb with a round sectional shape has is that it moves the trailing vortex further up and this will decrease the effective aspect ratio (Larsson & Eliasson [3]).

2.2 Computational hydrodynamics

In this section the governing equations used in computational hydrodynamics and more specifically in this thesis will be briefly explained. Further the turbulence models, boundary conditions, the overlapping grid concept and the discretization method will be explained. In the end of the section, theory of the verification and validation methods that have been used are described.

2.2.1 Governing equations

One of the governing equations used is the continuity equation, which explains the conservation of mass. If the fluid is incompressible, which means that the density ρ is constant, the continuity equation can be written in accordance with reference [7]:

$$\nabla \bullet \mathbf{v} = 0, \tag{2.11}$$

where **v** is the flow velocity, in Cartesian coordinates the equation would be:

$$\frac{\partial u}{\partial x} + \frac{\partial v}{\partial y} + \frac{\partial w}{\partial z} = 0, \tag{2.12}$$

where u, v and w are the velocity components in x-, y- and z-direction. The motions of the fluid are explained with the Navier-Stokes equations, which illustrate the flow fields when solved. The interested reader is directed to reference [7] or [8] for the full derivation of the equations. Navier-Stokes equations in Cartesian coordinates, which can be found in most fluid dynamics literature, i.e. Matusiak [7], can for the different directions be written:

$$\frac{\partial u}{\partial t} + u\frac{\partial u}{\partial x} + v\frac{\partial u}{\partial y} + w\frac{\partial u}{\partial z} = -\frac{1}{\rho}\frac{\partial p}{\partial x} + \nu\left(\frac{\partial^2 u}{\partial x^2} + \frac{\partial^2 u}{\partial y^2} + \frac{\partial^2 u}{\partial z^2}\right) + \frac{1}{\rho}F_x \tag{2.13}$$

$$\frac{\partial v}{\partial t} + u\frac{\partial v}{\partial x} + v\frac{\partial v}{\partial y} + w\frac{\partial v}{\partial z} = -\frac{1}{\rho}\frac{\partial p}{\partial y} + \nu\left(\frac{\partial^2 v}{\partial x^2} + \frac{\partial^2 v}{\partial y^2} + \frac{\partial^2 v}{\partial z^2}\right) + \frac{1}{\rho}F_y \tag{2.14}$$

$$\frac{\partial w}{\partial t} + u\frac{\partial w}{\partial x} + v\frac{\partial w}{\partial y} + w\frac{\partial w}{\partial z} = -\frac{1}{\rho}\frac{\partial p}{\partial z} + \nu\left(\frac{\partial^2 w}{\partial x^2} + \frac{\partial^2 w}{\partial y^2} + \frac{\partial^2 w}{\partial z^2}\right) + \frac{1}{\rho}F_z \tag{2.15}$$

where the left-hand side is the so-called total acceleration in the given direction and the right-hand side is the pressure force, viscous force and the body force. All forces are per unit mass. The body forces are the external forces acting on the fluid. The pressure force is the first term on the right-hand side, where p denotes the pressure. The second term is the viscous force, where ν denotes the kinematic viscosity. The viscous force is due to the viscous stresses acting on the fluid elements [7].

To solve the Navier-Stokes equations numerically would require tremendous amounts of computational time, and although the results would be very accurate it is not in reality feasible to use so much computational time. Hence some methods have been developed in order to lower the computational time. The Reynolds Average Navier-Stokes Equations (RANS) is one method for lowering the computational effort. The method is still very accurate and it can solve complex flow problems [8].

The RANS equations are time-averaged Navier-Stokes equations and the instantaneous values for the velocity u_i, pressure p and stress tensor σ_{ij} all consist of one fluctuating component and one average component. Thus the velocities would be denoted:

$$u_i = \bar{u}_i + u_i' \tag{2.16}$$

where $\bar{u}_i$ is the average velocity components in x-, y- or z-direction and u_i' is the fluctuating component. The pressure and the stress sensor can be denoted respectively. The final form of the RANS equations can be seen in equation (2.17), (2.18) and (2.19) (Matusiak [7]). The complete derivation of the equation can be found in reference [7] and [8].

$$\rho\left(\frac{\partial u}{\partial t} + u\frac{\partial u}{\partial x} + v\frac{\partial u}{\partial y} + w\frac{\partial u}{\partial z}\right) = -\frac{\partial p}{\partial x} + \mu\left(\frac{\partial^2 u}{\partial x^2} + \frac{\partial^2 u}{\partial y^2} + \frac{\partial^2 u}{\partial z^2}\right) - \rho\left(\frac{\partial \overline{u'^2}}{\partial x} + \frac{\partial \overline{v'u'}}{\partial y} + \frac{\partial \overline{w'u'}}{\partial z}\right) + F_x \tag{2.17}$$

$$\rho\left(\frac{\partial v}{\partial t} + u\frac{\partial v}{\partial x} + v\frac{\partial v}{\partial y} + w\frac{\partial v}{\partial z}\right) = -\frac{\partial p}{\partial y} + \mu\left(\frac{\partial^2 v}{\partial x^2} + \frac{\partial^2 v}{\partial y^2} + \frac{\partial^2 v}{\partial z^2}\right) - \rho\left(\frac{\partial \overline{u'v'}}{\partial x} + \frac{\partial \overline{v'^2}}{\partial y} + \frac{\partial \overline{w'v'}}{\partial z}\right) + F_y \tag{2.18}$$

$$\rho\left(\frac{\partial w}{\partial t} + u\frac{\partial w}{\partial x} + v\frac{\partial w}{\partial y} + w\frac{\partial w}{\partial z}\right) = -\frac{\partial p}{\partial z} + \mu\left(\frac{\partial^2 w}{\partial x^2} + \frac{\partial^2 w}{\partial y^2} + \frac{\partial^2 w}{\partial z^2}\right) - \rho\left(\frac{\partial \overline{u'w'}}{\partial x} + \frac{\partial \overline{v'w'}}{\partial y} + \frac{\partial \overline{w'^2}}{\partial z}\right) + F_z \tag{2.19}$$

where the third term on the right-hand side of the equations is the turbulence contribution to the mean flow and μ is the dynamic viscosity.

$$\mu = \nu\rho \tag{2.20}$$

The so-called Reynolds stress tensor R_{ij} (2.21), which is included in the third term on the right-hand side, is unknown and it must be modelled [7].

$$R_{ij} = -\begin{vmatrix} \rho\overline{u'^2} & \rho\overline{v'u'} & \rho\overline{w'u'} \\ \rho\overline{u'v'} & \rho\overline{v'^2} & \rho\overline{w'v'} \\ \rho\overline{u'w'} & \rho\overline{v'w'} & \rho\overline{w'^2} \end{vmatrix} = -\rho\overline{u_i'v_j'} \tag{2.21}$$

The Reynolds stress tensor is symmetric, thus $\rho\overline{u'v'} = \rho\overline{v'u'}$, $\rho\overline{u'w'} = \rho\overline{w'u'}$ and $\rho\overline{v'w'} = \rho\overline{w'v'}$. Hence there are 6 unknowns but still only four equations (3 Navier-Stokes equations and the continuity equation), which mean that the unknowns cannot be solved; this is known as the closure problem [9]. In order to be able to solve the equations turbulence models are introduced.

2.2.2 Turbulence models

Many turbulence models have been introduced and all of them are using empirical constants. The different models have different advantages and disadvantages for different flow problems.
The turbulence models can be grouped in to five classes [8]:

1. Zero-equation models
2. One-equation models
3. Two-equation models
4. Algebraic stress model (ASM)
5. Reynolds stress model (RSM)

In this thesis the Explicit Algebraic Stress Model (EASM) has been used, hence it is the only turbulence model that will be explained.

The EASM is developed from the Boussinesq assumption but non-linear terms are added. The Boussinesq assumption assumes that the Reynolds stress tensor is dependent to the rate of strain tensor S_{ij} in similar fashion as the viscous stresses (2.22), but instead of using the molecular viscosity μ the turbulent viscosity μ_t is used.

$$\sigma_{ij} = \mu S_{ij} \tag{2.22}$$

The turbulent viscosity is not constant over the flow field as the molecular viscosity; it will vary depending on the flow and the location according to Larsson & Raven [8].

According to the continuity equation (2.12) the rate of strain tensor would be 0 for S_{ii}, this would give a zero value for the Reynolds stress tensor R_{ii} as well. However if equation (2.21) and (2.23) are combined equation (2.24) can be derived.

$$k = \frac{\overline{u_1' u_1'}}{2} \tag{2.23}$$

$$R_{ii} = -2\rho k \tag{2.24}$$

where k is the turbulent kinematic energy. From the equations above the final Boussinesq assumption is derived (equation (2.25)) where δ_{ij} is the Kronecker delta and it is 1 if i=j and 0 if i≠j which is presented by Larsson & Raven in reference [8].

$$R_{ij} = \mu_t S_{ij} - \frac{2}{3}\rho k \delta_{ij} \tag{2.25}$$

The linear Boussinesq assumption often fails to compute complex three-dimensional flows; therefore the EASM has been developed [10]. In the EASM the Reynolds stress tensor is extended with non-linear terms and it is calculated with equation (2.26) presented in XCHAP's Theoretical Manual [9].

$$\begin{aligned} R_{ij} = {} & -\frac{2}{3}\rho k \delta_{ij} + \mu_t \left(S_{ij} + a_2 a_4 \left(S_{ik} W_{kj} - W_{ik} S_{kj} \right) \right) - \\ & a_3 a_4 \left(S_{ik} S_{kj} - \frac{1}{3} S_{mn} S_{mn} \delta_{ij} \right) \end{aligned} \tag{2.26}$$

where

$$a_1 = \frac{1}{2}\left(\frac{4}{3} - C_2\right) \tag{2.27}$$

$$a_2 = \frac{1}{2}(2 - C_4) \tag{2.28}$$

$$a_3 = \frac{1}{2}(2 - C_3) \tag{2.29}$$

$$a_4 = \frac{\tau}{\gamma_1 - 2\gamma_0(\alpha_1/\tau)\eta^2\tau^2} \tag{2.30}$$

$$\gamma_0 = \frac{C_1^1}{2} \tag{2.31}$$

$$\gamma_1 = \frac{C_1^0}{2} + \frac{C_{\epsilon 2} - C_{\epsilon 1}}{C_{\epsilon 2} - 1} \tag{2.32}$$

$$\tau = \frac{1}{\omega} \tag{2.33}$$

$$\eta^2 = S_{ij}S_{ij} \tag{2.34}$$

$$R^2 = \frac{W_{ij}W_{ij}}{\eta^2} \tag{2.35}$$

$$\mu_t = \nu_t \rho = \max\left(-k\alpha_1, \frac{0.0005k}{\beta^* \omega}\right) \tag{2.36}$$

The specific rate of dissipation of turbulent energy is denoted ω and β^* is a modelling constant. The rotation rate W_{ij} is obtained with equation (2.37), where U_i and U_j are the instantaneous velocity components.

$$W_{ij} = \frac{1}{2}\left(\frac{\partial U_i}{\partial x_j} - \frac{\partial U_j}{\partial x_i}\right) \tag{2.37}$$

α_1 in equation (2.30) and (2.36) can be solved from equation (2.38) and the correct α_1 is the solution with the lowest real part.

$$\left(\frac{\alpha_1}{\tau}\right)^3 - \frac{\gamma_1}{\eta^2\tau^2\gamma_0}\left(\frac{\alpha_1}{\tau}\right)^2 + \frac{\gamma^2 - 2\eta^2\tau^2\gamma_0 a_1 - \frac{2}{3}\eta^2\tau^2 {a_3}^2 + 2R^2\eta^2\tau^2 {a_2}^2}{(2\eta^2\tau^2\gamma_0)^2}\left(\frac{\alpha_1}{\tau}\right) = -\frac{\gamma_1 a_1}{(2\eta^2\tau^2\gamma_0)^2} \tag{2.38}$$

$C_{\epsilon 1}$=1.44, $C_{\epsilon 2}$=1.83, C_2=0.36, C_3=1.25, C_4=0.4, $C_1{}^0$=3.4 and $C_1{}^1$=1.8 are all also modelling coefficients [9].

2.2.3 Boundary conditions

The continuity equation and the Navier-Stokes equations are not enough to solve a flow field; boundary conditions have to be introduced in order to give boundary values for the equations. The boundary conditions can be grouped into three groups the solid boundary, the free surface and infinity as presented in reference [7]. Furthermore there will be boundary condition for the computational domain used in the calculations. These boundary conditions are modifications of the mathematical boundary conditions named above.

The solid boundary conditions are the boundary conditions for the areas where the fluid meets solid surface. The surfaces could for instance be a hull or the seabed. The first condition is the no-leak condition, which states that there cannot be any flow through a solid surface. Therefore, the velocity's normal component to the surface must be zero [7].

$$\mathbf{v}_n = 0 \tag{2.39}$$

The velocities at the hull surface must be 0 if the coordinate system is moving along with the hull. Thus the tangential velocity at the surface is zero.

$$\mathbf{v}_t = 0 \tag{2.40}$$

For surfaces that are not moving along with the surface the boundary condition can be replaced with

$$u = \mathbf{V}, v = w = 0 \tag{2.41}$$

where $\mathbf{V}$ is the ship velocity.

The free surface boundary conditions are the boundary conditions for surface between two liquids, in most cases the water surface between air and water. It is usually assumed that there is a known atmospheric pressure in the air p_a. The Reynolds stress and the surface tension are assumed to be zero. In reality they are very small and therefore they are neglected. Hence the atmospheric pressure is the stress and therefore the first free surface boundary condition, which is also known as the dynamic boundary condition, can be written [7]:

$$p = p_a \tag{2.42}$$

The second free surface boundary condition is known as the kinematic boundary condition and it states that a particle on the free surface has the same velocity in the normal direction as the free surface.

$$v_{particle} = v_n \tag{2.43}$$

Where v_n is the normal component of the free surface velocity and it is the only non-zero component because there is no shear stress at the surface. The waves that a ship or a boat generates are stationary if the coordinate system moves along with the vessel and in that case the free surface velocity is zero [7].

$$v_{particle} = v_n = 0 \tag{2.44}$$

The boundary conditions at infinity are used in order to have a place where the flow is completely undisturbed. In reality the place is of course not at infinity but a distance sufficiently far enough so that the flow is undisturbed and the following conditions are fulfilled:

$$u = \mathbf{U} \tag{2.45}$$
$$v = w = 0 \tag{2.46}$$
$$p = p_\infty \tag{2.47}$$

where $\mathbf{U}$ is the free stream velocity and p_∞ is the undisturbed pressure [8].

As mentioned above some of the boundary conditions have to be modified for computations because the computational domain might not be the same as reality. The computational boundaries may vary for different cases and they can be chosen arbitrary.

2.2.4 Overlapping grids

In order to solve numerically the RANS equations with a turbulence model and the continuity equation one or more grids are required together with a discretization scheme (see section 2.2.5). The grids can be structured or unstructured and they must cover the whole computational domain.

The structured grid is built up of cells in axial i, radial j and circumferential k direction. In a structured grid a mapping function can be used in order to transform the physical domain, which might be curve-linear, into the computational domain with Cartesian coordinates. In three-dimensional cases complete planes must be added when the cell number is increased, similarly complete lines must be added in two-dimensional cases. The cells in a three-dimensional structured grid are hexahedral.

Structured grids are normally of H-, O- or C-type. An H-type grid is a grid where all the gridlines go from one edge to the opposite edge and an O-type grid is circular, see Figure 2.3. The O-grid can be a full circle or a half circle.

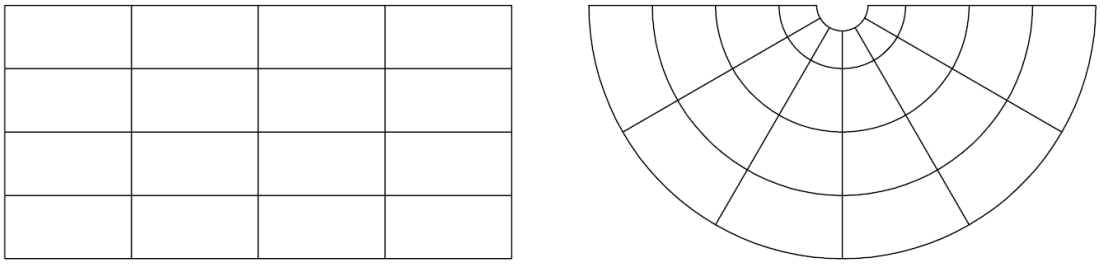

Figure 2.3 H-grid (left) and O-grid (right).

The topography is normally combined of two grid types and H-O-topography is especially common in hydrodynamics. The grid can be divided into several blocks or it can be a single block.

The advantage of the structured grids is the faster computational time compared to the unstructured grid due to the regularity of the grid.

The unstructured grid's advantage is the flexibility; a single point can be added without having to create a complete plane. This will avoid areas with unnecessary cells, which often occur in structured grids due to the complete plane (or line) insert. This will however increase the computational effort [8].

Another method of increasing the flexibility is to use overlapping grids with two or more structured grids. By doing this the flexibility of the unstructured grid is almost obtained while keeping the most of the regularity and low computational effort of the structured grid. Overlapping grids are good in shape optimisation and for meshing difficult geometries. An example of an overlapping grid can be seen in Figure 2.4.

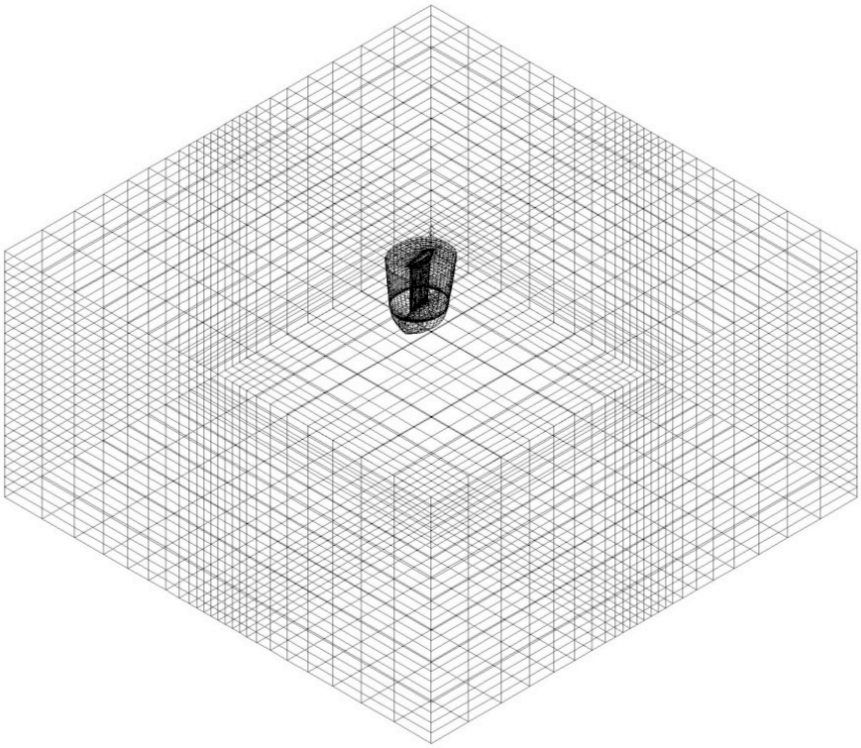

Figure 2.4 Overlapping grids

Overlapping grid components can be both boundary fitted and non-boundary fitted. The non-boundary fitted components penetrate the boundaries and therefore special techniques are required to only use the boundary fitted grids close to a boundary. This calls for a robust prioritization of the grids. The boundary fitted grids are built up around the objects and this makes the discretization easier.

Since overlapping grids are overlapping each other cells will also be overlapping each other. The cells that are from a grid with higher priority are normally prioritised, but this may cause problem at certain areas. The problem areas are the areas where a non-boundary fitted grid with higher priority is too close to a boundary of a boundary fitted grid with lower priority. Those areas are better represented by the grid that is fitted to the boundary, so therefore the priority rule cannot be used in those areas. In XCHAP this is solved with a distance function ϕ_B. This function calculates the shortest distance for a cell to the nearest boundary, thus at the physical boundaries the functions value is zero. If two cells overlap each other the cell with the lowest ϕ_B is chosen [11].

The grid close to the wall has to be very fine in order to resolve the boundary layer. In equation (2.48) y^+ should not be larger than 1. y is the distance from the wall to the first discretization point and y^+ is the nondimensional distance. Thus, the discretization point must be well inside the viscous sublayer, which is the inner layer of the turbulent boundary layer [8].

$$y^+ = \frac{yu_\tau}{\nu} \tag{2.48}$$

u_τ is the friction velocity and is derived from equation (2.49).

$$u_\tau = \sqrt{\frac{\tau_w}{\rho}} \tag{2.49}$$

The wall shear stress τ_w can be expressed with:

$$\tau_w = C_f \frac{1}{2} \rho U^2 \tag{2.50}$$

where C_f is the local skin friction coefficient [8]. The skin friction coefficient is dependent on the Reynolds number R_n, equation (2.51), where L is the characteristic length of the analysed object.

$$R_n = \frac{UL}{\nu} \tag{2.51}$$

$$C_f = \frac{0.0576}{\sqrt[5]{R_n}} \tag{2.52}$$

Equations (2.48)- (2.52) are all presented in reference [8].

2.2.5 Discretization

There are three common discretization methods in numerical calculation methods, Finite Volume Method (FVM), Finite Difference Method (FDM) and Finite Element Method (FEM). FEM has hardly been used in computational hydrodynamics while the other two are more common. FVM is the most used within computational hydrodynamics and also the discretization method used in XCHAP and therefore it is the only method that will be explained in this thesis, it will be explained in accordance with reference [8].

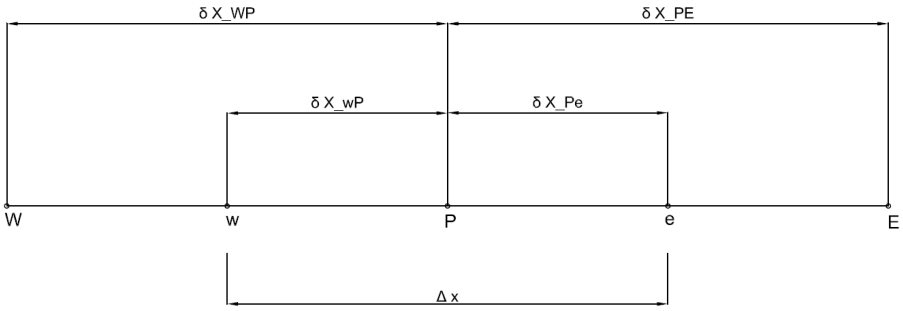

Figure 2.5 Finite Volume Method 1D [8]

In Figure 2.5 a conceptual picture of the FVM in one-dimension can be seen. The discretization is applied on node P and the capital letters W (west) and E (east) are the notations for the surrounding nodes in the control volume. The faces on each side of the node P are denoted with the small letters w (west) and e (east). The distances between the different nodes are also shown in the figure. The distance between W and P, δX_{WP} and the distance between P and E, δX_{PE} do not have to be equal.

The objective is to link the dependent variable ϕ (i.e. u_i, k, p, ω) at P to the dependent variable ϕ at W and E and this is done by using Gauss Theorem. Thus the transport equation of the RANS equation, together with the turbulence models can be written in a steady state form:

$$\frac{d}{dx}(u\phi) = \frac{d}{dx}(\Gamma\frac{d\phi}{dx}) \tag{2.53}$$

The diffusion coefficient Γ is dependent on the dependent variable. Equation (2.53) applied on the one-dimensional case in Figure 2.5 with a cross-sectional area A of the control volume can be written:

$$(uA\phi)_e - (uA\phi)_w = (\Gamma A\frac{d\phi}{dx})_e - (\Gamma A\frac{d\phi}{dx})_w \tag{2.54}$$

The continuity equation (2.11) is also needed for the derivation, thus

$$(uA)_e - (uA)_w = 0 \tag{2.55}$$

(2.56)

In a three-dimensional case 4 more nodes of the discretization point P have to be introduced n (north), s (south), t (top) and b (bottom) [8].

2.2.6 Verification and Validation

Since the numerical results from CFD calculations are just models which resemble real flow problems, the order of accuracy of the results is an important concern in order to know how close to the real solutions the model solutions are. In order to estimate the error a verification and validation method is used. P.J. Roache stated that verification is a process of "solving the equation right" while validation is a process of "solving the right equation" [12]. Thus verification is a method to estimate the numerical error and validation is a method of showing the model error. The validation is usually done through experimental testing such as wind tunnel tests and towing tank tests [13]. In this thesis two verification methods have been used and the reason for this is that they may lead to different results and the used method will be based on the outcome of the results. The two used methods are the Factor of Safety (FS) method and the Least Square Root (LSR) method. An assumption is made that the iterative uncertainty U_I and grid discretization uncertainty U_G are the only contributors to the numerical uncertainty U_ϕ. The iterative error is dependent on the convergence of the calculated solution, thus even though the convergence criterion is met there is still a small error due to the lack of complete convergence. The discretization error is caused by the discretization of the equations used [8]. The round-off error is the last contributor to the numerical uncertainty but it is usually neglected in practical CFD problems [13]. Therefore the numerical uncertainty can be approximated with equation (2.57) as presented in reference [14].

$$U_\phi = \sqrt{U_I^2 + U_G^2} \tag{2.57}$$

Both methods are based on grid convergence studies and compare all other grids to the finest grid.

The purpose of the verification is to find a confidence interval where the exact solution lies within with a 95% probability, equation (2.58).

$$\phi - U_\phi \leq \phi_{exact} \leq \phi + U_\phi \tag{2.58}$$

Where ϕ_{exact} is the exact solution and ϕ is the numerical solution of the finest grid. The exact solution is the imagined solution for a grid with zero step size. [15].

Factor of Safety method

The FS method is a method developed by Xing & Stern [15] where the uncertainty and error are estimated with a correction factor. This is similar to the method that the ITTC (International Towing Tank Conference) recommends. The method will be explained in accordance with reference [15]. The method requires the iterative uncertainty to be at least one order of magnitude smaller than the grid discretization error.

Three grids (triplets), which have been systematically changed, are analysed in this method. The grids used are refined with a refinement ratio r,

$$r = \frac{\Delta_{x_2}}{\Delta_{x_1}} = \frac{\Delta_{x_3}}{\Delta_{x_2}}, \tag{2.59}$$

where Δ_x are the grid spacing for the three grids. Grid number 1 is the fine grid, grid number 2 is the medium grid and grid number 3 is the coarse grid.
In order to decide the type of convergence a convergence ratio R is introduced. R is the ratio between the solution differences according to equation (2.60).

$$R = \frac{\phi_2 - \phi_1}{\phi_3 - \phi_2} \tag{2.60}$$

The convergence is monotonic if $0<R<1$, oscillatory convergent if $-1<R<0$, monotonic divergent if $R>0$ and oscillatory divergent if $R<-1$.

The discretization error δ_{RE}, is calculated with Richardson Extrapolation equation (2.61), where ϕ_i is the local quantity, ϕ_o the estimated exact solution, α is a constant, h_i the typical cell size and p is the order of accuracy.

$$\epsilon \cong \delta_{RE} = \phi_i - \phi_o = \alpha h_i^p \tag{2.61}$$

Once the type of convergence has been determined the order of accuracy can be calculated. The theoretical order of accuracy p_{th} =2 while the determined order of accuracy p_{RE} is calculated with equation (2.62) followed by the error estimate equation (2.63).

$$p_{RE} = \frac{\ln\left(\frac{\phi_3 - \phi_2}{\phi_2 - \phi_1}\right)}{\ln(r)} \tag{2.62}$$

$$\delta_{RE} = \frac{\phi_2 - \phi_1}{r^{p_{th}} - 1} \tag{2.63}$$

The calculated order of accuracy should theoretically be the same as the theoretical order of accuracy $p_{RE}=p_{th}$. This means that the solution is within the asymptotic range. However this is rarely the case in reality, because p_{RE} differs consistently in real cases from p_{th} [15], and the ratio (distance metric) is denoted:

$$P = \frac{p_{RE}}{P_{th}} \tag{2.64}$$

The numerical uncertainty can generally be expressed as a factor of safety multiplied by the error, equation (2.65).

$$U_G = F_s \, |\delta_{RE}| \tag{2.65}$$

Xing et al. [15] introduces a factor of safety dependent on the distance metric and the final uncertainty is calculated according to equation (2.66). The safety factors are based on statistical analysis.

$$U_{FS} = F_s \, (P)|\delta_{RE}| = \begin{cases} (2.45 - 0.85P)|\delta_{RE}|, 0 < P \leq 1 \\ (16.4P - 14.8)|\delta_{RE}|, P > 1 \end{cases} \tag{2.66}$$

Least Square Root method

The LSR method presented below is developed by Eça et al. and described in reference [13] and [14]. The LSR method discards the iterative error and the condition for using the method is that the iterative error must be two orders of magnitude smaller than the discretization error. Thus if the iterative error is 100 times smaller than the discretization error the iterative error can be neglected.

The LSR is also using Richardson Extrapolation equation (2.61). There are three unknowns ϕ_o, α and p in the equation, hence three grids are needed in order to solve the equations, but the method itself requires at least 4 grids [14] this will make the solution more certain. Thus one equation of form (2.61) is set up for every grid and the unknown's ϕ_o, α and p are solved with a Least Square fit. By doing this a curve is fitted to the obtained results. The result is plotted against h_i/h_1, which can be calculated with equation (2.67).

$$\frac{h_i}{h_1} = \sqrt[3]{\frac{(N_{cells})_1}{(N_{cells})_i}} \tag{2.67}$$

The convergence of the grid discretization is monotonic if p>0, oscillatory if $n_{ch} \geq INT(n_g/3)$ where n_{ch} is the number of triplets with $(\phi_{i+1} - \phi_i)(\phi_i - \phi_{i-1})<0$ and the grid discretization is not behaving regularly in other cases.

However equation (2.61) is only valid when the convergence is monotonic. Therefore the additional equations below are implemented, solved and curve fitted when the convergence criteria are not met.

$$\delta_{RE}{}^{02} = \phi_i - \phi_o = \alpha_{01} h^2 \tag{2.68}$$

$$\delta_{RE}{}^{12} = \phi_i - \phi_o = \alpha_{11} \, h + \alpha_{12} h^2 \tag{2.69}$$

$$\delta_{\Delta_M} = \frac{\Delta_M}{\left(\frac{h_{n_g}}{h_1}\right)-1} \tag{2.70}$$

Where $\Delta_M=\max(|\phi_i- \phi_j|)$, $1\geq i, j\geq n_g$
The discretization error δ_{RE} must be converted into a numerical uncertainty and this is done using the following formulas:

$$0.95 \leq p \leq 2.05:\ U_\phi = 1.25\delta_{RE} + U_S \tag{2.71}$$

$$0 < p \leq 0.95:\ U_\phi = \min\left(1.25\delta_{RE} + U_S, 3{\delta_{RE}}^{12} + {U_S}^{12}\right) \tag{2.72}$$

$$p \geq 2.05:\ U_\phi = \max\left(1.25\delta_{RE} + U_S, 3{\delta_{RE}}^{02} + {U_S}^{02}\right) \tag{2.73}$$

The numerical uncertainty is obtained from equation (2.74) if the convergence is oscillatory.

$$U_\phi = 3\delta_{\Delta_M} \tag{2.74}$$

If the convergence is behaving randomly the numerical uncertainty is obtained with equation (2.75).

$$U_\phi = \min\left(3\delta_{\Delta_M}, 3{\delta_{RE}}^{12} + {U_S}^{12}\right) \tag{2.75}$$

The least squares fits standard deviations are denoted U_S, ${U_S}^{02}$, and ${U_S}^{12}$ [14] and they are calculated with equation (2.76).

$$U_S = \sqrt{\frac{\sum_{i=1}^{n_g}(\phi i-(\delta_{RE}))^2}{n_g-3}} \tag{2.76}$$

Where δ_{RE} is replaced with equation (2.61) for U_S, with equation (2.68) for ${U_S}^{02}$ and with equation (2.69) for ${U_S}^{12}$ as presented by Eça et al. [16].

Validation

The validation uncertainty is calculated, according to reference [14], with equation (2.77). U_Φ is the numerical uncertainty and U_D is the uncertainty obtained in experimental tests. U_{input} is the uncertainty for the fluid properties and geometry and it is called the parameter uncertainty.

$$U_{val} = \sqrt{U_\phi^2 + U_{input}^2 + U_D^2} \tag{2.77}$$

The validation uncertainty is compared to the comparison error E, which is taken as the numerical solution S subtracted by the experimental solution D.

$$E = S - D \tag{2.78}$$

Eça et al. state [14] that the solution is validated if $|E|<U_{val}$ and that the modelling error is too large if $|E|>>U_{val}$. However, if $|E|<U_{val}$ can also mean that the quality of both the numerical and exeprimental solution is poor.

2.3 Optimisation

Optimisation in engineering is a method of finding one or many optima from a population of designs, the population can be given or arbitrary generated.

An optimisation consists of an objective function, design variables and constraints. The objective function **F(X)** is the function that is optimised in the process and it is dependent on the design variable vector **X**. The vector consist of values X_n and all values can either have set limitations or have unlimited freedom. These limitations are also known as side constraints.

$$X_n^1 \leq X_n \leq X_n^2 \tag{2.79}$$

Where X_n^1 and X_n^2 are the side constraints and they can either be values or infinite. The whole function can also be constrained with either equality constraints or inequality constraints. An equality constraint constrains a value to be equal to a certain value/parameter or relative to a certain value/parameter. An inequality constraint constrains a value to be smaller or great than a certain value/parameter [17].

2.3.1 Genetic algorithm

A Genetic Algorithm (GA) is an algorithm that uses evolution from biology as a model. The basic concept of the algorithm is that it checks the fitness of a variant (parent variant) and reproduces a new variant (offspring) from it if the variant is fit enough. The fitness is evaluation is based on the object function. A concept picture of a genetic algorithm can be seen in Figure 2.6 as described by Abraham et al. [18]. The reproduction can either go through mutation or crossover. Mutation uses a fit variant and makes small changes to it and hopefully improves the design. The crossover reproduction takes two fit parent variants and combines them into a new offspring.

In the beginning of an optimisation process a genetic algorithm creates an initial population, which can be created randomly or based on an initial design. The algorithm parallel computes all variants in a population and when it is finished the next iteration round is calculated. An iteration in a genetic algorithm is often referred as a generation [18].

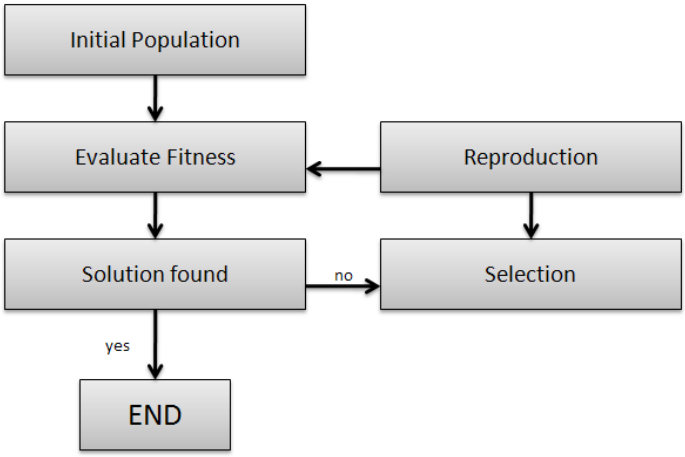

Figure 2.6 Genetic Algorithm flow chart [18]

Cirello & Manucuso state in reference [19] that the advantage of a genetic algorithm compared to a conventional algorithm is that it can run many parallel calculations at the same time. This will reduce the risk for the algorithm to converge to a local optimum, because it will have better possibilities to cover the whole design space.

2.3.2 Non-dominated Sorting Genetic Algorithm, NSGA-II

The Non-dominated Sorting Genetic Algorithm (NSGA) is a genetic algorithm but the fitness evaluation of the variants differs from the other genetic algorithms. The variants are divided into non-dominated fronts depending on their non-domination. A solution is non-dominated with respect to another solution if it partially smaller than the other solution [20].

The concept of the NSGA is shown in Figure 2.7, where it can be seen that in the beginning of the algorithm the first generation is created followed by the creation of the Front1. After the algorithm has seen that the whole population is not classified (assigned dummy fitness) it checks the whole population and selects the fittest variants and gives them a dummy fitness and they are all part of the first front. Once the dummy fitness has been assigned the variant is shared with the dummy fitness. Sharing is a method of not letting the algorithm get stuck in one region and allows many Pareto optima. The sharing function divides the dummy fitness with a factor that is proportional to the number of variants in that region [20].

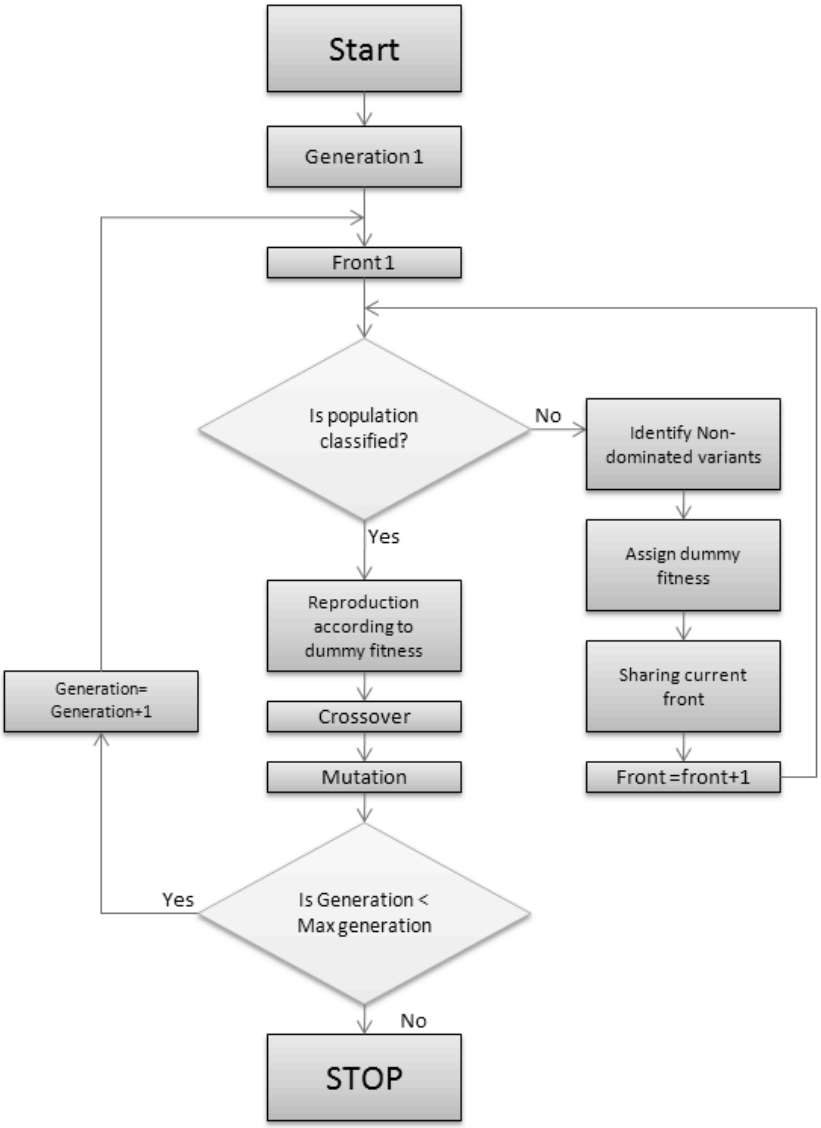

Figure 2.7 NSGA flow chart taken from reference [20]

Once the sharing has been done the next front (Front2) is created and the steps above are repeated for the remaining variants in as many loops as required before the whole population has been classified. The variants of front number n are always non-dominated to the variants in front number n+1. After the whole population has been classified the variants are reproduced according to their dummy fitness, the variants in the Front1 has the highest probability to reproduce. The same reproduction with crossover and mutation is used in an NSGA as in other GA:s. Once the crossover has taken place the next generation is created, the whole loop is done until the set maximum generations are achieved.

The NSGA-II is an improved version of the first NSGA. The algorithm has been made faster and the sharing function is replaced by a crowded comparison approach. The crowded comparison approach is according to reference [21] superior to the sharing function. The sharing functions disadvantages are the diversity of the solutions are depending on a chosen sharing parameter, which can be chosen very badly. Another disadvantage is that it has a high complexity. The crowded

comparison approach on the other hand is not dependent on a selected parameter. The crowded comparison approach estimates the density of other solutions around the compared solution and assigns it a crowding distance. So when the algorithm compared two variants firstly the variant, which belongs to a lower front, is preferred but if both variants are belonging to the same front the variant with the higher crowding distance is preferred. A variant with a lower crowding distance lies in a more crowded area. Thus the crowded comparison tries to increase the diversity of the population [21].

2.4 Velocity Prediction Program VPP

A velocity prediction program is a program for predicting the performance of a sailing yacht. There are both static and dynamic VPP:s on the market; the dynamic VPP will not be explained in this thesis because it has not been used. The basic concept of a VPP is that it solves equilibrium equation of the yacht. Hence, all forces and moment for the boat have to cancel each other in all 6 degrees of freedom to be in an equilibrium state. Both aerodynamic and hydrodynamic forces are taken into account and experimental data can be imported into most VPP:s on the market. Larsson & Eliasson [3] presents the relations for the forces and moments as:

1. Along the direction of motion the driving force from the sail is equal to the total resistance.
2. At right angles to the direction of the motion in the horizontal plane the side force from the sails is equal to the side force of the underwater body.
3. Vertically, the buoyancy force is equal to the gravity force and the vertical components of the keel and sail forces are assumed to cancel each other.
4. The heeling moment from the sails is equal to the transverse righting moment from the hull.
5. The pitching moment from the sails is equal to the longitudinal righting moment from the hull.
6. The total yawing moment is zero, since the hydro and aerodynamic forces act along the same line in the horizontal plane.

A VPP is using an iterative method to obtain the results, the initial boat speed and heel angle is guessed. Once the results have converged for the desired wind speeds the result can be presented, which often is presented in a polar plot. A polar plot is a diagram where the velocity of the boat can be obtained for different true wind speeds and true wind directions. The velocity made good (abbreviation VMG), which is one of the most important outputs of the VPP, is normally also plotted in the polar plot. When the boat is sailing upwind VMG is the velocity component opposite to the direction as the true wind velocity, see Figure 2.8 [3]. Downwind it is the component along the wind direction.

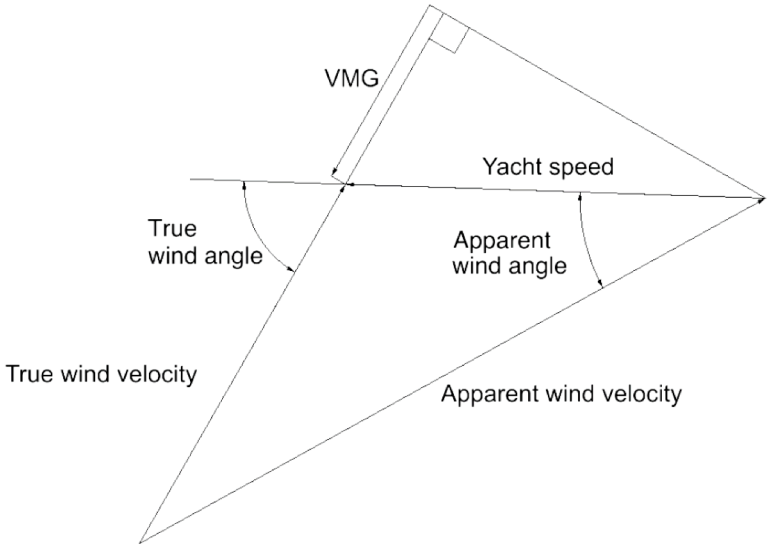

Figure 2.8 The different wind and speed components [3]

The difference between the true wind angle and the apparent wind angle is also displayed in Figure 2.8. The true wind angle is the angle from where the wind is actually coming and the apparent wind angle is the angle of the wind how it is felt in the direction of the motion. The angle difference is due to the yacht speed.

3. Investigated cases

3.1 CFD

The CFD configuration and the CAD models used in the investigated cases will be presented in this section.

3.1.1 The initial keel model

The initial keel model that was used was the keel design in reference [1] with some minor modifications. The modifications do not have a large effect on the performance of the keel. They were done in order to be able to perform the optimisation.

An integrated bulb keel has a smooth transition between the bulb and fin part of the keel. The design of the keel can be seen in Figure 3.1 and Figure 3.2.

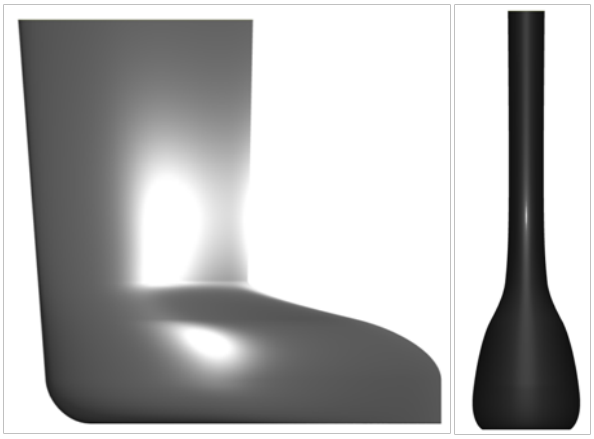

Figure 3.1 Side view and front view of the initial keel design

The particulars of the keel can be seen in Table 3.1. The keel mass is for a keel made of cast iron with a density of 7000 kg/m^3 and the centre of gravity is taken from the intersection between the leading edge and the root chord. The tip chord is taken as the length of the tip chord for a keel without a bulb. Thus the distance between the extrapolated values for the leading and trailing edge at the bottom of the keel. The bulb length is the maximum length of the bulb and the aspect ratio is the geometrical aspect ratio with a keel span mulitplied by 2 which is a normal way of presenting the aspect ratio [3].

Table 3.1 Particulars of the initial keel

Volume [m^3]	0.386	**T_K [m]**	1.86
Mass [kg]	2702.41	**Root chord [m]**	1.08
Wetted surface [m^2]	5.25	**Tip chord [m]**	0.6
Centre of gravity [m]	[0.731,0,-1.27]	**Bulb length [m]**	1.817
Planform area [m^2]	1.8414	**Fin part heigth [m]**	1.2
Sweep angle [°]	5	**Bulb part heigth [m]**	0.66
TR	0.833	**AR**	3.76

The keel is built up of some NACA-sections with surfaces swept over them. The NACA-sections are scaled with a parameter curve, which will be more explained in 3.2.3. The fin part of the keel has a NACA 63-015 section at the root chord and it is

gradually changing into a NACA 65-018 section at the intersection between the fin part and the bulb part. The bulb is built up of NACA 65-018 sections.

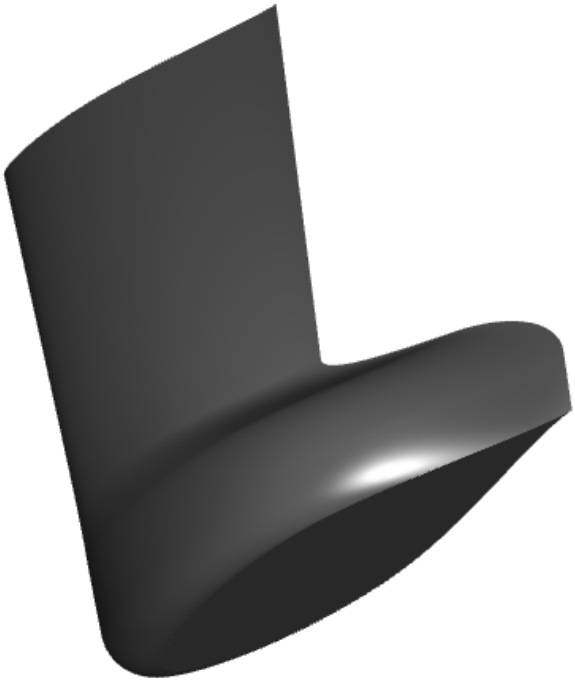

Figure 3.2 Fish eye view of the keel

3.1.2 Grid generation

Two overlapping grids were used in the CFD calculations, one box module for the surrounding grid and one rudder module for the keel. The box grid is rectangular and it is stretched in order to have denser grid in the middle where the keel is situated and coarser grid at the outer edges. This will increase the calculation accuracy around the keel where it is needed and decrease the accuracy at the outer edges in order to decrease the computational effort. The grid was stretched in x- and y-direction (see Figure 3.3) with a stretching function. In z-directions the cell sizes were uniform. The background grid domain was set to [-10, 10], [-10, 10], [-10, 0], since this will give a grid large enough for the keel that has a nondimensionalized span length of 1.86.

The stretching function used in the x- and y-direction was a middle stretching function, *stre(id="middlex",midd,s0=0.35,s1=0.65,ds0=0.4)*, where ds0=0.4 sets the cells in the middle of the domain to be 40% of the cell size of the uniform cells used with no stretching function. s0 and s1 are the boundaries for the cells with the ds0 cell size, thus the ds0 cells lays between 35% of the domain to the 65% of the domain. These setups have been configured so that the box grid and the keel grid have approximately the same cell size at the outer boundary of the keel grid.

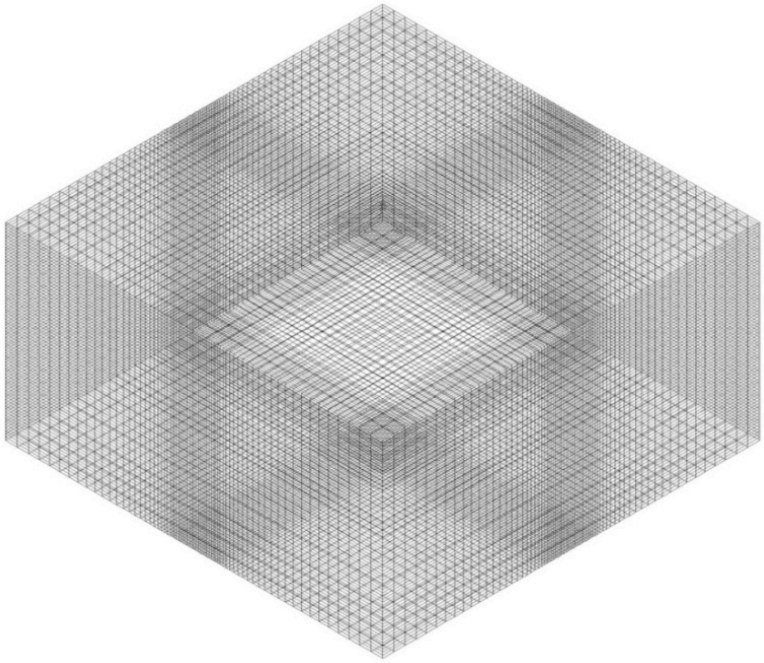

Figure 3.3 Background grid

SHIPFLOW has a module for modelling rudders but it can also be used for modelling other wings such as keels. This rudder module has been used for modelling the keel. The reason for choosing this module is that it is built up on wing section. Hence the sections are exported from a CAD model into separate files that can be read into the module. By doing this, the sections can be easily varied in the optimisation process and imported into SHIPFLOW. The grid has been stretched with a hyperbolic stretching function in all direction (see Figure 3.4), because the grid has to be dense close to the keel, in order to model the boundary layer correctly.

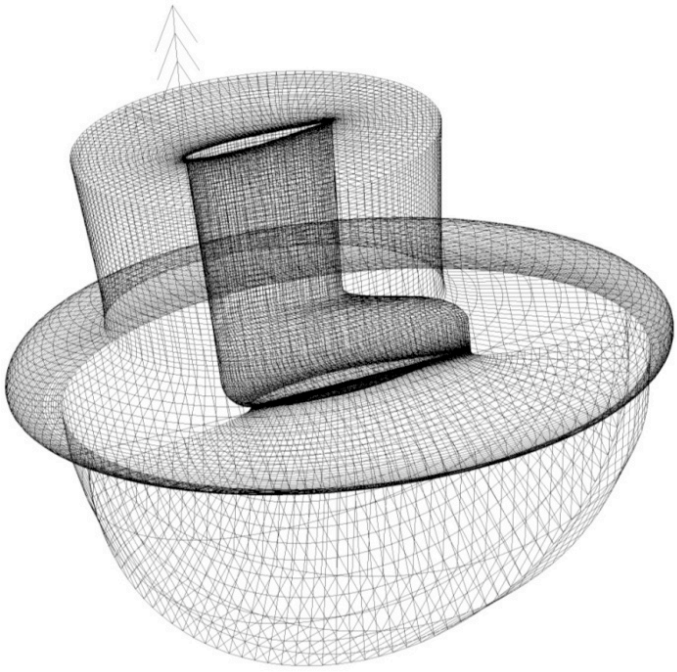

Figure 3.4 Keel grid

The finest grid used in the uncertainty analysis, used for choosing the grid size, has to be very fine as explained in section 2.2.6. A cell number of 3899468 was used in the finest grid, where the box grid had 101 grid nodes in all directions and the keel had 171 grid nodes in circumferential direction, 101 nodes in radial direction and 131 nodes in axial direction. The nondimensional distance y^+ was set to 0.6 for the finest grid in order to still have a reasonable y^+ for the coarser grids. y^+ should be smaller than one as mentioned in section 2.2.4.

A refinement ratio of $\sqrt[4]{2}$ was used for the refining of the grids. A refinement ratio of $\sqrt{2}$ was tried but it was too coarse. The number of grid nodes was divided with the refinement ratio while the nondimensional distance y^+ was multiplied with it. The number of cells and number of points can be seen in Table 3.2. In every case 8000 iterations were used.

Table 3.2 Grids used in the uncertainty analysis

	Name	Cell number	Points
1	**Grid01**	3899468	3628817
2	**Grid01_5**	2404044	2209125
3	**Grid02**	1464680	1325669
4	**Grid02_5**	919755	818550
5	**Grid03**	571157	498230

The results of the uncertainty analysis will be presented in section 4.1.

3.1.3 Boundary conditions

In the RANS solver XCHAP the boundary conditions presented in Table 3.3 are possible to include in the calculations.

Table 3.3 Boundary conditions taken from XCHAP Theoretical Manual [9]

	NO-SLIP	SLIP	INFLOW	OUTFLOW
v	**v**=0	$\frac{\partial \boldsymbol{v}}{\partial \xi_B} = 0$	**v**=constant	$\frac{\partial \boldsymbol{v}}{\partial \xi_B} = 0$
p	$\frac{\partial p}{\partial \xi_B} = 0$	$\frac{\partial p}{\partial \xi_B} = 0$	$\frac{\partial p}{\partial \xi_B} = 0$	p=0
k	k=0	$\frac{\partial k}{\partial \xi_B} = 0$	k=constant	$\frac{\partial k}{\partial \xi_B} = 0$
ω	$\omega = f(u_\tau,...)$	$\frac{\partial \omega}{\partial \xi_B} = 0$	ω =constant	$\frac{\partial \omega}{\partial \xi_B} = 0$

v is the time averaged velocity, p the pressure, k the turbulent kinetic energy and ω is specific rate of dissipation of turbulent energy. ξ_B is the parameter direction crossing the boundary, thus it is the direction normal to the boundary.

The box grid has SLIP condition on the top, the bottom and on the sides while it has INFLOW on the side facing the incoming flow and OUTFLOW on the side facing the outgoing flow. The keel grid has NOSLIP condition on the keel surfaces. On the outer surface of the keel grid an INTERIOR boundary condition was set. The INTERIOR boundary conditions interpolates the values from the neighbouring grid or grids, hence it interpolates between the cells in the box grid at the boundary for the keel grid. On the top surface of the keel grid a SLIP condition was set so that coincide with the background grid boundary condition.

3.1.4 CFD solver

The CFD solver that was used was SHIPFLOW 4.4.04 as described in section 1.3. The module XCHAP was employed as a RANS-equation solver and the Explicit Algebraic Stress Model (EASM) was used as turbulence model. XCHAP can handle overlapping grids, which is of large importance in this thesis.

The computations were carried out at full scale and the Reynolds number used in the calculations was based on the velocity from the initial VPP results and the characteristic length was taken as the length of the mean chord 0.99m. The velocity U was 6.8 knots which is equal to 3.5 m/s.

$$R_n = \frac{UL}{\nu} = \frac{3.498\frac{m}{s} * 0.99m}{10^{-6}\frac{m^2}{s}} = 3.46 * 10^6 \quad (3.1)$$

The leeway angle was also obtained from the VPP calculations and a leeway angle of 4° was obtained for 8 m/s. A kinematic viscosity of 10^{-6} m^2/s was used. The setup for the XCHAP calculations can be seen in APPENDIX 2.

3.2 Optimisation

The optimisation was set up on Chalmers University of Technology's computational cluster, which has 268 nodes that all have 2 CPU's with 8 cores each. The processors were Intel Xeon 5520 that all have at least 24 GiB memory. 4-8 nodes were used in the optimisation loop depending on the traffic at the cluster.

3.2.1 Work flow

The optimisation was set up according to the flow chart in Figure 3.5 and it was fully automated. The generic integration, the NSGA-II and Des Var are all applications integrated in the Friendship Frameworks. The optimiser creates the new variants using the NSGA-II algorithm explained in section 2.3, once variants are created the information is sent to the Des Var which makes the changes to the design variables, exports 59 Z-section files and sends the required information changes to the generic integration. The generic integration integrates the different components used in the optimisation. The generic integration makes the required changes to the command file (see APPENDIX 2) and sends the file together with the section file to the cluster, where the CFD calculations start. Once the CFD calculations are done a script (force.py) takes the average results (drag and lift forces) from the last 10% of the iterations and calculates from that the drag and lift coefficients and also the ratio C_D/C_L. C_D/C_L-is the objective function which will be minimised, hence the algorithm will try to lower the drag while improving the lift. C_D and C_L are calculated with

equation (2.6) respectively equation (2.5). The forces and C_D/C_L-ratio is written in a file (meanforce.dat) and sent back to the generic integration. The NSGA-II algorithm is taking the results into account and creates the next generation of variants, which is the start of the next loop.

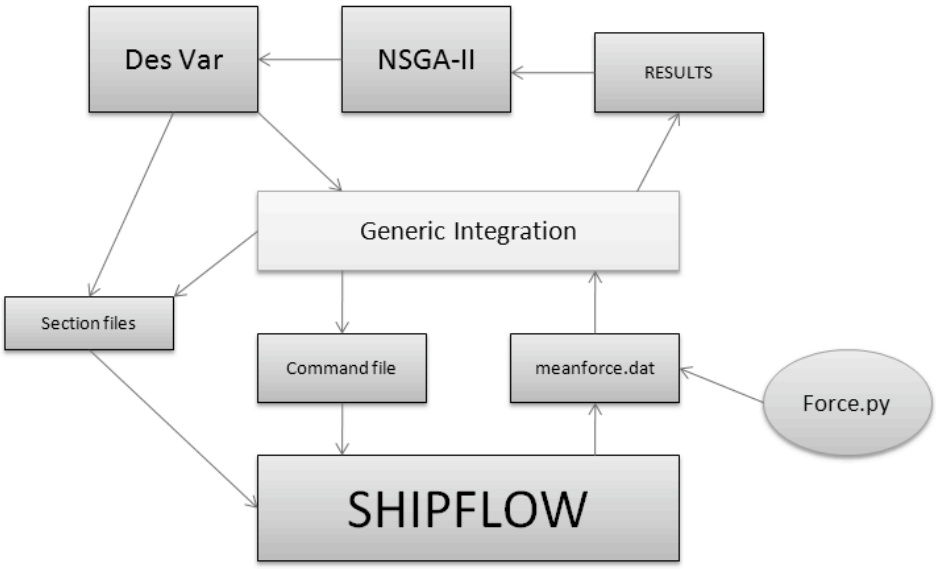

Figure 3.5 Optimisation loop

4500 iterations were done in every SHIPFLOW calculation and each calculation lasted approximately 14 hours.

3.2.2 Design variables

The design variables where chosen carefully and the number of variables was kept as low as possible and still give a reasonable freedom to the shape variation. The reason for keeping the number of design variables low is to minimize computational time and it was chosen to use 7 design variables.

The first design variable 3DPoint02_X (the point above the trailing edge of the bulb in Figure 3.6) was changing a parameter that was controlling the length of the NACA-profiles of the bulb, hence it was controlling the length of the bulb. The other design variables were all changing a parameter curve (the green curve in Figure 3.6) that was controlling the height and breadth of the NACA-profiles of the bulb. The parameter curve had more control points than that are seen in Figure 3.6 but they are not shown in the picture for convenience. The parameter curve lies in the XZ-plane, but it scales the NACA-profiles in transversal (Y) and vertical (Z) direction.

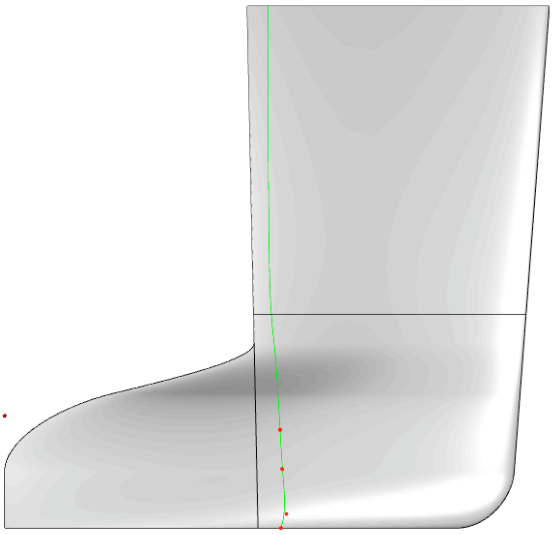

Figure 3.6 Parameter curve and control points

The lowest point on the parameter curve can only be moved in X-direction, thus the design variable TC07_X was controlling how wide the flat bottom of the bulb is. The point was set to a constant value in vertical direction because the span of the keel had to be fixed. The second lowest point on the parameter curve could be moved in two directions X and Z, therefore two design variables had two be used TC06_X and TC06_Z.

Table 3.4 Side constraints for the design variables. The units are in meters

Variable	Lower limit	Initial value	Upper limit
TC05andTC5b_X	0	0	0.07
TC05b_Z	-1.55	-1.51	-1.3
TC05_Z	-1.7	-1.65	-1.65
TC06_X	0.06	0.14	0.2
TC06_Z	-1.86	-1.81	-1.7
TC07_X	0	0.12	0.15
3DPoint02_X	-1.1	-0.8665	-0.6

The design variables TC05b_Z and TC05_Z were controlling the two higher points in vertical direction, while the TC05andTC5b_X was controlling the two points in a transversal direction simultaneously. This setup for TC05andTC5b_X was chosen in order to lower the number of design variables and speed up the optimisation.

The lower and upper side constraint for each design variable can be seen in Table 3.4 together with the initial value for each variable. The side constraints were set so the shape was kept as an L-shape and they had to be kept within reasonable limits to avoid a very large design space.

3.2.3 Constraints

The optimisation was set up with some constraints in order to still fulfil some requirements the keel had to fulfil after the optimisation. The constraints were inequality constraints but also limitations for the design variables and the span.

The span was set to a constant value because the span does not only have an influence on the hydrodynamic and stability performance the span has also a practical aspect due to shallow sailing areas. The constant span was the same as the span for the initial keel design 1.86m.

Another limitation was the global shape of the bulb keel. The shape must be kept as an L-shape, which means that no part of the bulb can be in front of the leading edge of the keel. The optimisation was limited to the bulb part, hence the fin part of the keel was not optimised as described in section 1.4. The reason was that the focus of the thesis lies on the integrated bulb.

The inequality constraints that were set were a maximum mass of the keel and a minimum moment. The maximum mass was set to 3200 kg which is higher than the initial keel mass (2702.41kg), the reason for the higher maximum weight is to give the optimisation algorithm more freedom and a higher weight will give a hydrodynamic disadvantage, hence the algorithm will probably not find the optimal design with a high weight. The minimum moment was set in order keep a sufficient stability of the yacht. The lower limit for the moment was set to 33.78kN and it was calculated with equation (3.2), where m is the mass of the keel, g the acceleration of gravity and VCG_{keel} is the distance of the centre of gravity of the keel from the root of the keel.

$$\text{Moment} = m * g * VCG_{keel} \tag{3.2}$$

The centre of gravity of the keel was free to move, but in vertical direction it was indirectly constrained by the moment constraint.

Two other inequality constraints were added after noticing that the algorithm tried unreasonable designs. These constraints will prevent the unreasonable designs and speed up the optimisation. Both of the constraints were constraining the design variables. The first one constrained design variable TC05_Z to be smaller than TC05_5_Zb and the other one constrained design variable TC07_X to be smaller or equal to TC06_X (see Figure 3.6).

A penalty value of C_D/C_L=0.1 was given to all variants that were violating the constraints, the penalty was given before the CFD calculations was done and the result was directly send to back to the NSGA-II instead of starting the CFD calculation. By doing this unnecessary CFD calculations could be avoided and the optimisation time could be shortened. By giving a high penalty value to the violated variants the algorithm will see them as weak variants and try to find variants in other areas of the design space.

3.3 Experimental validation

Wind tunnel tests were carried out for validation of the CFD results. Validation is a very important part of CFD calculations because the CFD calculations trustworthiness is very dependent on the type of flow problem. The type of calculations that has been done in this project has not been carried out often before. The experimental wind tunnel tests were therefore particularly important in this thesis.

3.3.1 Physical explanation of the wind tunnel and the keel models

The experimental tests were carried out in the wind tunnel at the Department of Applied Mechanics at Chalmers University of Technology in Gothenburg Sweden. The wind tunnel has a 2.7m long test section with a total width of 1.8m and a height of 1.25m. The wind tunnel cross section is gradually increasing downstream in order to keep a constant pressure in spite of the growing boundary layers on the walls. A picture of the keel model mounted in the wind tunnel, a picture of the keel in the wind tunnel in the wind tunnel looking from the flow direction and a side view can be seen in Figure 3.7. The keel seen in the middle picture is not the keel with the initial design. It is another keel and the picture is just a conceptual picture of the setup in the wind tunnel.

The keel model was manufactured at a scale of 1:2.5, which means that the span of it was 0.744m. It was a model of the initial design (see section 3.1.1). The keel was made out of a hard foam called NECURON® 651, which was painted and a steel rod was inserted for mounting the balance. The material properties of NECURON® 651 are displayed in Table 3.5.

Table 3.5 Material properties of NECURON® 651

Compressive strength	26 N/mm²
Flexural strength	30 N/mm²
Density	0.70 g/cm³

The keel models were mounted upside down on a balance in the wind tunnel, this setup is called floor-mounting [22]. The balance, which was mounted on a turntable, measured the forces and the moments in three directions. An additional steel rod was placed behind the balance to support the keel and prevent a large moment on the balance. Both rods penetrated the wind tunnel floor through different slots, see Figure 3.8. The rod that is attached to the keel goes through a slot that is just so big that the rod does not touch the walls and the other rod has a slot that allows the keel to rotate approximately $\pm 5°$ with some safety margin.

Figure 3.7 The keel mounted in the wind tunnel, the keel model in the wind tunnel, a side view of the keel model.

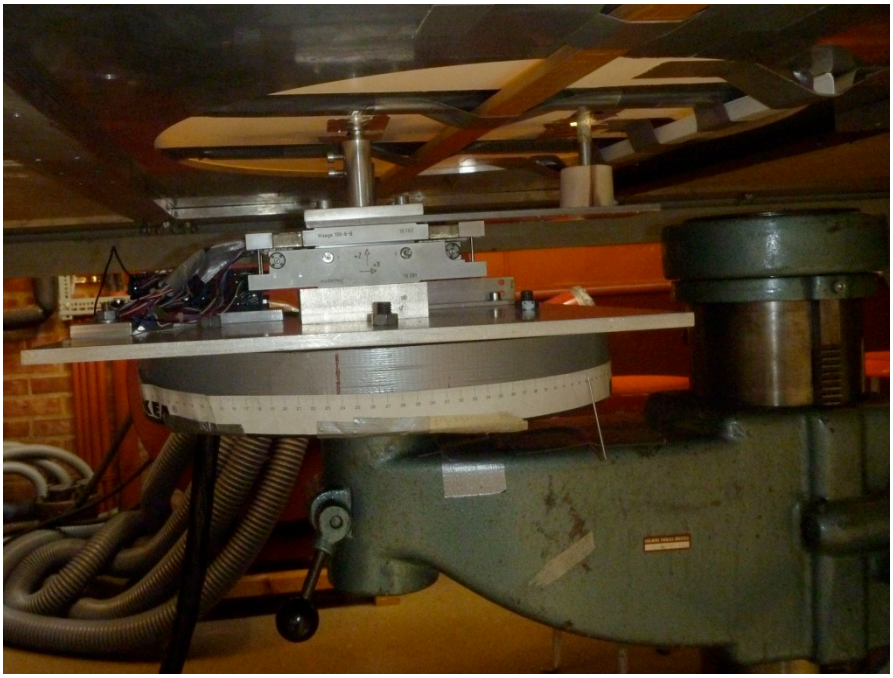

Figure 3.8 The balance setup

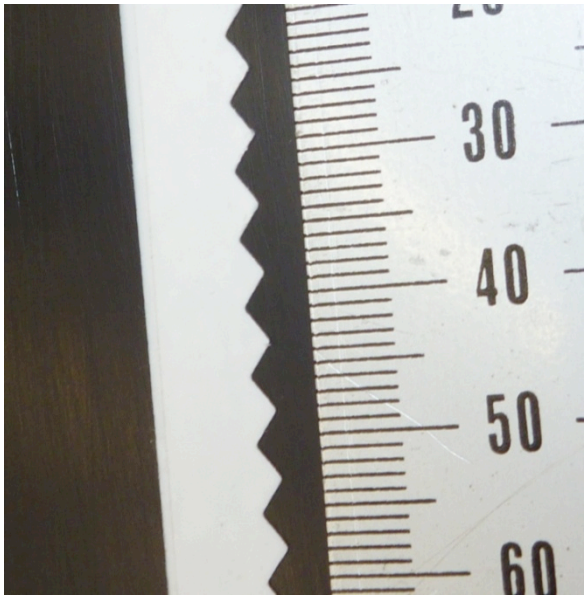

Figure 3.9 Zig-zag tripping tape (the measurement tape is in mm)

In order to trip the boundary layer zig-zag tape were taped on the model, using the recommendation from reference [23], see Figure 3.9. The boundary layer is tripped in order to stabilize the position of the transition and make the flow turbulent. The flow over the keel is modelled as turbulent in the RANS calculations, hence the flow is wanted to be turbulent in the wind tunnel in order to be comparable. The zig-zag tape was taped on a distance of 25% of the total chord and bulb length from the leading edge, although the transition control would be better if the tape was positioned closer to the leading edge, but the risk of destroying the NACA profile would increase by doing that. The thickness of the zig-zag tape was 0.33 mm. A stethoscope was used in order to listen were the transition occurred and see whether the tape worked or not. The stethoscope pipe was dragged along the surface of the keel and a clear disturbing noise arose when at the transition point and that occurred directly after the zig-zag tape.

The CFD calculations for the initial keel design were carried out at model scale as well, hence the friction should be the same in the numerical and experimental tests.

The wind keels were tested at a wind speed of 41 m/s, which resulted in a Reynolds number of:

$$R_n = \frac{UL}{\nu} = \frac{41\frac{m}{s} * 0.396m}{1.56 * 10^{-5}\frac{m^2}{s}} \approx 1.04 * 10^6 \quad (3.3)$$

The reference length L was taken as the mean chord length. The wind speed and the kinematic viscosity are however not constant, both of them are fluctuating. Both the wind speed and the viscosity are monitored and recorded for each force measurement, thus the Reynolds number will vary slightly.

3.3.2 Alignment of the balance, the keel model and the flow

Since the balance is mounted on a rotating turntable it is impossible to know with eye accuracy whether it is in line with the flow or not. A test with a rod could be performed and check when the lift force is zero, but in this thesis the alignment has been done at the analysis stage. When all measurements were done and the drag curve plotted the misalignment between the balance and the flow was obtained from the difference at $\pm 4°$. This was done in accordance with reference [23].

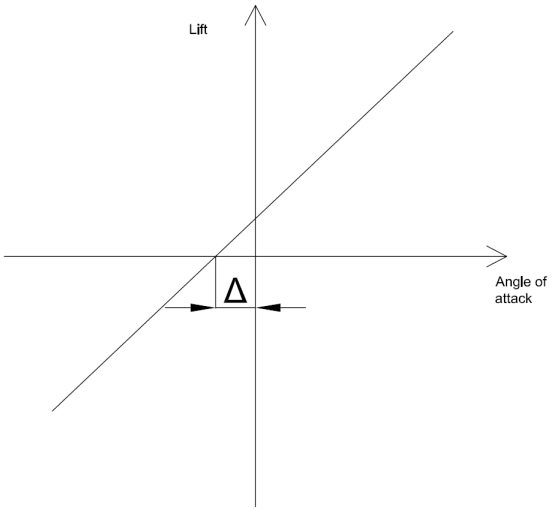

Figure 3.10 Angle correction

The keel placement will neither be exactly aligned with the flow but this can also be corrected in the analysis. The misalignment is denoted with Δ and can be seen in Figure 3.10.

3.3.3 Correction and errors

In the uncertainty analysis of the wind tunnel test only the uncertainties that could be quantified were taken into account. The uncertainties that could be quantified were the bias errors and the precision errors. Bias errors are the systematic errors and the precision errors are due to the precision of the keel setup.

The corrections that were taken into account in the analysis of the results were the blockage effect, the pressure correction, the balance correction and the additional drag from the zig-zag tape.

The manufacturers of the balance are suggesting a correction for the forces in x- and y-direction [24]. Thus the corrected value of the force in x-direction is calculated:

$$F_{x-korr} = F_{x-measured} - \Delta F_x \tag{3.4}$$

And respectively in y-direction:

$$F_{y-korr} = F_{y-measured} - \Delta F_y \tag{3.5}$$

where the correction factors are calculated with equation (3.6) in x-direction and equation (3.7) in y-direction respectively.

$$\Delta F_x = 1.22 * 10^{-05} * \left(F_x{}^2 * 1\right) - 1.24 * 10^{-04} * (F_x * M_z) + 7.99 * 10^{-06} * \left(F_z * M_y\right) - 3.79 * 10^{-05} * \left(F_y * M_z\right) \tag{3.6}$$

$$\Delta F_y = -6.77 * 10^{-05} * \left(F_y * M_z\right) - 1.98 * 10^{-05} * (F_z * M_x) - 7.16 * 10^{-05} * (F_x * M_z) \tag{3.7}$$

M_x, M_y and M_z are the moments in x-, y- and z-direction.
The additional drag the zig-zag tape caused was corrected according to reference [23]. Thus the total drag was corrected with 0.07N.

$$D = D_{measured} - 0.07N \tag{3.8}$$

The blockage effect is due to the fact that the volume of the model is decreasing the area where the air can flow and that the boundary layer is growing along the wind tunnel which makes the wind tunnels effective cross sectional area smaller. The area blocked by the model is called solid blockage and the boundary layer blockage is called the buoyancy blockage. Since the wind tunnel sectional area is gradually increasing to account for the increasing boundary layer thickness this component is zero. The third type of blockage is the wake blockage, which is due to the lower velocity than the free stream velocity in the wake of the keel causing a higher velocity outside the wake in order to maintain a constant mass flow rate.

The solid blockage correction was calculated with equation (3.9) according to reference [25], where k is a factor depending on the shape of the model and it is 0.9 for a three-dimensional wing. ∇_{model} is the volumetric displacement of the model keel and C is the cross sectional area of the wind tunnel, which was 2.04 m^2.

$$\varepsilon_{sb} = \frac{k * \nabla_{model}}{C^{3/2}} = 0.0076 \tag{3.9}$$

The wake blockage was calculated according to Maskell's method [26] with equation (3.10) where the second term can be neglected in a streamlined flow. S is the reference area of the model keel and CD_0 is the profile drag. The flow was assumed to be streamlined in the analysis of the data.

$$\varepsilon_{wb} = \frac{S}{4C}CD_0 + \frac{5S}{4C}(CD_u - CD_i - CD_0) = \frac{S}{4C}CD_0 = 0.00049 \tag{3.10}$$

The wake blockage was very small so it was neglected in the calculations. Hence the solid blockage was the only blockage component added to the velocities. The corrected velocity was calculated:

$$v_{corrected} = (1 + \varepsilon_{sb}) * v_{uncorrected} \tag{3.11}$$

The precision error is caused by the error of the setup, which mean how precise the keel is setup and how precise the angle is set. The precision error was measured with a standard deviation test. The standard deviation was obtained from 10 consecutive tests for the same angle.

The gap between the wind tunnel and the model's root chord has an effect on the drag. A gap of 0.01*span length can increase the induced drag by 31% according to reference [22], but the gap can probably be neglected if it is smaller than 0.005*span. Thus the gap was set to 4 mm which is approximately 0.0054 of the span (span=0.744m), this distance will be small enough to avoid a large additional

uncertainty, but large enough to prevent the keel from touching the floor at higher wind speeds. A test with a 5mm gap was also carried out and the results corresponded very well with the 4mm gap tests.

The effect of the slots for the rods in the wind tunnel floor was also tested by comparing the results of one test series with the used slots to one series with completely taped slots. The result showed that the effect of the slots that was used could be neglected.

All quantified uncertainties that could be quantified can be seen in Table 3.6. The precision of the balance is given by the manufacturers in reference [24] and the calibration error was taken from the deviations when the balance was calibrated. The temperature and static pressure uncertainty was taken from reference [23]. The temperature and static pressure deviation was calculated via the viscosity. The precision error was calculated with the standard deviation from 10 consecutive tests for the same angle, as mentioned before. I was estimated that the angle of the turntable could be set with an eye accuracy of 1/7°. The misalignment error for the balance and the keel (see section 3.3.2) was estimated from the analysis of the data.

Table 3.6 The quantified uncertainties

	Type	Size	Lift Uncertainty [N]	Drag Uncertainty [N]
Balance	Precision		8.75E-02	9.5E-02
Balance	Calibration		1.0E-02	1.0E-02
Temp	Calibration	0.3°	3.5E-03	7.0E-04
Static pressure	Calibration	100Pa	1.5E-03	1.5E-03
Temp dev.	Environment	4°	4.4E-02	8.4E-03
Static pressure dev.	Environment	900Pa	1.3E-02	1.3E-02
Precision	Precision		2.6E-01	2.9E-02
Angle/Balance	Bias	2/70°	2.2E-03	1.99E-02
Angle/Keel	Bias	1/70°	1.1E-03	9.9E-03
TOTAL			**2.78E-01**	**1. 03E-01**

The total uncertainty was taken as the square root of the sum of the squared uncertainties.

$$U_{Total} = \sqrt{\sum_{i=1}^{N} U_i^{\,2}} \tag{3.12}$$

3.4 Velocity Prediction Program

The WinDesign VPP was used in order to get a more understandable performance indicator of the keels. The VPP will take into account the lift and the drag of the keels, but it will also take into account the righting moment. Hence a broader performance indicator will be obtained than just using the C_D/C_L-ratio, which only takes into account the hydrodynamic performance.

The YD40, which is an example yacht designed for Principles of Yacht Design [3], was used for the VPP calculations. The data of the yacht was taken from reference [3] and the keel data was taken from the CAD files and the inserted lift and drag curves were obtained from the CFD calculations.

The particulars of the YD40, that were inserted in the VPP can be seen in Table 3.7, where L_{OA} is the yacht's length over all, B_{MAX} is the maximum beam, SA is the sail area, m_{yacht} is the mass of the yacht without the weight of the keel, SA_{Main} is the sail area of the main sail and SA_{Jib} is the sail area of the jib.

Table 3.7 Main particulars of the YD40 [3]

L_{OA}	12.05m	**m_{yacht}**	4870kg
B_{MAX}	3.71m	**SA_{Main}**	35.5m^2
SA	71.8m^2	**SA_{Jib}**	36.3m^2

The particulars that depend on the keel used can be seen in Table 3.8, where m is the total mass of the yacht, S_W is the wetted surface of the canoe body, T_e is the total effective span, VCG is the total vertical centre of gravity of the boat from the waterline, S_{W_keel} is the scaled wetted surface of the keel and L_{WL} is the length of the water line of the yacht.

Table 3.8 Particulars depending on the keels

	Initial keel	**Optimised keel**
m	7580,45kg	7599.25kg
S_W	25m^2	24.96m^2
T_e	2.348m	2.289m
VCG	-0.1093m	-0.1121m
S_{W_keel}	5.25m^2	4.172m^2
L_{WL}	9.982m	9.976m

The lift and drag forces were inserted into the VPP via the span, wetted surface of the keel and the mean chord. The following method was used when the input data were calculated.

1) The form factor (1+k) was used for scaling the wetted surface in relation to the initial design. Hence the wetted surface for the initial design was its real wetted surface and the wetted surface for the optimised keel was inserted as:

$$S_{w\_opt} = \frac{(1 + k_{opt})}{(1 + k_{ini})} * S_{w\_ini} \tag{3.13}$$

By doing that the profile and viscous drag was taken into account.

2) The form factor was calculated with equation (3.14), where C_{D0} is the drag at zero angle of attack and C_F the total skin friction according to reference [8].

$$(1 + k) = \frac{C_{D0}}{C_F} \tag{3.14}$$

3) The total skin friction C_F was calculated with the ITTC-57 formula [8]. But it was multiplied with the wetted surface and divided with the planform area in order to get the same dimension as the induced drag.

$$C_F = \frac{0.075}{(\log R_n - 2)^2} \tag{3.15}$$

4) The effective span was calculated with equation (2.9) and (2.10), where the induced drag was taken as (C_D and C_L were taken from the CFD calculations):

$$C_{Di} = C_D - C_{D0} \tag{2.1}$$

5) The mean chord was calculated according to equation (2.7)

In the method explained above it is assumed that the viscous drag is increasing quadratically with the lift force, thus the increase in viscous drag is included in the induced drag calculated in step 5 above. The assumption was legitimate because the values followed a parabolic curve quite well when the results were analysed.

4. Results

The results of the grid variation, the CFD calculations of the initial design, the optimisation and the wind tunnel are presented in this chapter.

4.1 Grid variation results

In section 2.2.6 the Factor of Safety method by Xing & Stern [15] and the Least Square Root method by Eça et al. [13], which are the uncertainty analysis methods used in this thesis, are presented. The results of them are presented below. In both methods five grids (Table 3.2) have been used.

4.1.1 Factor of Safety method

Since the FS method is based on triplets the grids that can be used are Grid01, Grid01_5 and Grid02 or Grid01, Grid02 and Grid03. Two tests were carried out one with a refinement ratio of $\sqrt[4]{2}$ (Grid01, Grid01_5 and Grid02) and another with a refinement ratio of $\sqrt{2}$ (Grid01, Grid02 and Grid03).

The convergence ratio R, defined in (2.60), should be between 0 and 1 for the convergence to be monotonic. This condition is not fulfilled for forces Fy_p, Fx_f and Fy_f in the case when Grid01, Grid02 and Grid03 are compared, R for Fy_p is smaller than 0 and for Fx_f and Fy_f it is larger than 1. Although this would not discard the comparison it was decided to use Grid01, Grid01_5 and Grid02 instead, because it will give a more reliable result. The step size between the used grids was constant.

The convergence ratios are between 0 and 1 for every force component for the comparison for Grid01, Grid01_5 and Grid02, which means it converges monotonically according to Xing & Stern [15]. The results can be seen in Table 4.1, where the results of the different force components together with the total drag and lift forces (in this case F_x and F_y) are shown.

Table 4.1 Uncertainty results calculated with the Factor of Safety method

	Fx_p	Fy_p	Fx_f	Fy_f	Fx	Fy
R	0.569157	0.509396	0.584566	0.860721	0.877804	0.510424
p_{RE}	2.374496	4.133128	3.289728	0.919021	0.798599	4.120783
δ_{RE}	0.000475	-0.00062	-0.00018	-6.8E-05	0.00067	-0.00063
P	1.187248	2.066564	1.644864	0.459511	0.399299	2.060392
U_{FS1}	-	-	-	0.00014	0.001414	0.000442
U_{FS2}	0.002216	0.011907	0.00225	-	-	-
U_{FS}	0.002216	0.011907	0.00225	0.00014	0.001414	0.012002
%	14.59%	3.82%	29.52%	66.87%	6.20%	3.85%

The observed order of accuracy p_{RE} is calculated with equation (2.62) and the estimated error δ_{RE} with equation (2.63). The distance metric P is derived with equation (2.64) where the theoretical order of accuracy $p_{th}=2$.

The final uncertainty U_{FS} is chosen from U_{FS1} (calculated with the upper equation in equation (2.66)) and U_{FS2} (calculated with the lower equation in equation (2.66)), which depend on the distance metric, equation (2.66). The percentage value in the end of Table 4.1 is the uncertainty in percentage of the obtained result. It can be seen that the frictional force components Fx_f and Fy_f have a large uncertainty but since they have small influence on the total force, the total forces Fx and Fy have a much smaller uncertainty. The errors for the different force components seem to have cancelled out each other as well.

4.1.2 Least Square Root method

The LSR-method requires at least 4 grids [14] so 4 or 5 grids from Table 3.2 will be used. The method neglects the iterative error and requires that the iterative error is at least two orders of magnitude smaller than the grid discretization error and this requirement is fulfilled for all the grids, however the scatter of the points was very large when 5 grids were used, which would make the curve fit very difficult. Thus only 4 grids (Grid01, Grid01_5, Grid02 and Grid02_5) were used for the comparison in the uncertainty analysis.

A curve was fitted to the results using equation (2.61), equation (2.68) and (2.69) and this was performed for the force components in x- and y-direction and also for the total lift and drag force. The result for the pressure component of the force in x-direction can be seen in Figure 4.1 and a complete overview over the curve fits can be seen in APPENDIX 1. The curve fits for three grids have also been plotted for comparison and both curves are plotted against h_i/h_1. The computational results for the four grids can also be seen in the graphs (the four triangles).

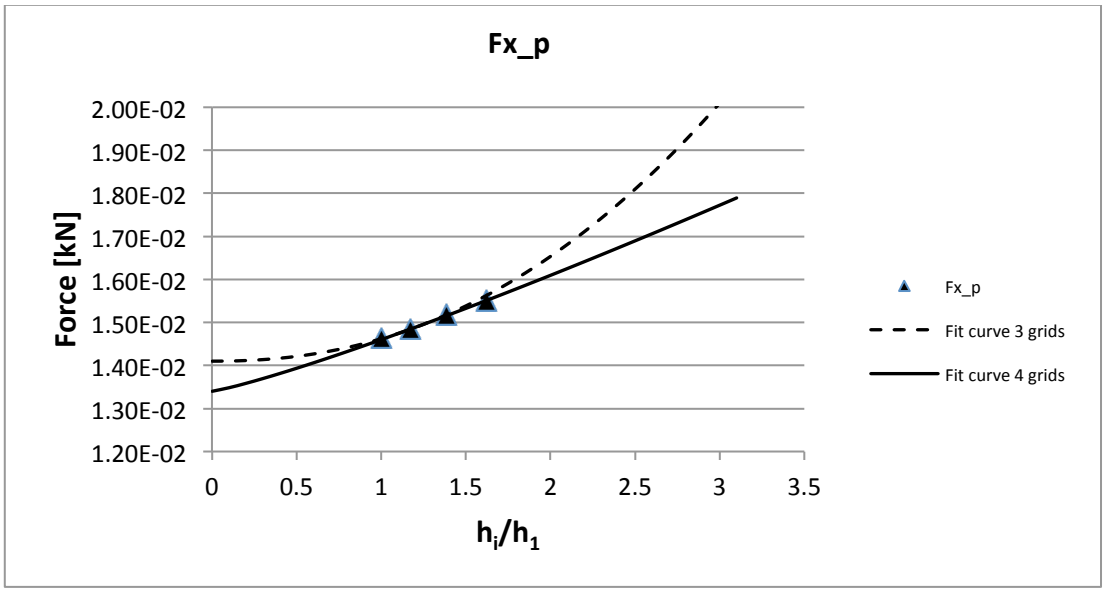

Figure 4.1 Curve fits for the pressure component of the force in x-direction

The observed order of accuracy p, the constant α and the estimated exact solution ϕ_o was obtained from the curve fits. The order of accuracy for the different forces,

which also decides the convergence type, can be seen in Table 4.2. The standard deviations (U_S, U_{S02} and U_{S02}) calculated for the different discretization errors (equation (2.61), (2.68) and (2.69)) were calculated with equation (2.76) and the result can be seen in Table 4.2. The different error estimators are denoted δ_{RE}, δ_{RE02}, δ_{RE12} and $\delta_{\Delta M}$ and the final uncertainty using the LSR-method is denoted U_{LSR}. The uncertainty in percentage of the obtained result can be seen in the end of the table.

Table 4.2 Uncertainty analysis results obtained with the LSR-method

	Fx_p	Fy_p	Fx_f	Fy_f	Fx	Fy
p	1,17E+00	-1,89E+00	1,67E+00	1,68E+00	1,67E+00	-2,28E+00
δ_{RE}	1,76E-03	-	-8,49E-04	-5,46E-05	3,91E-04	-
δ_{RE02}	1,05E-03	-2,31E-03	-7,21E-04	-4,65E-05	3,30E-04	-2,31E-03
δ_{RE12}	1,85E-03	-1,25E-02	-8,08E-04	-7,57E-05	1,04E-03	-1,25E-02
$\delta_{\Delta M}$	2,48E-03	2,97E-03	1,01E-03	6,87E-05	1,46E-03	3,02E-03
U_S	4,42E-05	-	1,66E-05	8,92E-07	3,10E-05	-
U_{S02}	4,41E-05	6,05E-04	9,04E-05	1,48E-06	3,50E-05	5,98E-04
U_{S12}	2,10E-05	3,32E-04	1,57E-05	4,29E-07	5,21E-06	3,32E-04
U_{LSR}	2,24E-03	3,73E-02	1,04E-03	6,74E-05	5,20E-04	3,73E-02
%	14,75 %	11,95 %	13,71 %	32,22 %	2,28 %	11,95 %

It can be observed that the uncertainties for Fx_p, Fy_p and Fx_f are all in the same range while the Fy_f is a bit larger. As for the FS-method the errors for the different components seem to cancel out each other.

4.2 Results from the initial design

The results of the CFD calculations for the keel with the initial design will be presented in this section.

In Figure 4.2 the magnitude of the total velocities are plotted. Two vortices are built up around the bulb. The first one starts on the suction side just above the bottom (see the two lower pictures in Figure 4.2) and it is created after the thickest part of the bulb. The second one is built up earlier on the pressure side (upper left picture in Figure 4.2) but it moves up above the edge after the thickest part of the bulb (upper right picture in Figure 4.2). A more detailed picture series of the development of the vortices and the total velocities can be seen in APPENDIX 3 (the slices are plotted at 10 cm interval from the leading edge backwards). The total velocities are plotted in Figure 4.2 and the scale can be seen on the right hand side of the pictures. The vortex on the pressure side rotates clockwise and the vortex on the suction side rotates counter clockwise looking in the flow direction, see Figure 4.3. The two vortices are merged together at the aft part of the keel and a large wake is developed.

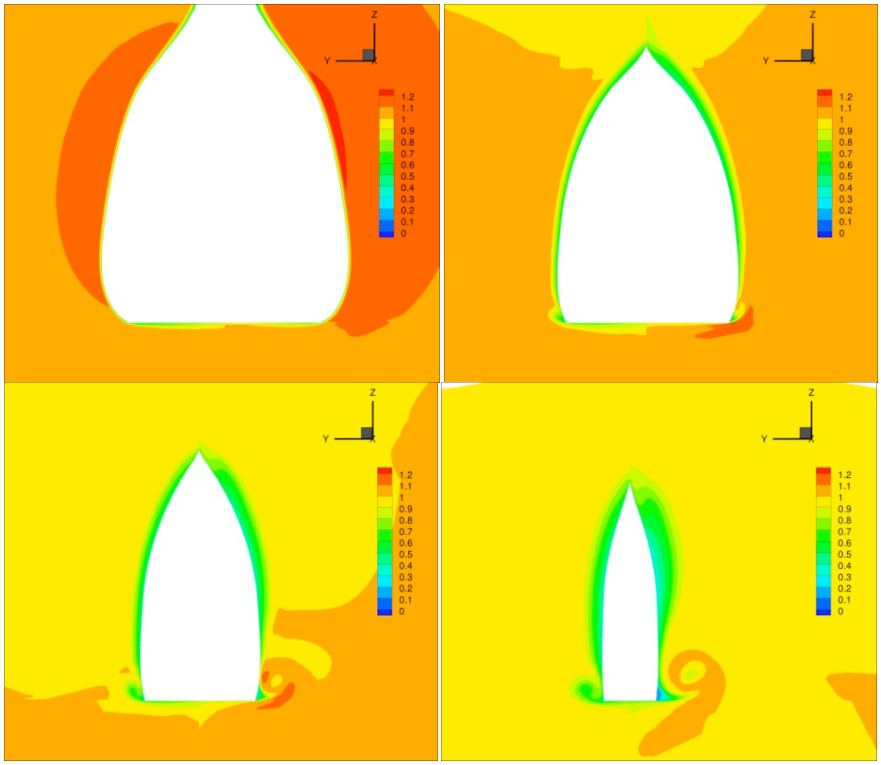

Figure 4.2 The development of the vortices, the total velocities are plotted.

The boundary layer is thin around the bulb at the beginning of the bulb, but after the thickest part it is growing gradually until it separates at the aft part of the bulb.

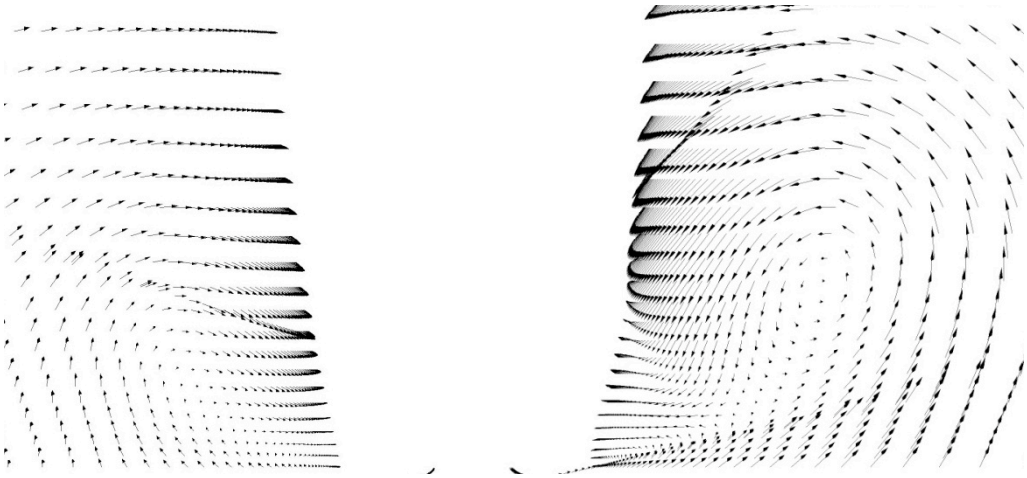

Figure 4.3 The contra rotating vortices on pressure (left) and suction side (right)

The pressure distribution on the surface of the keel can be seen in Figure 4.4, both pressure and suction side are displayed. The pressure coefficient $C_{P,}$ which is presented in the figure, is varying between -1 and 1.

It can be seen that the stagnation area where the pressure is high (red colour) at the leading edge is larger at the bulb than at the fin part. The pressure is decreasing after the leading edge on the pressure side and the lowest pressure can be observed at the middle part of the side. A low pressure area occurs at the bottom of the leading edge under the stagnation area.

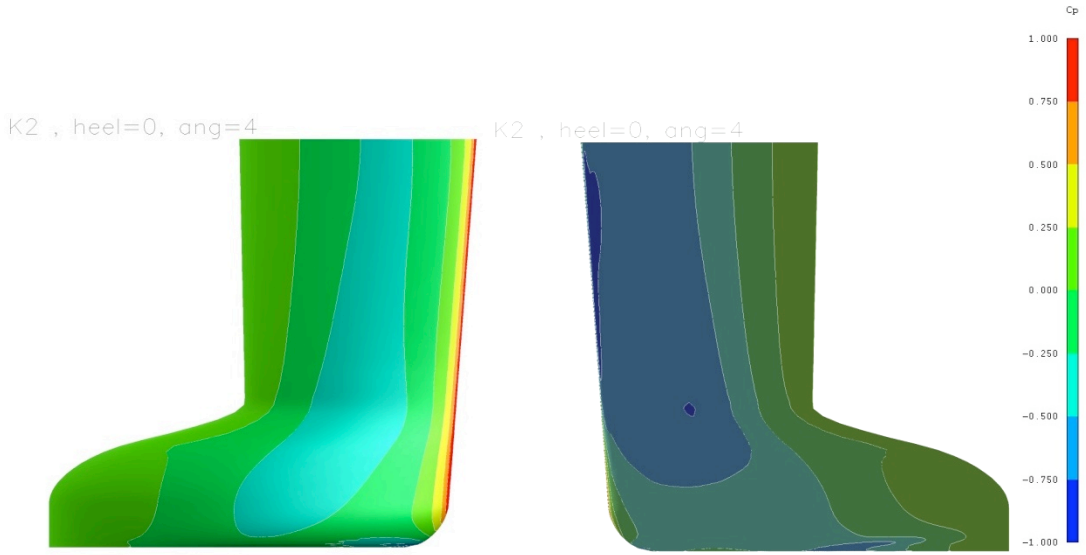

Figure 4.4 Pressure distribution on the pressure side (left) and the suction side (right)

A large suction area with very low pressure occurs directly after the leading edge on the suction side. This area fades out after a while into a more neutral pressure. A low pressure area appears as well at the bottom of the bulb.

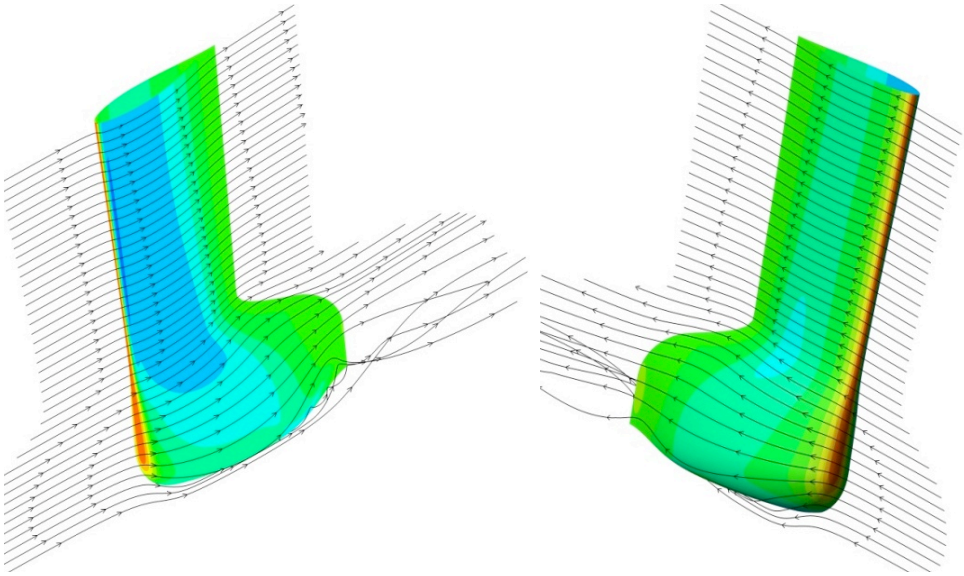

Figure 4.5 Streamlines plotted on pressure distribution

It can be seen in Figure 4.5, that the streamlines follow the keel surface on the pressure side (right) while the separation can clearly be seen on the lower part of the bulb on the suction side (left), which also could be seen in Figure 4.6. The streamlines are well attached on the fin part of the keel at both sides.

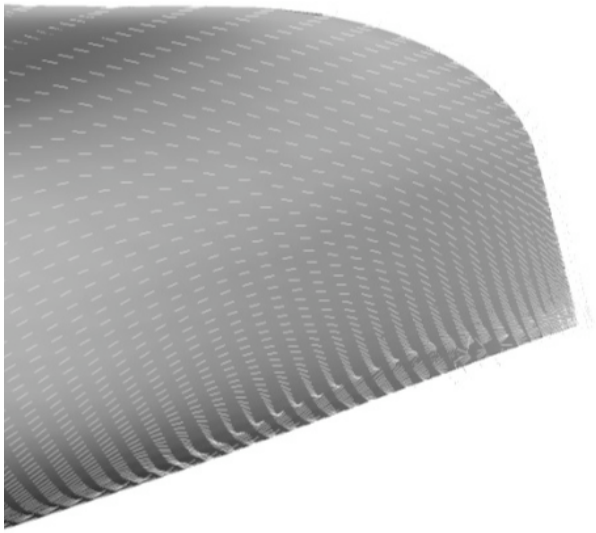

Figure 4.6 Separation at the suction side

It can also clearly be seen in the vector plot (Figure 4.6) that the flow separation starts at the lower part of the bulb on the suction side. The separation will start at an earlier position at larger angles of attack.

The reason to the different phenomena will be discussed in section 5.1.3.

4.2.1 Lift and drag

The results from the lift and drag forces were taken as an average of the last 10% of the iterations. The force components that were recorded were the pressure forces in x and y-direction and the frictional forces in x- and y-direction. The pressure force consists of the induced drag and profile drag in x-direction and the pressure difference causes the lift in y-direction. The frictional force in x-direction is caused by the friction of the wetted surface.

The graphs of how the forces converged can be seen in Figure 4.7 and it is noticed that the standard deviation was less than 0.06% of the average forces. The number of iterations has been divided by a factor of ten; hence it was 4500. The total residuals can be seen in Figure 4.8. It can be seen in the graph that the residuals are decreasing by 3 orders of magnitude, which is a satisfactory decrease.

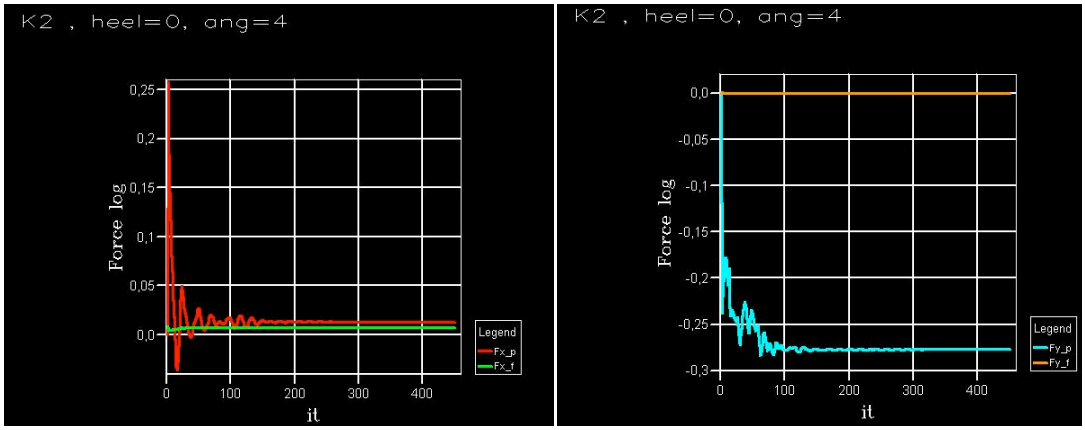

Figure 4.7 Convergence of the forces in x- and y-direction

The pressure force in x-direction was 13N and -277N in y-direction and the frictional force in x-direction was 7.6N and 0.2N in y-direction. This gave a total drag force of 21N and the total lift force was 277N. Thus the drag coefficient C_D was 0.0226 obtained with equation (2.6) and the lift coefficient C_L=0.301 was obtained respectively with equation (2.5). A planform area of 1.8414m^2 was used in the calculations. Finally the drag-lift coefficient ratio was obtained C_D/C_L=0.07502.

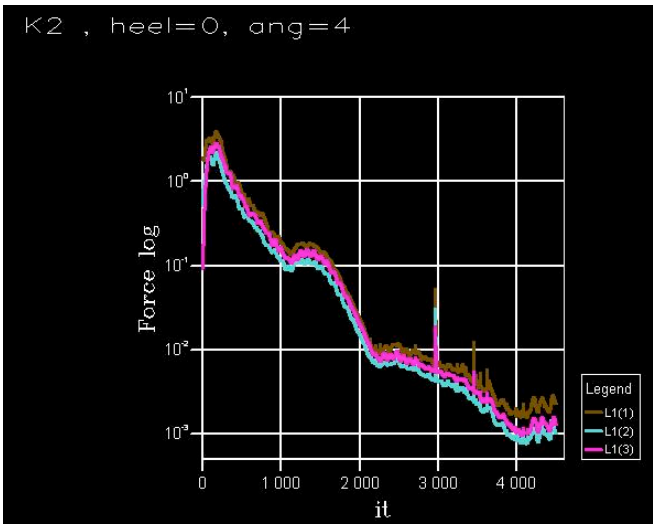

Figure 4.8 Residuals

4.3 Results from the optimisation

The results from the optimisation will be presented in this section. The lift and drag forces of the new optimised keel will be presented together with the vortex development and the pressure distribution over the keel surface.

Figure 4.9 Profile and front view of the optimised keel

The shape of the optimised keel can be seen in Figure 4.9 and Figure 4.10. The shape of the bulb is quite round with a narrow flat area at the bottom. The final weight of the keel was 2729.25kg and the vertical centre of gravity was -1.26454m, which gave a moment of 34.51kN, according to equation (3.2).

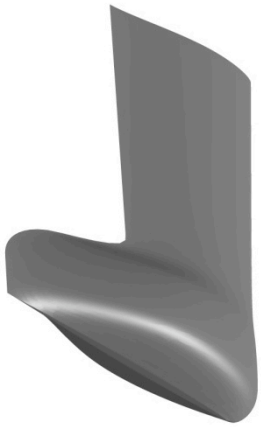

Figure 4.10 Fish-eye view of the optimised keel

4.3.1 Convergence

The final values for the design variables for the optimised keel are shown in Table 4.3 and the initial values and the side constraints are also displayed for comparison. The variables are explained in section 3.2.2.

Table 4.3The design variables from the initial and the optimised design together with the side constraints.

Variable	Lower limit	Initial value	Optimised value	Upper limit
TC05andTC5b_X	0	0	0.005368	0.07
TC05b_Z	-1.55	-1.51	-1.48311	-1.3
TC05_Z	-1.7	-1.65	-1.69989	-1.65
TC06_X	0.06	0.14	0.116844	0.2
TC06_Z	-1.86	-1.81	-1.78534	-1.7
TC07_X	0	0.12	0.013003	0.15
3DPoint02_X	-1.1	-0.8665	-0.95115	-0.6

The convergence of the CD/CL-ratio is displayed in Figure 4.11. The chosen variant is marked with des0068 and the variants that were violating the constraints are not displayed. The lines in the graph are the fitted curves. The straight line is the linear fitted curve and the square fitted curve. The optimisation was stopped after 146 variants, when 10 generations had been completed, although 6 variants from the 11th generation were used in the results. 47 of the variants were violating the constraints and a penalty was given to them. A complete overview over the convergence of the different design variables can be seen in APPENDIX 6.

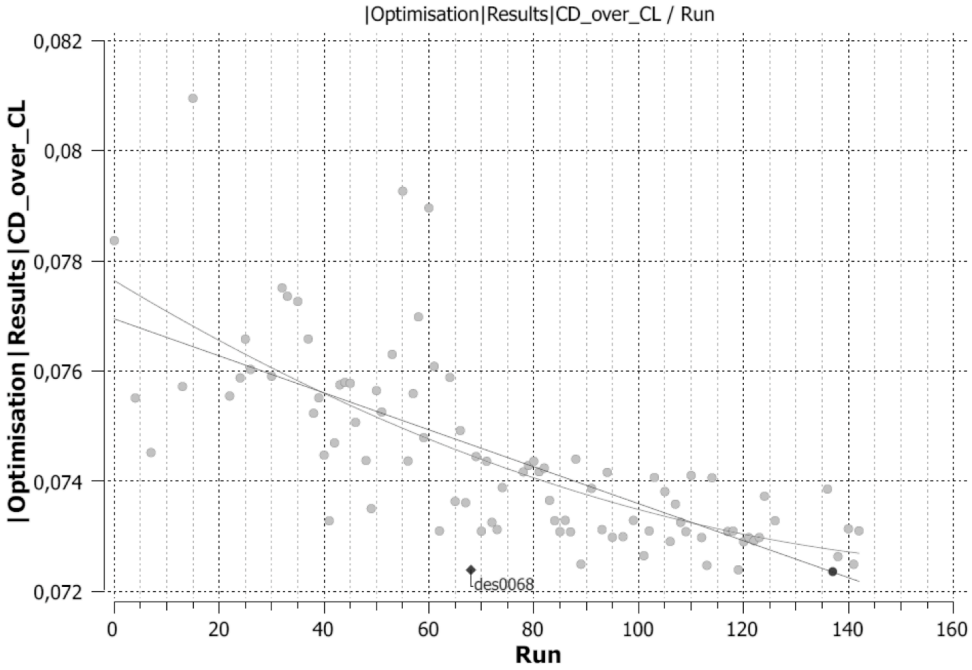

Figure 4.11 The convergence of CD/CL-ratio. The variants that were violating the constraints are not displayed

.

4.3.2 Lift and drag

The optimised keel was scaled with the same planform area (1.8414 m^2) as the initial design in order to get the lift and drag coefficients. By doing this the keels were more comparable and the planform was taken as the mean chord multiplied by the keel span, therefore their planform area was the same. The keels projected lateral area was however not the same.

The drag force pressure component was 10.9N and the frictional component was respectively 8.28N, which gave a total drag force of 19.2N and a drag coefficient of 0.02088. The corresponding lift force components were -266.N (pressure) and 0.11N (friction) giving a total lift force of -266N and a lift coefficient of 0.2884. Thus the C_D/C_L-ratio was equal to 0.07239.

4.3.3 Vortex development

The total velocity magnitudes around the optimised keel can be seen in Figure 4.12. The pictures are taken from the same x-coordinates as the pictures in Figure 4.2. The total plots of the flow over the bulb can be seen in APPENDIX 4.

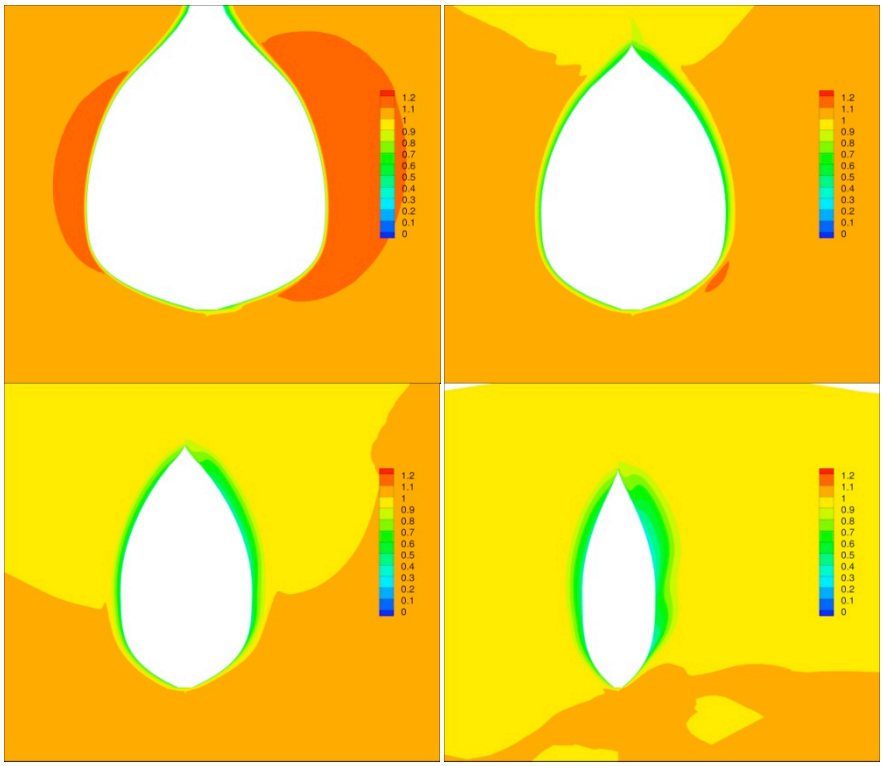

Figure 4.12 Flow around the optimised bulb. The total velocities are shown

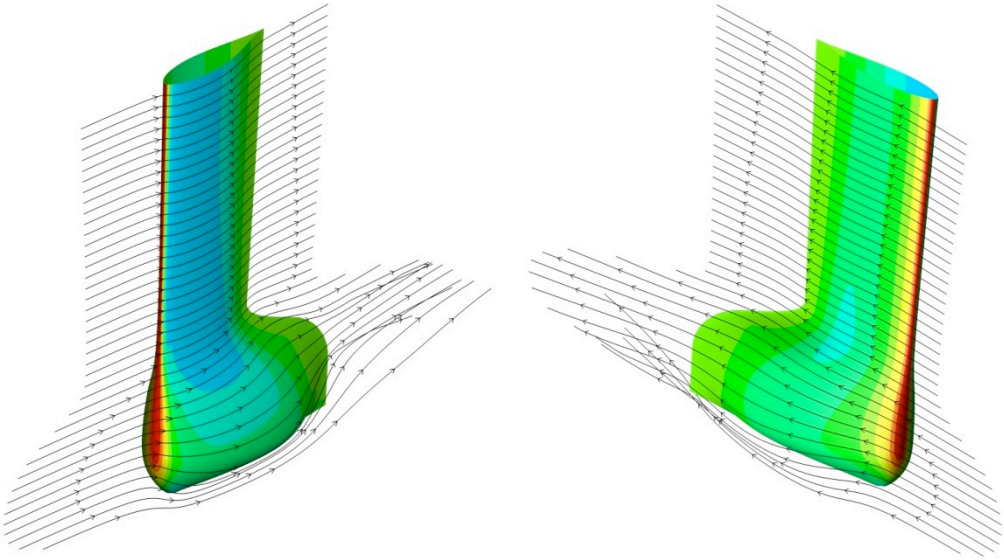

Figure 4.13 Streamline plots of the optimised keel

The streamline plots for the optimised keel can be seen in Figure 4.13. The pressure distributions are also plotted in the pictures. The results of the optimised keel will be discussed in section 5.1.3.

4.3.4 Pressure distribution

The pressure distribution of the optimised keel can be seen in Figure 4.14. The stagnation area is bigger in this case as well at the bulb and a lower pressure area can be observed at the mid part of the pressure side. The low pressure area at the suction

side is strongest just behind the leading edge and it fades gradually towards the trailing edge.

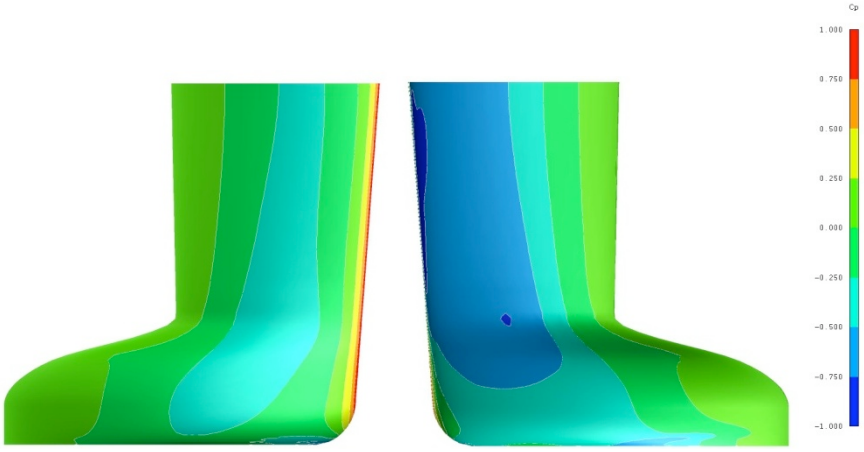

Figure 4.14 Pressure distribution on pressure (left) and suction (right) side

4.4 VPP results

Both keels were attached on the YD-40 hull and tested on a virtual Olympic sailing course in the VPP program. The course was 0.5nm (nautical mile) upwind and 0.5nm downwind. The results for the race can be seen in Figure 4.15, the final course time is plotted for different true wind speeds.

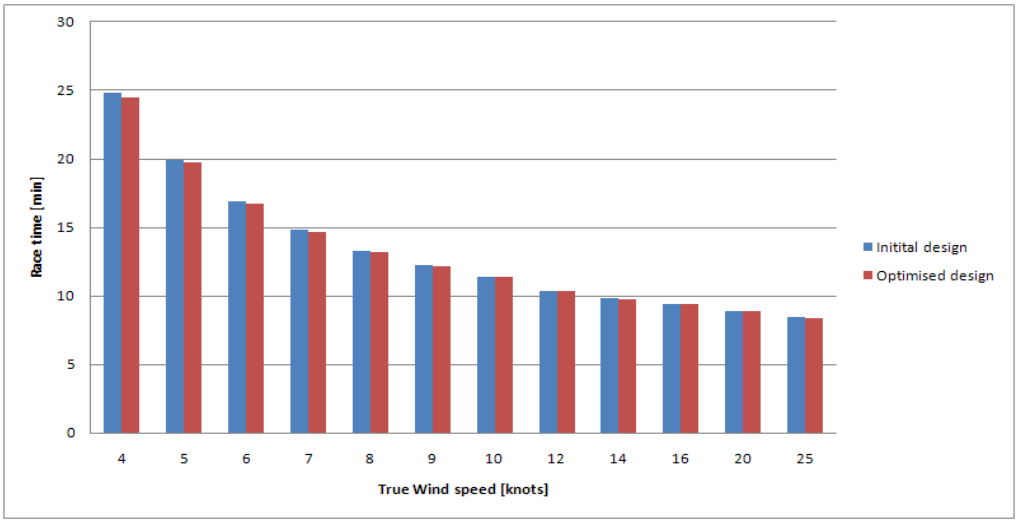

Figure 4.15 The results for the two different keels on an Olympic sail course

4.5 Wind tunnel results

The obtained wind tunnel results was analysed according to section 3.3 where the uncertainty is also calculated.

The drag coefficient results from three combined test can be seen in Figure 4.16, where the trendline is plotted as well.

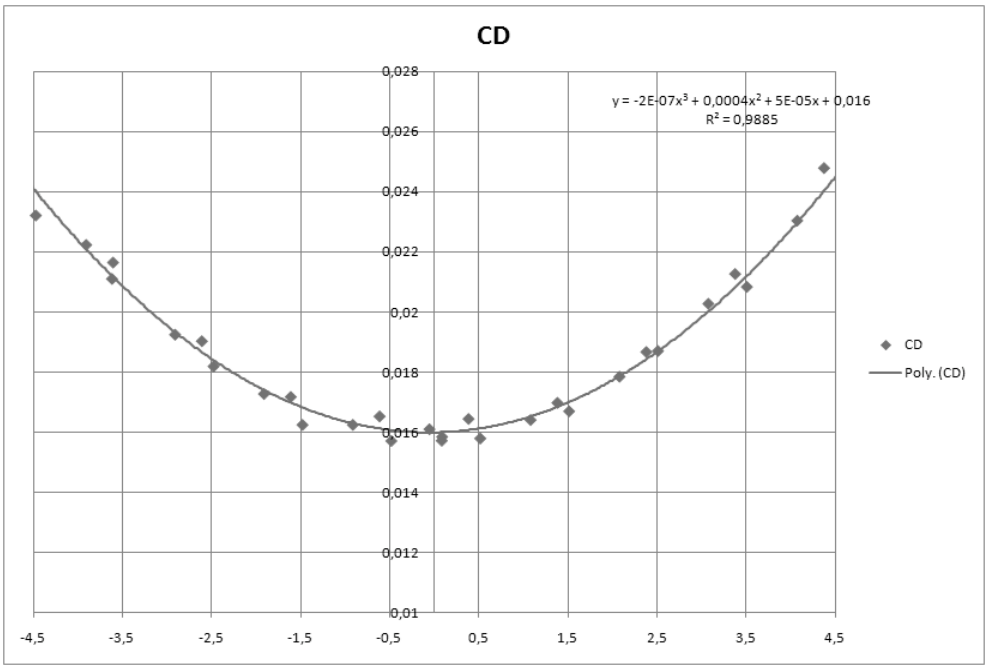

Figure 4.16 Drag plot from three combined test series

The drag coefficient for 0 degrees is 0.016 and for ±4 degrees it is 0.0224. The corresponding forces were 4.92N±0.103 for 0 degrees and 6.88N±0.103 for ±4 degrees if a velocity of 41.9m/s and a density of 1.186kg/m^3 were used. Some scatter in the results can be seen.

The lift coefficient results are displayed in Figure 4.17, the results were also obtained from three test series.

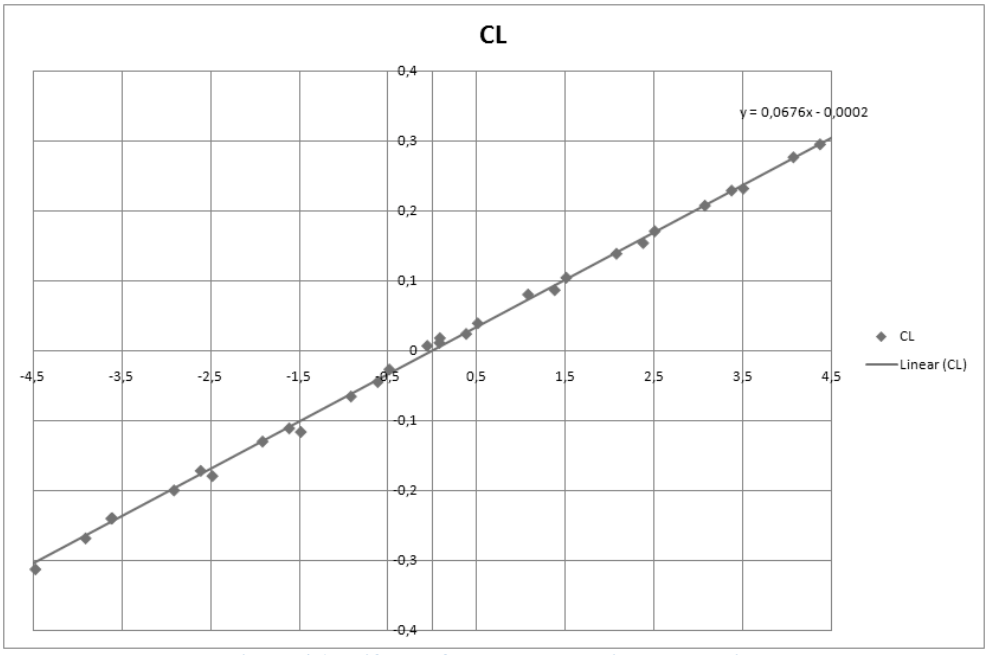

Figure 4.17 Lift plot from three combined test series

The lift coefficient for 0 degrees is 0 and for ±4 degrees it is 0.2704. The corresponding forces were 0N±0.103 for 0 degrees and 83.1N±0.103 for ±4 degrees if a velocity of 41.9m/s and a density of 1.186kg/m^3 were used. Some scatter in the results can be seen.

5. Discussion

5.1.1 Uncertainty analysis

Both methods that have been used in this thesis for the uncertainty analysis are accepted in the hydrodynamic society (Workshop on Numerical Ship Hydrodynamics, Gothenburg 2010), even if the authors of the methods disagree with each other. It must also be emphasised that both methods have mostly been tested on generic cases. However the results from the LSR-method were chosen for the final uncertainty. The reason for choosing the LSR-methods over the FS-method was that it uses at least four grids while the FS-method used only triplets. It can be seen in APPENDIX 1 that the results in between 3 and 4 grids vary a lot and even if LSR-method should not be used with less than 4 grids it shows an indication on how the result differs depending on the number of grids. Furthermore the FS-method does not take the grid refinement round-off error into account, which causes scatter in the solutions, when refining the grids. The grid refinement round-off error occurs when refining the grid with a refinement ratio ($\sqrt[4]{2}$ used in this thesis), the results will have decimals and cell numbers cannot be decimal numbers so they have to be rounded and this will create an error for every refinement. Hence the aspect ratio of the cells will vary between the grids. There are also other reasons for the scatter in the refinements plots such as limit of the turbulence models, limiters in the discretization scheme and priority changes in the overlapping regions.
Thus the final uncertainty can be seen in Table 4.2 where it can be seen that the pressure forces have an uncertainty of Fx_p=14.75% and Fy_p=11.95% respectively, while the frictional force have an uncertainty of Fx_f=13.71% and Fy_f=32.22%. The uncertainty of the frictional force in y-direction is very large in proportion to the actual force component, however the frictional component has very little influence on the total lift and this can be emphasised looking at the uncertainty of the total lift force, Fy=11.95%. The uncertainty of the total drag force was very low, Fx=2.28%.

5.1.2 Optimisation

The NSGA-II has actually been developed for multi objective optimisation, however the advantages of the algorithm can also be used in single objective optimisation. The 7 design variables used in the optimisation makes a relatively large design space and the risk of finding a local optimum with a gradient-based algorithm would have been large in such a large design space. Thus the NSGA-II was a convenient choice since its advantage is that it can find many optima and even when it starts to converge to a design it will also look in other areas of the design space, due to the crowded comparison approach, explained in section 2.3.2. A gradient-based search could have been done starting from the results from the NSGA-II, but that was not included in the scope of the work.

The generation of the grid using the rudder module was shown to be a very effective way of setting up the grid in an optimisation process. The shape could be varied easily with the scaling of the profiles and still have the same grid setup and the same number of cells. However this setup has its limitations for keel shapes and the grid will not be perfect, see section 5.1.4. The rudder module has its limitations since it is using sections for the generation of the grid, it could be difficult to model for

instance the L-bulb and T-bulb keel from reference [2] due to the sharp intersection between the bulb and the keel.

The given penalty of C_D/C_L=0.1 that was given to the variants that violated the constraints was shown to have an effect on the algorithm. The algorithm seemed to converge to less effective designs than the initial design. Due to this the side constraints for the variants had to be decreased, so the variants had less freedom. Hence the design space was also decreased. Thus this kind of setup for the optimisation requires very carefully set limitations and constraints. One way to improve the results would be to not use the penalty and let the calculations be performed for the violated constraints as well. By doing this the algorithm will have a better picture of the design space. However this would require more computational time and the optimisation required already with the used setup approximately 10 days. The penalty might also have an effect on the results close to the border of the inequality constraints. If the inequality constraint is violated the C_D/C_L=0.1, which means that the algorithm will treat it as a bad variant. However a good design might exist at the other side of the border of the inequality constraint and because the violated variant is treated as a bad variant the algorithm will not look in that area and some good variants might be missed.

It can be seen in the convergence plots in APPENDIX 6 that the algorithm was searching in a large part of the design space and it converged to two different optima. This justifies the choice of the NSGA-II.

The final design was chosen based on the objective function, however the variant with 2nd lowest C_D/C_L-ratio was approximately 80 kg lighter than the variant with the lowest C_D/C_L-ratio, thus it was chosen as the final design.

5.1.3 Design comparison

The initial keel design

From the results for the initial keel design in section 4.2 and the picture series in APPENDIX 3 it can be seen that two vortices are developed on each side of the bulb. The vortex on the suction side was expected, this vortex is also built up on a conventional fin keel [3] and it is developed due to the pressure difference on both sides. This vortex has a large influence on the effective aspect ratio. A vortex higher up will reduce the effective aspect ratio. The vortex on the pressure side does not occur above the edge on a flow around conventional fin keels. The fact that it is above the edge of the bulb is a peculiar phenomenon. On a conventional keel with sharp tip edges a vortex is developed just under the tip on the pressure side due to the sharp edge, this same vortex occurs for the initial keel design but once the keel starts to become narrower after the thickest part the vortex moves up above the edge.

One reason for this phenomenon is probably that the angle of the flow (angle of attack) is smaller than the angle of the bulb side after the thickest part. Hence the flow flows out at the pressure side as well and not only the suction side, see Figure 5.1. If the angle of attack was larger the flow would be sucked up on the suction side or leave the keel at the trailing edge due to the angle of the flow.

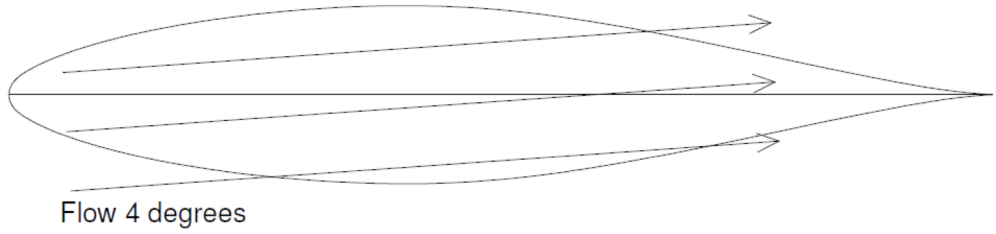

Figure 5.1 The development of the vortex above the bulb edge on the pressure side.

The advantage of the integrated bulb keel compared to other bulb keels is that it provides additional lift, however the wetted surface is also increased so the drag is also increased. The initial keel design has a relatively high lift and drag coefficient giving a C_D/C_L ratio of 0.07502.

Comparison

The optimised keel was longer and had a more round section shape than the initial design (see Figure 5.3). The wide bottom surface was also decreased as can be seen in Figure 5.2, however a narrow part of the bottom still have this plane bottom part with sharp edges.

Figure 5.2 Front view of the initial (left) and optimised (right) keel design

It is a very interesting phenomenon that the optimised design has this narrow plane bottom part, because the sharp edge of it is probably preventing the vortex moving from the pressure to the section side to move far up on the suction side. This could be an indication that the same rules apply for a bulb keel as for a fin keel. In section 2.1 the effects of the tip on a fin keel is explained and it is stated that a tip with sharp edges is the best tip shape. The results from the optimisation indicate that this could be applied on bulb keels as well. Hence even if the bulb has a round shape, it is worth having a sharp tip at the bulb in order to prevent the overflow.

Figure 5.3 Profile view of the initial (left) and optimised (right) keel design

The flow pictures for the optimised keel in Figure 4.12 and in APPENDIX 4 show no sign of the vortices that are developed around the initial keel. In APPENDIX 5, where the u-velocity is plotted with the flow vectors, a small rotational movement on the suction side can be seen for the optimised keel. The vortex could be seen more clearly if the chosen contours were finer. Thus these vortices are much smaller than the vortices on the initial design and therefore leaving a smaller wake, which will decrease the induced drag. This is also indicated in the force results presented in section 4.3.2. The pressure drag has decreased while the frictional drag has had a small increase due to the fact that the optimised keel has a larger wetted surface. The lift has also decreased, but the ratio between the lift and drag has of course increased and the important performance indicator is the lift for a given drag. The C_L/C_D-ratio was increased by 3.6%, the lift decreased by 4.2% and the drag decreased by 7.5%. The initial design of the keel had a vertical wall on the side of the bulb (see Figure 5.2) this side provided additional lift to the keel. But the additional lift that the wall provides also seems to increase the drag and it is therefore taken away as can be seen from the optimisation results.

It can be seen in the plots in APPENDIX 3 and APPENDIX 4 that the boundary layer looks very similar before it separates, but the wake behind the optimised keel design is more regular.
The flow was very well attached at the suction side on the optimised keel and the separation was not as obvious as on the initial keel design. The difference can clearly be seen in Figure 5.4, where the initial design is plotted on the left side and the optimised design on the right side. The phenomenon with the flow moving up above the bulb edge did not occur on the optimised keel like it did on the original design.

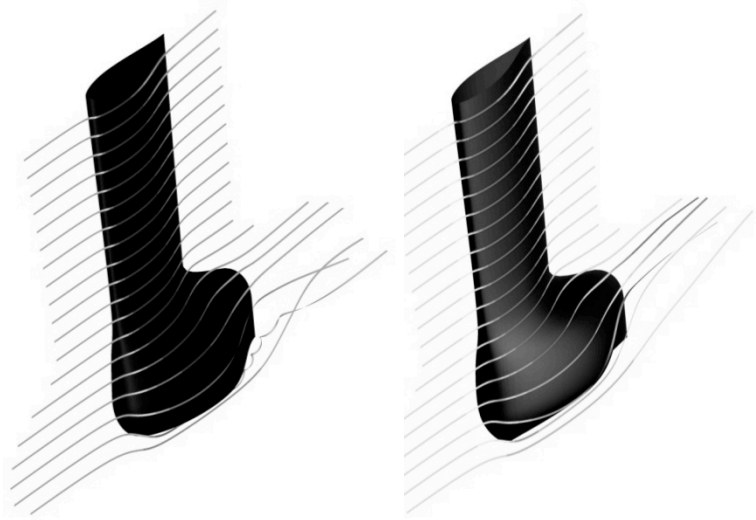

Figure 5.4 The separation of the flow at the suction side

It is not possible to draw the conclusion that a bulb keel should have a sharp tip because this might only be a coincidence, but the relation between the fin keel and the bulb keels seems to be very likely.

VPP comparison

It can be seen in the VPP result that the optimised keel was better in all true wind speeds except at the true wind speed of 20 knots where the course times were the same. The differences are not very large, around 10 seconds at lower wind speeds and only 1-3 seconds at higher wind speeds. 10 seconds gain on a 1nm course can make a substantial difference in a real sail race. Hence, it may be worth optimising the keel for a performance cruiser. It may be questioned whether an optimisation of a keel is necessary for a pleasure cruiser since the differences was so small in the race.
The optimised keel was 18.8kg heavier and had a little higher vertical centre of gravity. But because the keel was heavier it lowered the total vertical centre of gravity for the YD-40, hence giving a better righting moment.

5.1.4 Problem area in the mesh

A problem area occurred in the grid due to the method that was used for creating the grid. The grid was not as smooth as wanted at the leading edge of the bulb, just above the bottom, see Figure 5.5. This area has probably had a small effect on the results as can be seen in Figure 4.4. It was tried to make a denser grid to avoid the sharp edge but without success, one way to avoid this problem would have been to use another grid generator and build up the grid with a blocking technique, but in that case the good optimisation properties of the used rudder module would have been lost.

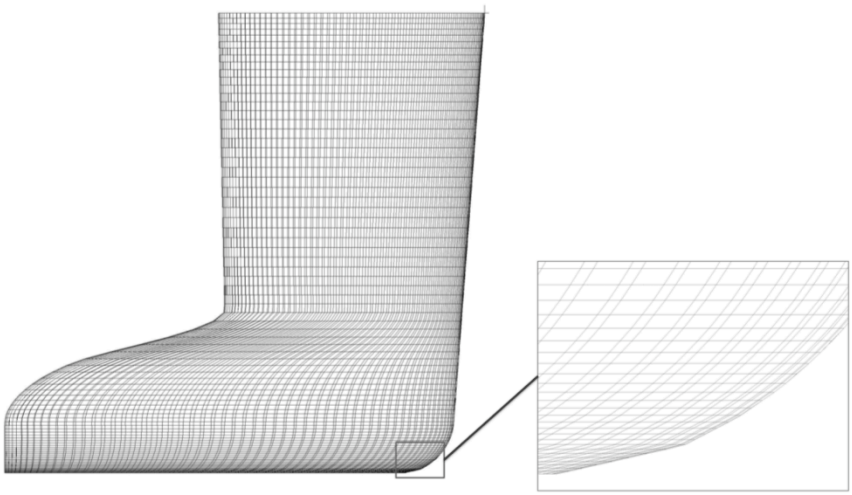

Figure 5.5 Problem area in the grid

5.1.5 Comparison between the numerical and experimental results

The wind tunnel tests were compared to the CFD calculations at model scale, hence the same Reynolds number was used in the experimental and the numerical tests, $R_n=1.04*10^6$ (the mean chord was used as reference length, 0.396m). There are of course differences between the CFD calculations in full scale and model scale, but it was assumed that the RANS solver calculates with the same accuracy similar problems with the same grid structure but with different Reynolds numbers. Since the wind tunnel tests were taken in three different series with very little variation between the series the repeatability of the tests can be seen as successful. The results from the CFD calculations (model scale) and the experimental tests obtained in the wind tunnel can be seen in Table 5.1. The drag and lift coefficients are compared followed by the C_L/C_D-ratio at 4 degrees angle of attack.

Table 5.1 Comparison between CFD calculations (model scale) and wind tunnel tests at 4 degrees angle of attack.

	CFD (model scale)	Experimental
C_D	0.0247	0.0224
C_L	0.2957	0.2704
C_L/C_D	11.972	12.071

The CFD result is approximately 10% larger for both the drag coefficient C_D and the lift coefficient C_L. While the C_L/C_D-ratio is differs with less than 1%. The fact that the difference between the C_L/C_D-ratio in the experimental and the numerical tests are within 1 % should be consider as a good result, even though the lift and drag forces are over predicted in the CFD calculations. The C_L/C_D-ratio is one of the most important hydrodynamic performance indicators. It is important to know at the design stage of a sailing yacht how much drag a certain keel has for a given lift.

The corresponding forces to the force coefficients are 6.88N±0.103N for the drag and 83.08N±0.278N for the lift in the experimental tests and 7.59N±0.2125N for the drag and 90.85N±10.86N for the lift in the numerical tests. The forces have been calculated using a velocity of 41.93 m/s and a density of 1.1864 kg/m3. The

numerical uncertainties have been calculated using the percentage values in section 4.1.2. The comparison errors are obtained with equation (2.78), so E_{drag}=7.59N-6.88N=0.71N and E_{lift}=90.85N-83.08N=7.77N. The validation uncertainties are U_{val_drag} =0.236N and U_{val_lift}=10.86N, calculated with equation (2.77). The parameter uncertainty is equal to zero due to the strong model concept. The lift force solution is validated because $E_{lift} < U_{val\_lift}$ but the drag force is not because $E_{drag} > U_{val\_drag}$.

At zero degrees angle of attack the drag coefficient was 0.01656 in the numerical tests and 0.016 in the wind tunnel test, which is a 3.4% difference. Because the difference of the drag coefficients was smaller at 0° angle of attack than 4° angle of attack, it can be assumed that the induced drag or the profile drag is over predicted in the numerical calculations, because the friction component in the drag force is kept almost constant between 0° and 4° angles of attack. The induced drag has the biggest change because it is zero at 0° angles of attack, thus it has probably a bigger effect on the over prediction than the profile drag.

One error that could not be quantified and was not taken into account was the flow before the tripping tape, which had an effect on the drag. The flow before the tripping tape was laminar in the experimental tests and this flow is modelled as turbulent in the CFD calculations. This was also a reason for the over prediction of the drag in the CFD calculations. However, the error could be roughly estimated by calculating the frictional resistance for turbulent respectively laminar flow, over the area before the tripping tape. The frictional resistance could be calculated from the drag formula (equation (2.6)) and replacing C_D with the total skin friction C_F. The total skin friction for the turbulent flow was obtained from the integral of equation (2.52), according to reference [7].

$$C_{F\_turbulent} = \frac{0.074}{\sqrt[5]{R_n}} \tag{5.1}$$

The total skin friction for the laminar flow can be obtained with equation (5.2), according to reference [8].

$$C_{F\_laminar} = \frac{1.328}{\sqrt{R_n}} \tag{5.2}$$

The frictional resistance for the turbulent flow at the area before the tape is 1.128N and the resistance for the laminar flow is 0.465N. This would mean that the modelled drag in the CFD calculations is approximately 0.66N too large. This corresponds very well with the overprediction seen in E_{drag} above (0.71N). If this correction had been introduced E_{drag} would be very small, much less than U_{val_drag} , so the drag prediction would have been validates as well. [1]

One geometric difference between the wind tunnel model and the model used in the numerical calculations was that the model in the numerical calculations had a sharp trailing edge while the wind tunnel model had to be cut off for manufacturing reasons. Hence the CFD model had a larger lateral area and that was probably one reason for the larger lift force in the numerical calculations.

6. Summary

An integrated bulb-keel has been shape optimised in this thesis using advanced numerical methods and the methods used have been evaluated and the numerical results have been validated with wind tunnel tests.

Two methods were used for the uncertainty analysis and the Least Square Root method was finally chosen to use over the Factor of Safety method. It was shown that the difference in the results between using 3 and 4 grids in the uncertainty analysis was significant and therefore the LSR-method was chosen. The estimated uncertainty was approximately 2.3% for the drag force and 12% for the lift force.

The method of using the rudder module in SHIPFLOW together with the exported section files was shown to be very effective in the shape variation of the keel. It was easy to vary the shape and the CFD setup could be kept almost untouched in the optimisation due to the section files.

It was noticed that the NSGA-II is a sufficient optimisation algorithm for a optimisation problem in a large design space, however the side limitations and constraints had to be adjusted and set very carefully. The penalty of 0.1, given to all variants that were violating the constraints, for the C_D/C_L-ratio probably did have a negative effect on the algorithm.

The optimised keel design was a bit longer and it had more round shape, however the most important shape variation was the narrow but sharp tip on the bulb. This tip seems to improve the design and prevent the overflow.

The keels were mounted on a 40 foot sailing yacht and tested in a velocity prediction program on an Olympic sailing course. The optimised keel was better in all wind directions but the differences were quite small. The optimised keel will however give an advantage, which could be important for a performance cruiser.

The wind tunnel test, which is a crucial part of a project when investigating new type of flow problems, was corresponding very well with the numerical results and C_L/C_D-ratio was especially well predicted in the numerical simulations. The C_L/C_D-ratio is an important performance indicator for a keel because it is important to know the drag for a given lift at the design stage of sailing yacht.

Throughout the project it has been noticed that the computational time is one significant limitation when carrying out CFD calculations. Therefore the setup has to be very carefully configured and the time allocated for the calculations is often under estimated at the planning stage of the project.

7. Future work

Some new ideas for investigation have evoked during the project and the author's recommendation for future study will follow below:

The optimisation was limited to the bulb part of the keel in this thesis and the fin part was kept constant. A global optimisation would be very interesting including both parts of the keel and mounting the keel on a hull would give an even better picture of the global performance.

Heel angles were not taken into account in thesis, thus all the calculations were performed at a heel angle of zero degrees. An optimisation including many heel angles would require a lot of computational time, hence that might not be a feasible solution, but investigate already designed integrated bulb-keels would give added value to this investigation and the effects of heel angle on the lift and drag could be gained. Investigating how the keels perform at more angles of attack would also give a better picture of the overall performance.

This thesis has shown that the tip of the bulb should square although the bulb itself has a rather round section shape. This was a very interesting outcome of the thesis and it shows that the same rules may apply for a bulb as for a fin keel stated in reference [3]. However this has to be investigated more deeply and more systematic tests have to be carried out with very dense grids in the area of the tip. Some other very important relations that are known for fin keels remain unknown for bulb keels, for instance how the bulb affects the aspect ratio, taper ratio and the sweep angle.

One improvement of the optimisation setup would be to include a velocity prediction program in the optimisation. By doing this, the overall performance would be taken into account more accurately. The hydrodynamic performance (CFD calculations) and the stability performance (VPP) would be considered and not only take the moment and weight as constraints as has been done in this thesis.

The optimisation of the 2 other bulbs, that were compared in reference [2; 6], would be very interesting to do and see how the new optimised keels are performing in relation to each other. However the setup used in this thesis with the section files and the rudder module could be difficult to configure due to the shape of the other bulbs. It could be difficult to model the sharp intersection between the fin part and the bulb part of the keel, because the rudder module is using section files for the build-up of the grid.

References

1. **Bergman, E., Pettersson, W., Tell, J. & Tesanovic, A.** *Investigation of keel bulbs for sailing yachts* . BSc thesis, Department of Shipping and Marine Technology. Gothenburg, Sweden : Chalmers Technical University, 2010.
2. **Axfors, B. Tunander, H.** *Investigation of Keel Bulbs for Sailing Yachts.* MSc thesis, Department of Shipping and Marine Technology. Gothenburg : Chalmers University of Technology, 2011.
3. **Larsson, L. & Eliasson, R.** *Principles of Yacht Design, third edition.* Maine : International Marine/McGraw-Hill, 2007. ISBN-13:9780071487696.
4. **Rossell, H. E, Chapman, L. B.** *Principle of Naval Architecture.* New York : The Society of Naval Architecture and Marine Engineers, 1949.
5. **Abbott, I. H., von Doenhoff, A. E.,.** *Theory of Wing Sections.* London : McGraw-Hill Book Company, 1949.
6. **Orych, Michał.** *Calculations of the flow and resistance components of systematically varied keel/bulb winglets.* MSc thesis, Department of Shipping and Marine Technology. Gothenburg : Chalmers University of Technology, 2005.
7. **Matusiak, J.** *KUL-24.113 Laskennallinen laivahydrodynamikka Osa 1.* : Helsinki University of Technology, 2007. .
8. **Larsson, L. & Raven, H. C.** *Ship Resistance and Flow.* : The Society of Naval Architects and Marine Engineers, 2010. ISBN 987-0-939773-76-3.
9. **FLOWTECH International AB.** *XCHAP Theoretical Manual.* s.l. : FLOWTECH International AB, 2007.
10. **G.B. Deng, P. Queutey, M. Visonneau.** Three-Dimensional Flow Computation with Reynold Stress and Algebraic Stress Models. [book auth.] W. Rodi. *Engineering Tubulence Modelling and Experiments 6.* s.l. : Elsevier Ltd., 2005.
11. **Regnström, B.** *Introduction to overlapping grids.* : FLOWTECH, 2008. .
12. **Roache, P.J.** *Verification and Validation in Computational Science and Engineering.* New Mexico : Hermosa Publisher, 1998. .
13. **Eça, L., Vaz, G., Hoekstra, M.** *Code Verification, Solution Verification and Validation in RANS Solvers.* Shanghai : ASME 29th International Conference on Ocean, Offshore and Arctic Engineering OMAE2010, 2010.
14. **Eça, L., Vaz, G., Hoekstra, M.** *A VERIFICATION AND VALIDATION EXERCISE FOR THE FLOW.* Lisbon, Portugal : V European Conference on Computational Fluid Dynamics, June 2010.
15. **Xing, T. & Stern, F.** *Factor of Safety for Richardson Extrapolation.* s.l. : Journal of Fluids Engineering, 2010.
16. **Eça, L., Hoekstra, M.** *Discretization Uncertainty Estimation based on a Least Squares.* Lisbon : 2nd Workshop on CFD Uncertainty Analysis, October 2006.
17. **N., Vaanderplaast G.** *Numerical Optimization Techniques for Engineering Design. 3rd Edition.* : Vaanderplaast Research & Development Inc., 2001. ISBN 0-944956-01-7.
18. **Abraham, A., Nedjah, N. & de Macedo Mourelle, L.** *Evolutionary Computation: from Genetic Algorithms to Genetic Programming.* s.l. : Studies in Computational Intelligence, 2006. ISBN 978-3-540-29849-6.
19. **Cirello, A., Mancuso.** *A numerical approach to the keel design of a sailing yacht.* s.l. : Ocean Engineering Elsevier Ltd, 2008.

20. **Srinivas, N., Deb, K.** *Multiobjective Optimization Using Nondominated Sorting in Genetic Algorithm.* s.l. : Journal of Evolutionary Computations, 1994.
21. **Deb, K., Pratap, A., Agarwal, S., Meyarivan, T.** *A Fast and Elitist Multiobjective Genetic Algorithm: NSGA-II.* Kanpur : Indian Institute of Technology Kanpur, 2002.
22. **Barlow, J. B., William, H. R. Jr, Pope, A.** *Low-Speed Wind Tunnel Testing, Third Edition.* s.l. : Wiley-Interscience publication, 1999. ISBN-0-471-55774-9.
23. **Werner, S.** *Computational Hydrodynamics Applied to an America's Cup Class Keel.* Gothenburg, Sweden : Chalmers University of Technology, 2006. ISBN 91-7291-849-7.
24. **RUAG aerospace defence technology.** *DNW: DMS–Waage 196–6H Kalibrierbericht zur Version C02.* s.l. : RUAG, 2004.
25. **Ranzenbach, R., Zahn, M.** *Experimental Methods to Evaluate Underwater Appendages.* Maryland : The 17th Chesapeake Sailing Yacht Symposium, 2005.
26. **Maskell, E., C.** *A Theory of the Blockage Effects on Bluff Bodies and Stalled Wings in a Closed Wind Tunnel"* . s.l. : Aeronautical Research Council R&M No 3400, 1963.

APPENDIX 1

Appendix to section 4.1.2.

The curve fittings to the results using equation (2.61)

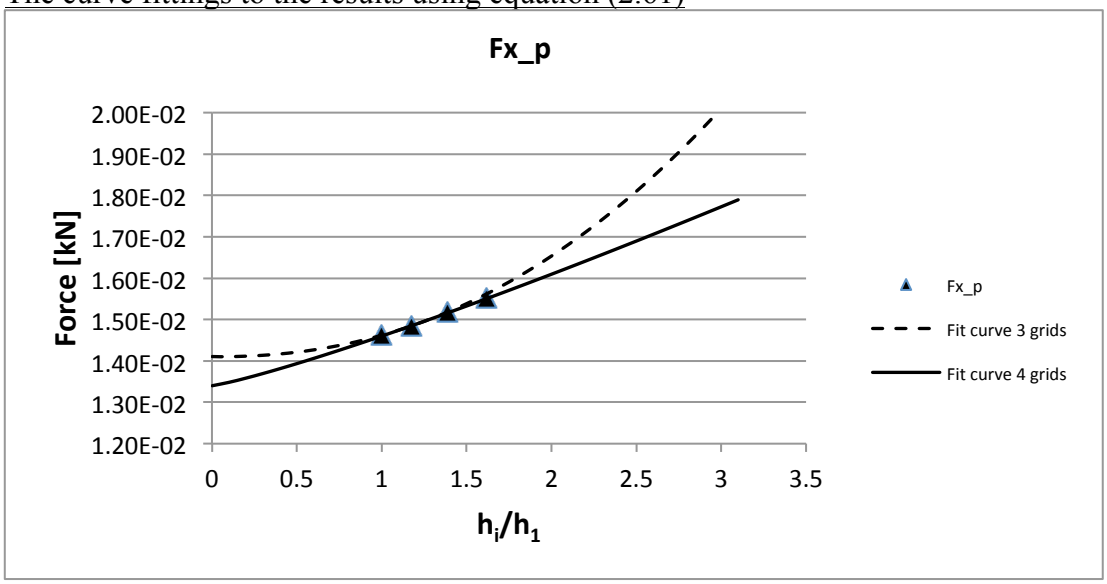

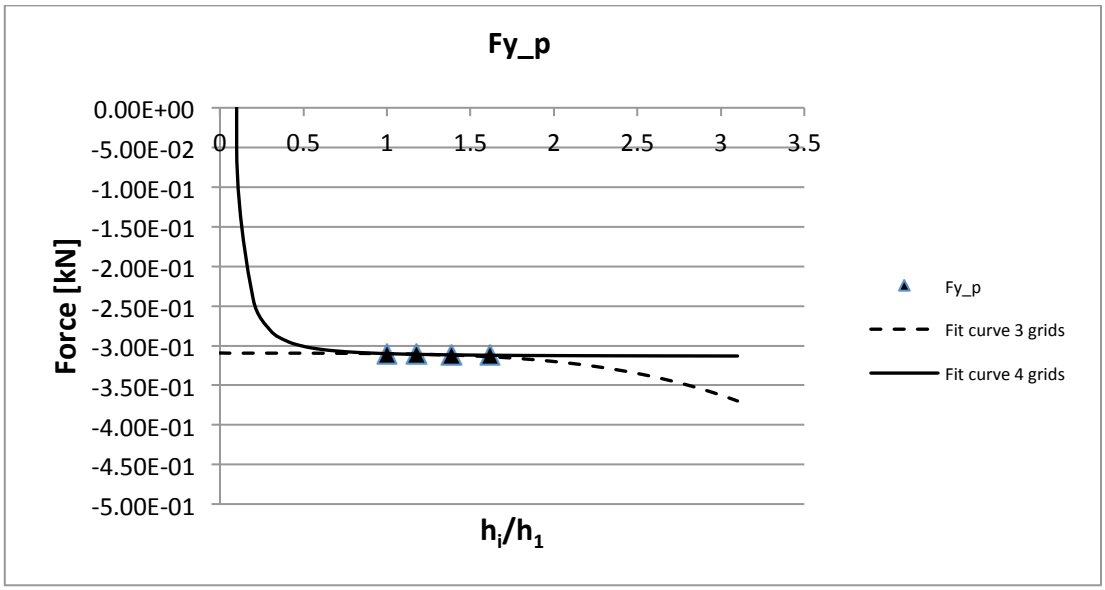

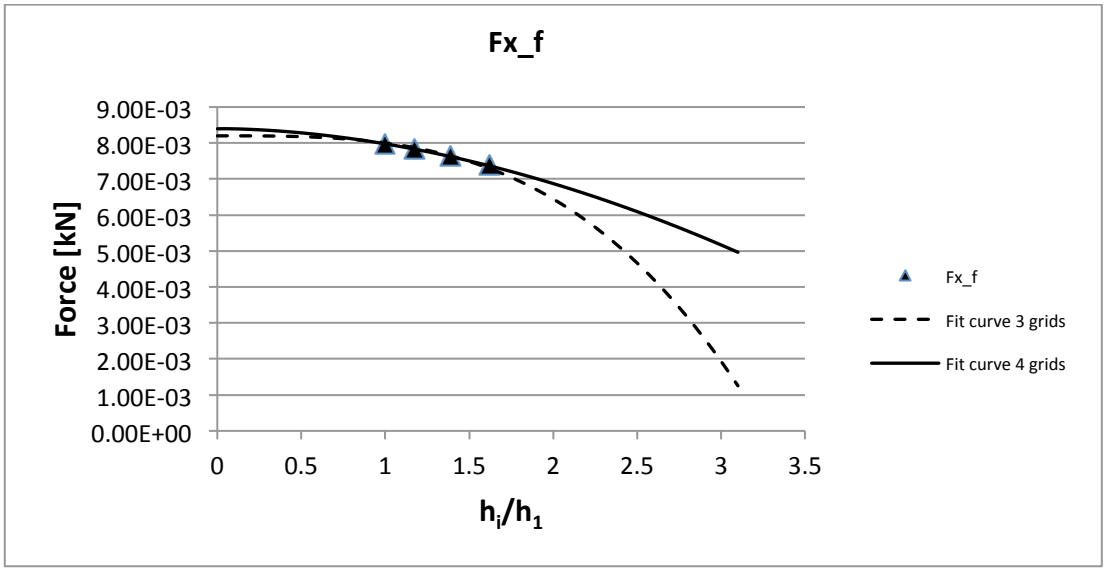
Fx_f
9.00E-03
8.00E-03
7.00E-03
6.00E-03
5.00E-03
4.00E-03
3.00E-03
2.00E-03
1.00E-03
0.00E+00
Force [kN]
0
0.5
1
1.5
2
2.5
3
3.5
h_i/h_1
Fx_f
Fit curve 3 grids
Fit curve 4 grids

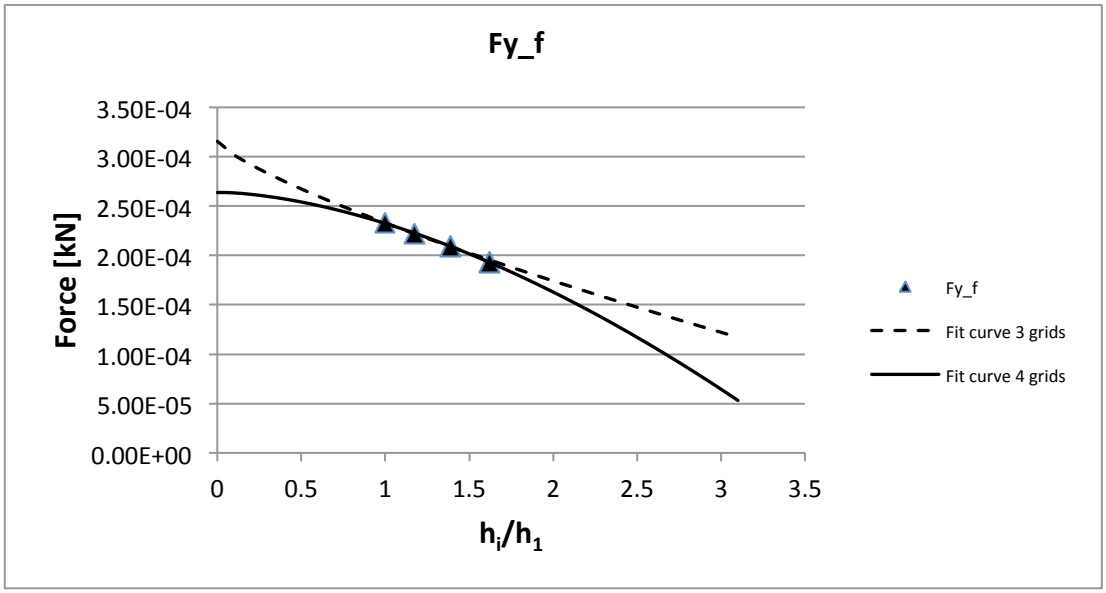
Fy_f
3.50E-04
3.00E-04
2.50E-04
2.00E-04
1.50E-04
1.00E-04
5.00E-05
0.00E+00
Force [kN]
0
0.5
1
1.5
2
2.5
3
3.5
h_i/h_1
Fy_f
Fit curve 3 grids
Fit curve 4 grids

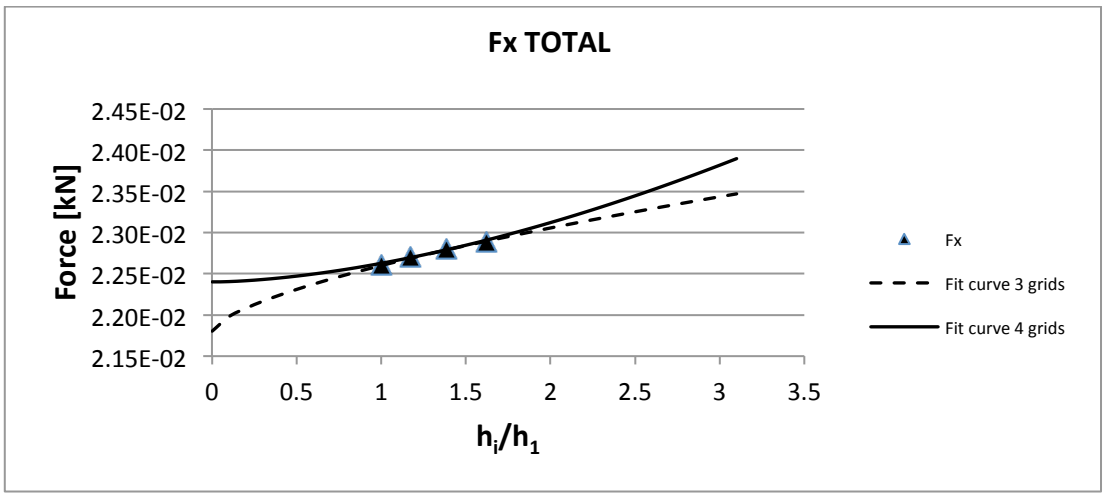
Fx TOTAL
2.45E-02
2.40E-02
2.35E-02
2.30E-02
2.25E-02
2.20E-02
2.15E-02
Force [kN]
0
0.5
1
1.5
2
2.5
3
3.5
h_i/h_1
Fx
Fit curve 3 grids
Fit curve 4 grids

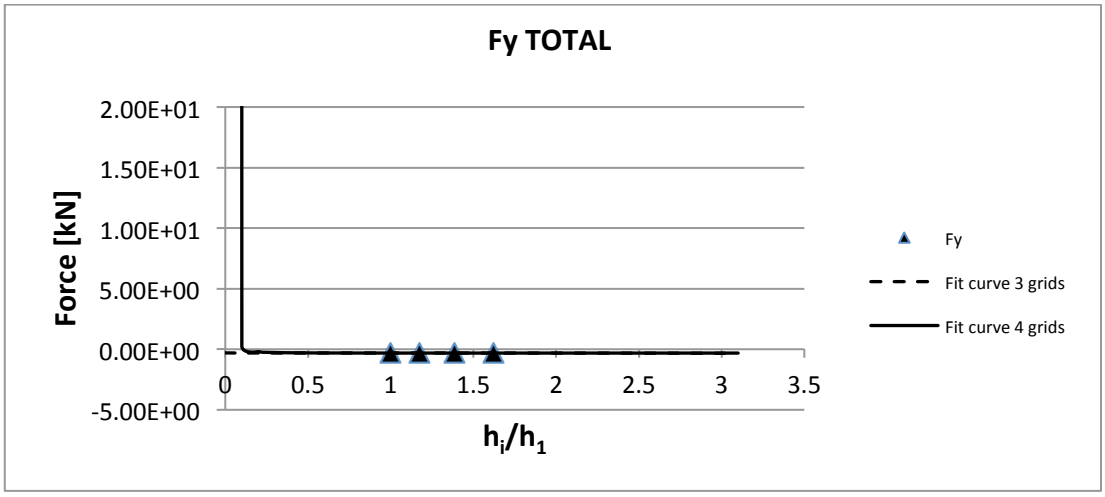

The curve fittings to the results using equation (2.68)

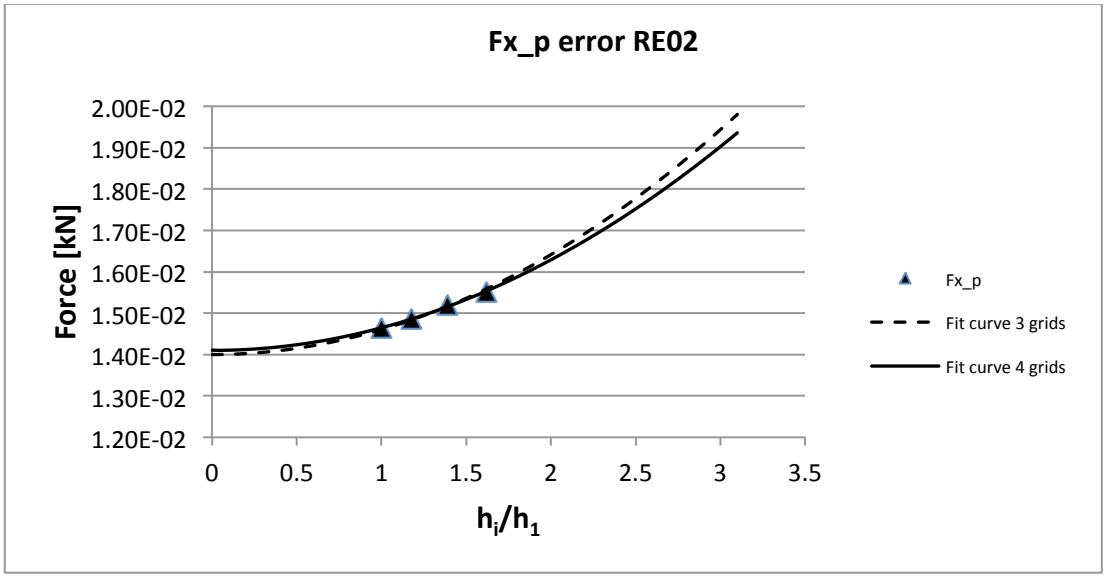

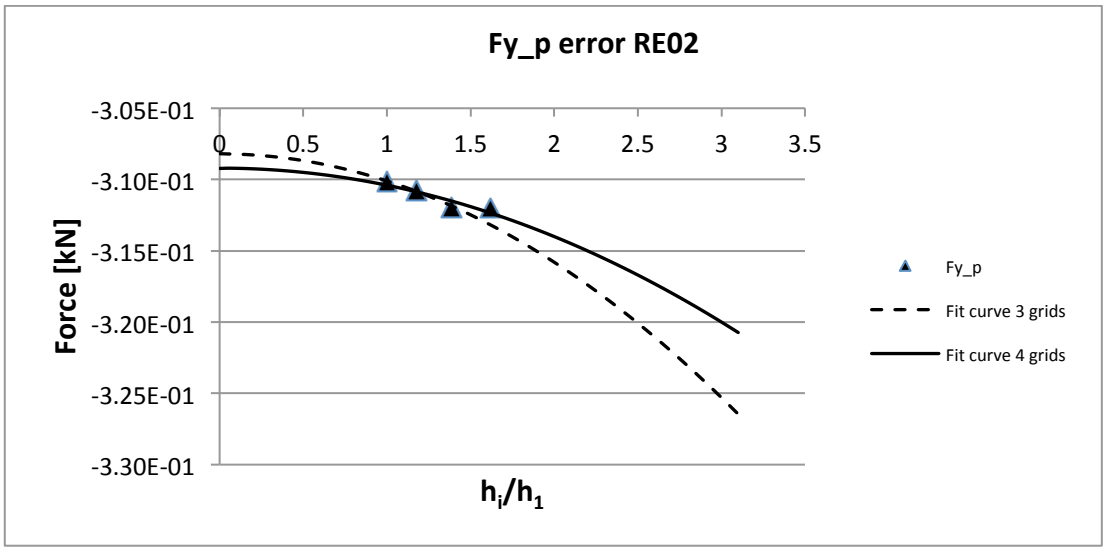

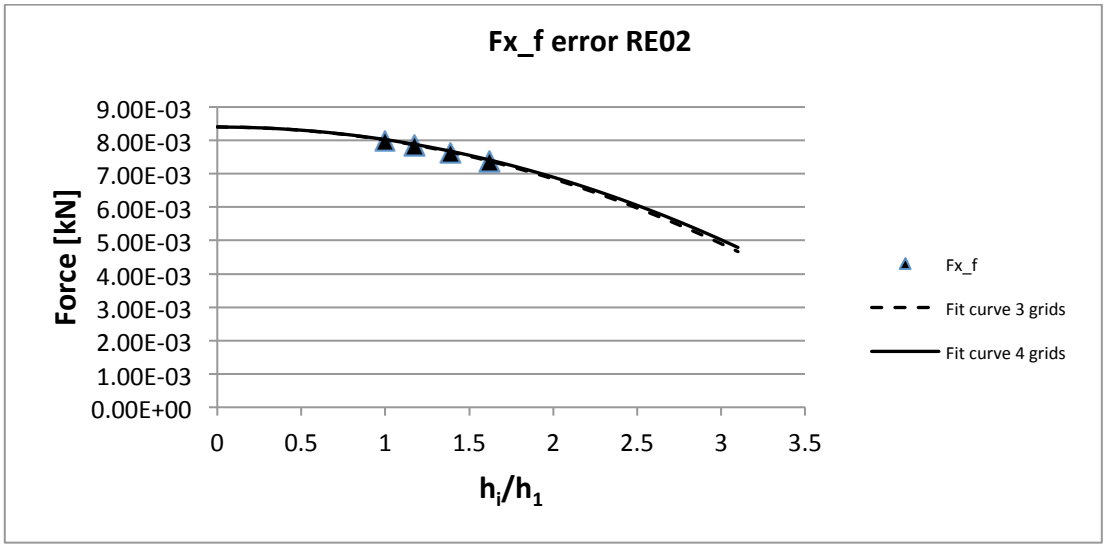
Fx_f error RE02
9.00E-03
8.00E-03
7.00E-03
6.00E-03
5.00E-03
4.00E-03
3.00E-03
2.00E-03
1.00E-03
0.00E+00
Force [kN]
0
0.5
1
1.5
2
2.5
3
3.5
h_i/h_1
Fx_f
Fit curve 3 grids
Fit curve 4 grids

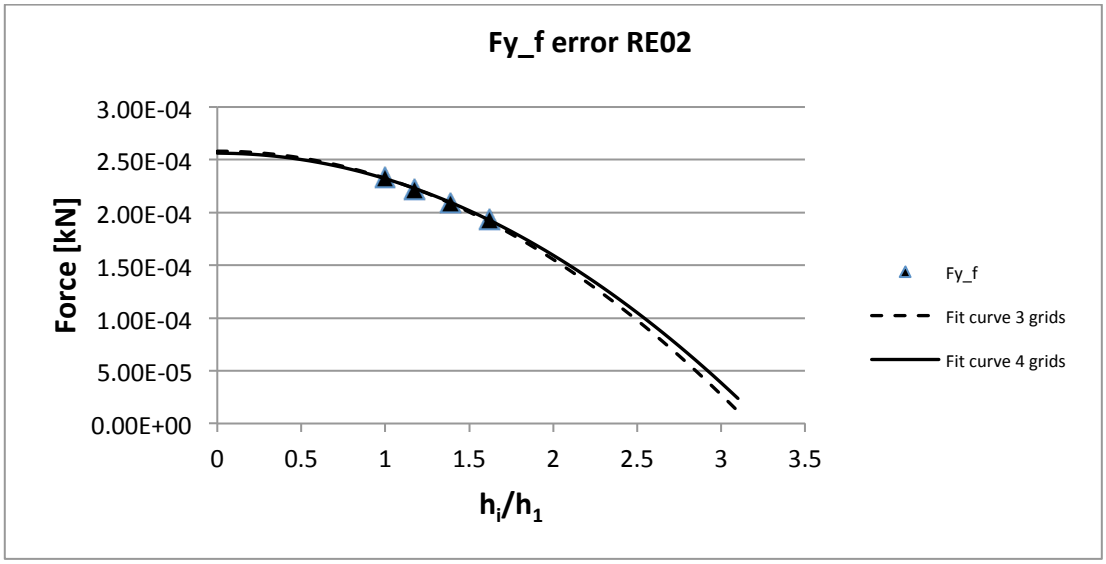
Fy_f error RE02
3.00E-04
2.50E-04
2.00E-04
1.50E-04
1.00E-04
5.00E-05
0.00E+00
Force [kN]
0
0.5
1
1.5
2
2.5
3
3.5
h_i/h_1
Fy_f
Fit curve 3 grids
Fit curve 4 grids

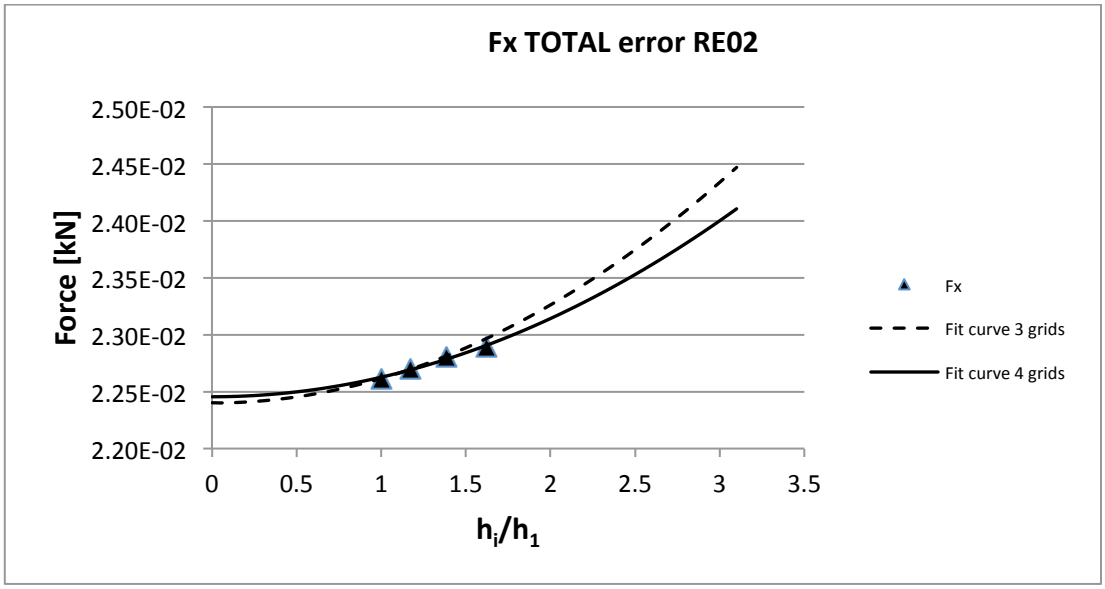
Fx TOTAL error RE02
2.50E-02
2.45E-02
2.40E-02
2.35E-02
2.30E-02
2.25E-02
2.20E-02
Force [kN]
0
0.5
1
1.5
2
2.5
3
3.5
h_i/h_1
Fx
Fit curve 3 grids
Fit curve 4 grids

..

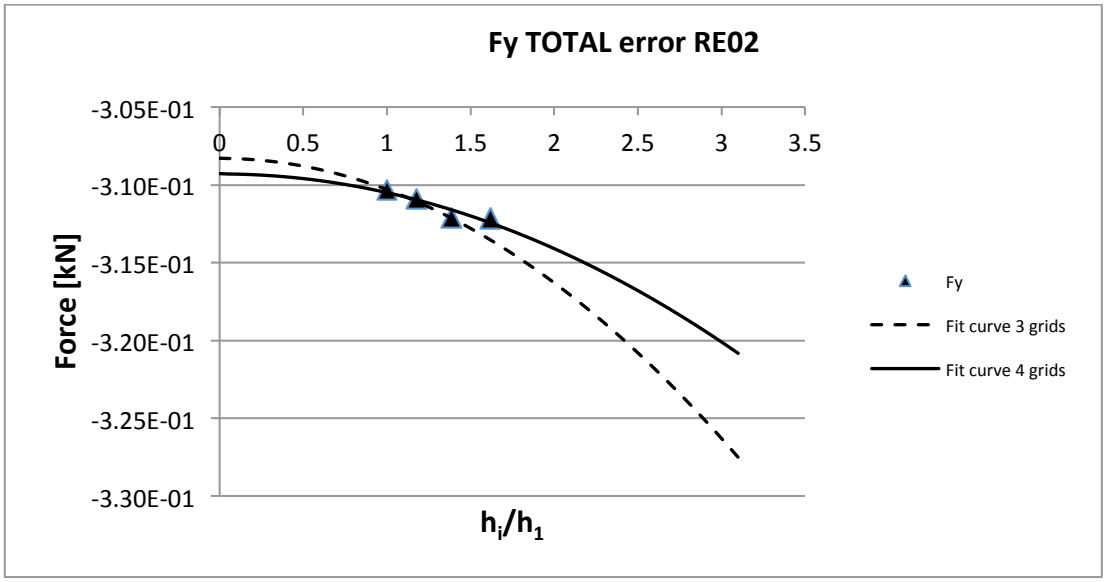

The curve fittings to the results using equation (2.69)

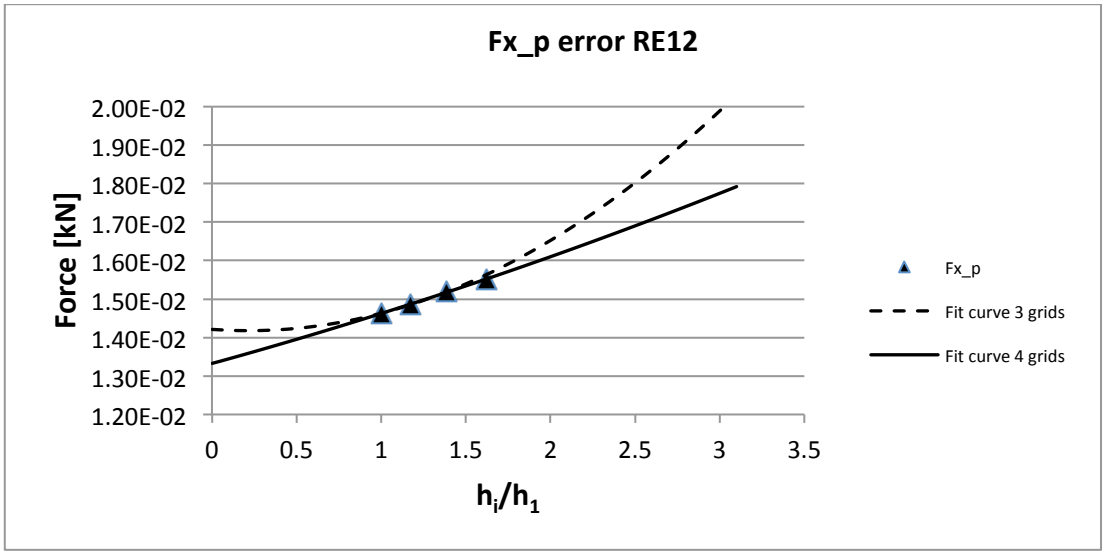

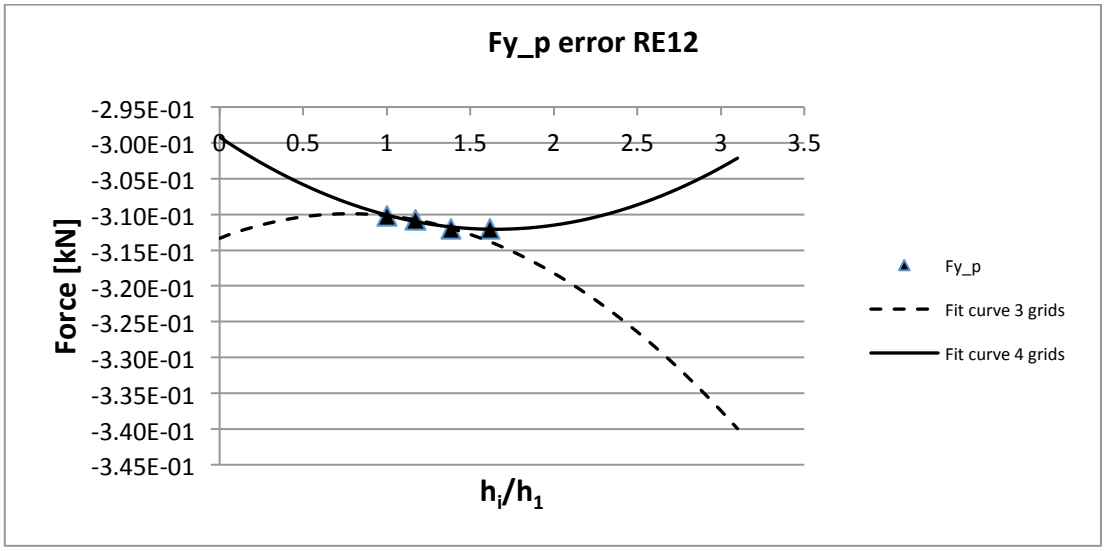
Fy_p error RE12
-2.95E-01
-3.00E-01
-3.05E-01
-3.10E-01
-3.15E-01
-3.20E-01
-3.25E-01
-3.30E-01
-3.35E-01
-3.40E-01
-3.45E-01
Force [kN]
0
0.5
1
1.5
2
2.5
3
3.5
h_i/h_1
Fy_p
Fit curve 3 grids
Fit curve 4 grids

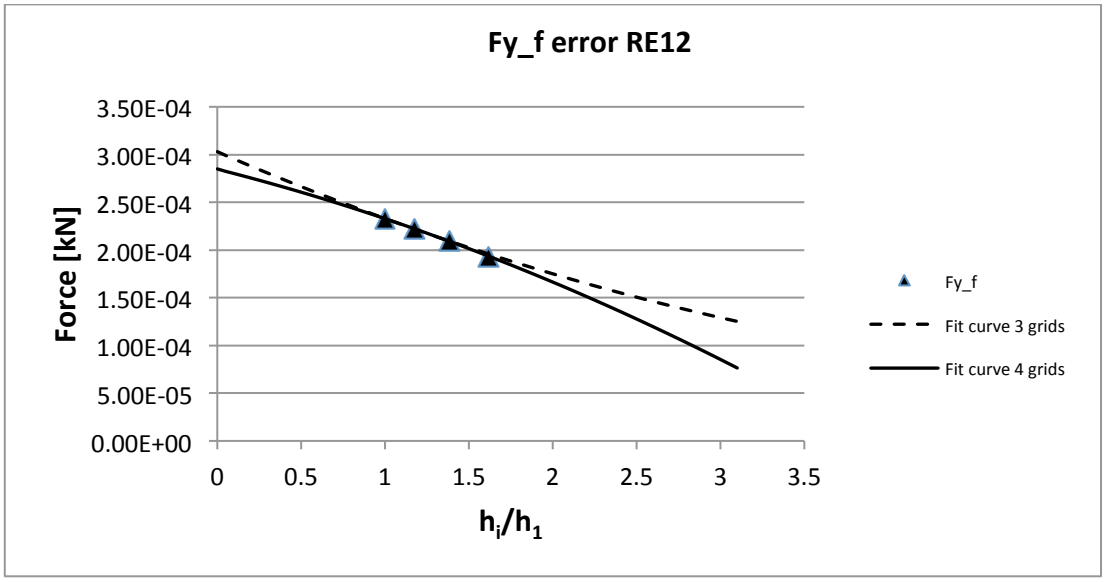
Fy_f error RE12
3.50E-04
3.00E-04
2.50E-04
2.00E-04
1.50E-04
1.00E-04
5.00E-05
0.00E+00
Force [kN]
0
0.5
1
1.5
2
2.5
3
3.5
h_i/h_1
Fy_f
Fit curve 3 grids
Fit curve 4 grids

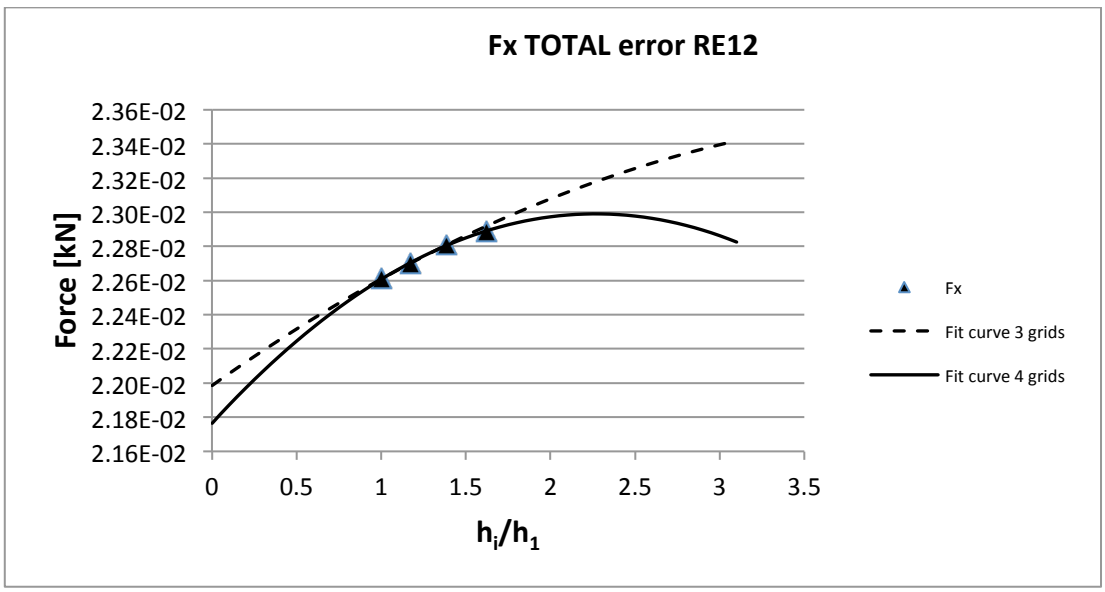
Fx TOTAL error RE12
2.36E-02
2.34E-02
2.32E-02
2.30E-02
2.28E-02
2.26E-02
2.24E-02
2.22E-02
2.20E-02
2.18E-02
2.16E-02
Force [kN]
0
0.5
1
1.5
2
2.5
3
3.5
h_i/h_1
Fx
Fit curve 3 grids
Fit curve 4 grids

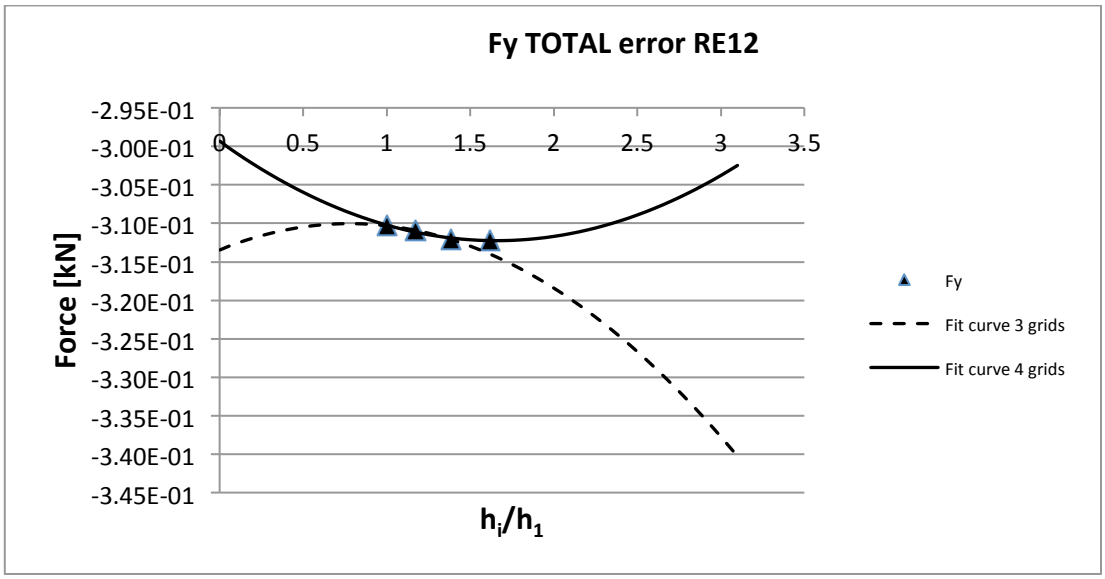
Fy TOTAL error RE12
-2.95E-01
-3.00E-01
-3.05E-01
-3.10E-01
-3.15E-01
-3.20E-01
-3.25E-01
-3.30E-01
-3.35E-01
-3.40E-01
-3.45E-01
Force [kN]
0
0.5
1
1.5
2
2.5
3
3.5
h_i/h_1
Fy
Fit curve 3 grids
Fit curve 4 grids

APPENDIX 2

The command file used in the Shipflow calculations.

```
xflo
  titl(titl="K2 , heel=0, ang=4")
  prog(xcha)
  vshi(fn=[0],rn=[3.46e06])
  symm(nosy)
  stre(id="middlex",midd,s0=0.35,s1=0.65,ds0=0.4)
  stre(id="middley",midd,s0=0.35,s1=0.65,ds0=0.4)
  stre(id="middlez",midd)
  box(id="box",low=[-10, -10, -10],high=[10, 10, 0],dime=[71, 71,
71],str1="middlex",str2="middley",str3="middlez",bc11="INFLOW",bc12=
"OUTFLOW",bc21="SLIP",bc22="SLIP",bc31="SLIP",bc32="SLIP")
  rudd(id="keel2",ytar=0.8485,span=1.86,tp1o,tp2f,s=[0, 0.0692951,
0.13859, 0.207885, 0.27718, 0.346476, 0.415771, 0.485066, 0.554361,
0.623656, 0.631335, 0.639015, 0.646694, 0.654373, 0.662053,
0.669732, 0.677412, 0.685091, 0.69277, 0.70045, 0.708129, 0.715809,
0.723488, 0.731167, 0.738847, 0.746526, 0.754206, 0.761885,
0.769564, 0.777244, 0.784923, 0.792603, 0.800282, 0.807961,
0.815641, 0.82332, 0.831, 0.838679, 0.846358, 0.854038, 0.861717,
0.869397, 0.877076, 0.884755, 0.892435, 0.900114, 0.907794,
0.915473, 0.923152, 0.930832, 0.938511, 0.94619, 0.95387, 0.961549,
0.969229, 0.976908, 0.984587, 0.992267, 1],c=[1.08, 1.06753,
1.05505, 1.04258, 1.03011, 1.01763, 1.00516, 0.992688, 0.980215,
0.967742, 0.96636, 0.964977, 0.963812, 0.969529, 0.98441, 1.0073,
1.03718, 1.07312, 1.11429, 1.1599, 1.2092, 1.2615, 1.31613, 1.3724,
1.42968, 1.48477, 1.53009, 1.56859, 1.60226, 1.63219, 1.65903,
1.6832, 1.705, 1.72465, 1.74229, 1.75803, 1.77195, 1.7841, 1.79451,
1.80321, 1.81019, 1.81544, 1.81893, 1.82064, 1.82051, 1.81885,
1.81607, 1.81215, 1.8071, 1.80087, 1.79341, 1.78462, 1.77437,
1.76244, 1.74847, 1.73186, 1.71143, 1.68414, 1.62089],xle=[0, -
0.00978707, -0.0195741, -0.0293612, -0.0391483, -0.0489353, -
0.0587224, -0.0685095, -0.0782966, -0.0880836, -0.0891682, -
0.0902529, -0.0913375, -0.0924221, -0.0935067, -0.0945913, -
0.095676, -0.0967606, -0.0978452, -0.0989298, -0.100014, -0.101099,
-0.102184, -0.103268, -0.104353, -0.105438, -0.106522, -0.107607, -
0.108691, -0.109776, -0.110861, -0.111945, -0.11303, -0.114114, -
0.115199, -0.116284, -0.117368, -0.118453, -0.119538, -0.120622, -
0.121707, -0.122792, -0.123876, -0.124959, -0.126051, -0.127692, -
0.130484, -0.134398, -0.139455, -0.145684, -0.153145, -0.161929, -
0.172179, -0.184113, -0.198083, -0.214691, -0.235121, -0.262412, -
0.325659],dime=[121, 71, 93],sect=["58", "57", "56", "55", "54",
"53", "52", "51", "50", "49", "48", "47", "46", "45", "44", "43",
"42", "41", "40", "39", "38", "37", "36", "35", "34", "33", "32",
"31", "30", "29", "28", "27", "26", "25", "24", "23", "22", "21",
"20", "19", "18", "17", "16", "15", "14", "13", "12", "11", "10",
"09", "08", "07", "06", "05", "04", "03", "02", "01", "00"],angl=-
4,ysig=1,bc31="SLIP")
end
xcha
  para(nthr=8)
  cont(start,maxi=4500,impo)
end
```

APPENDIX 3

Velocity plots of the total velocities around the initial keel design taken at 10 cm intervals starting from the leading edge.

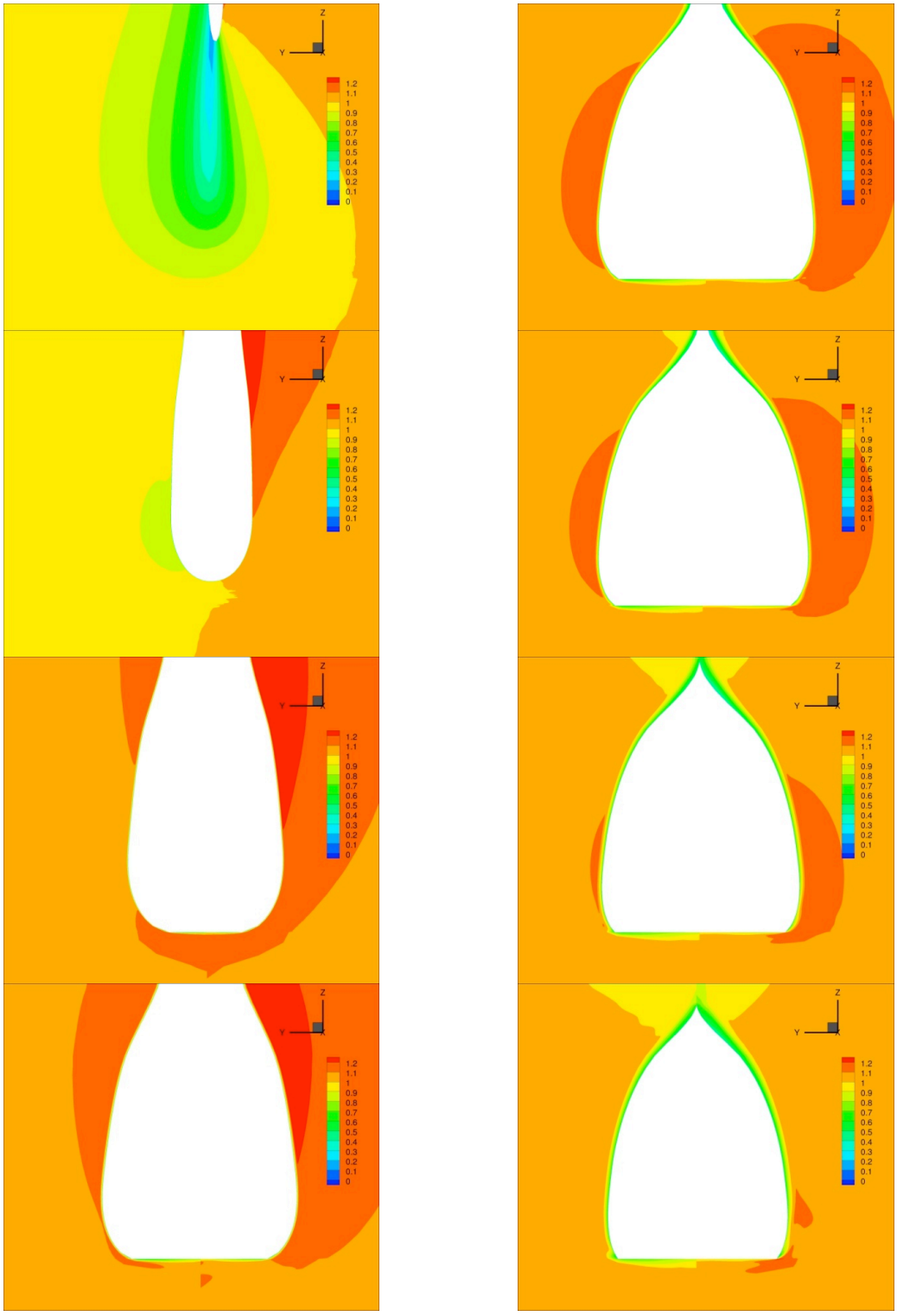

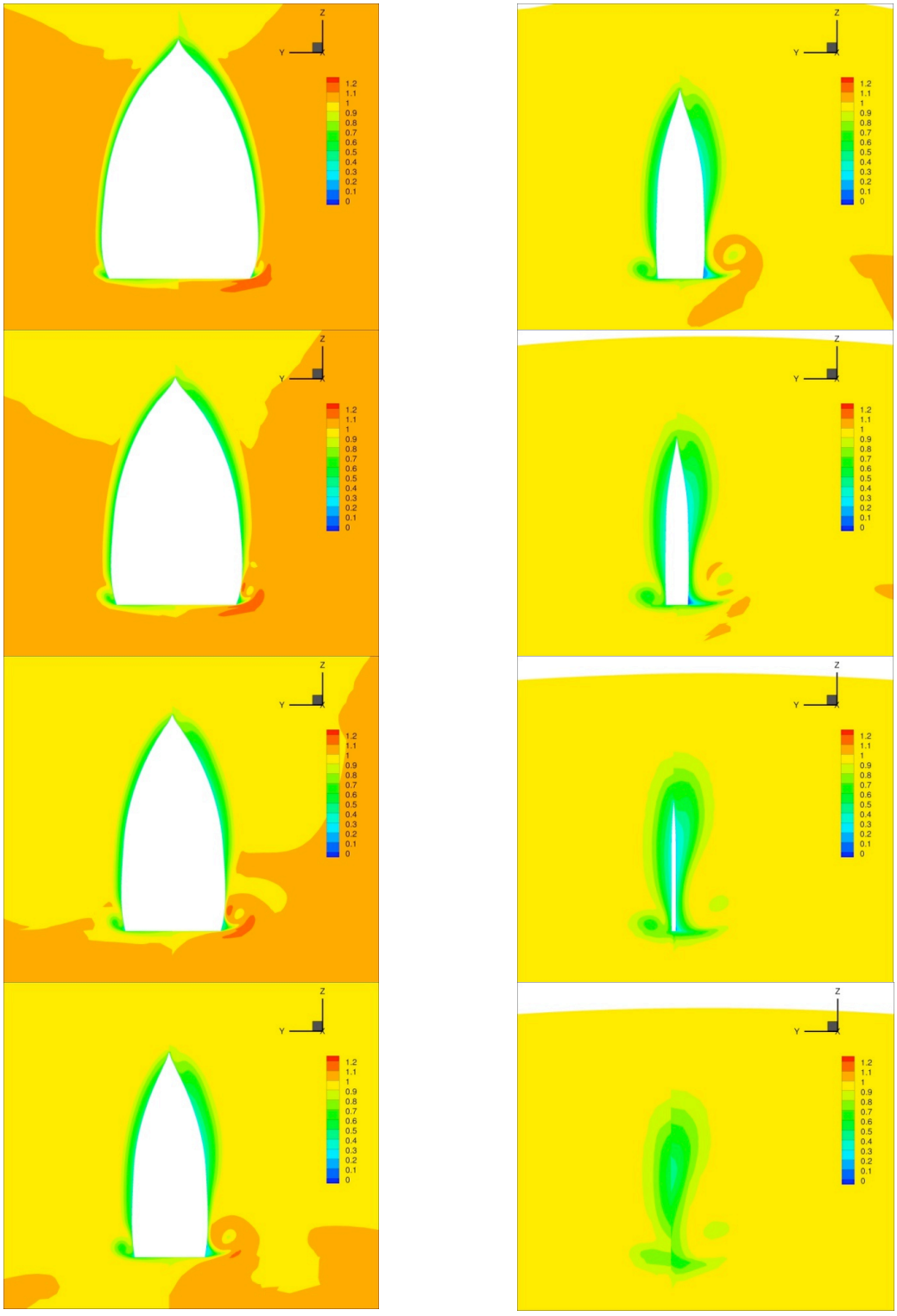
Z
Y
1.2
1.1
1
0.9
0.8
0.7
0.6
0.5
0.4
0.3
0.2
0.1
0

APPENDIX 4

Velocity plots of the total velocities around the optimised keel design taken at 10 cm intervals starting from the leading edge.

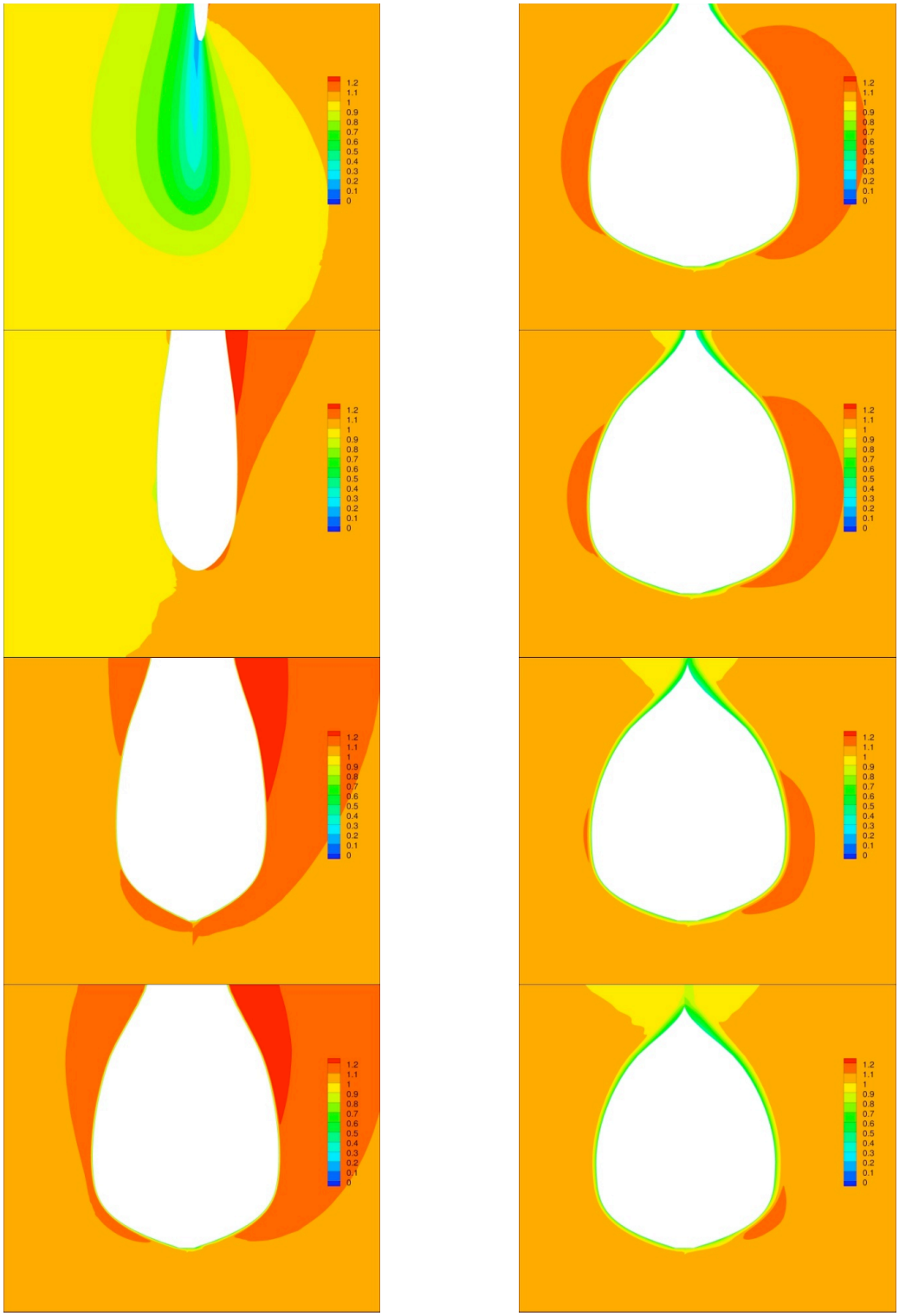

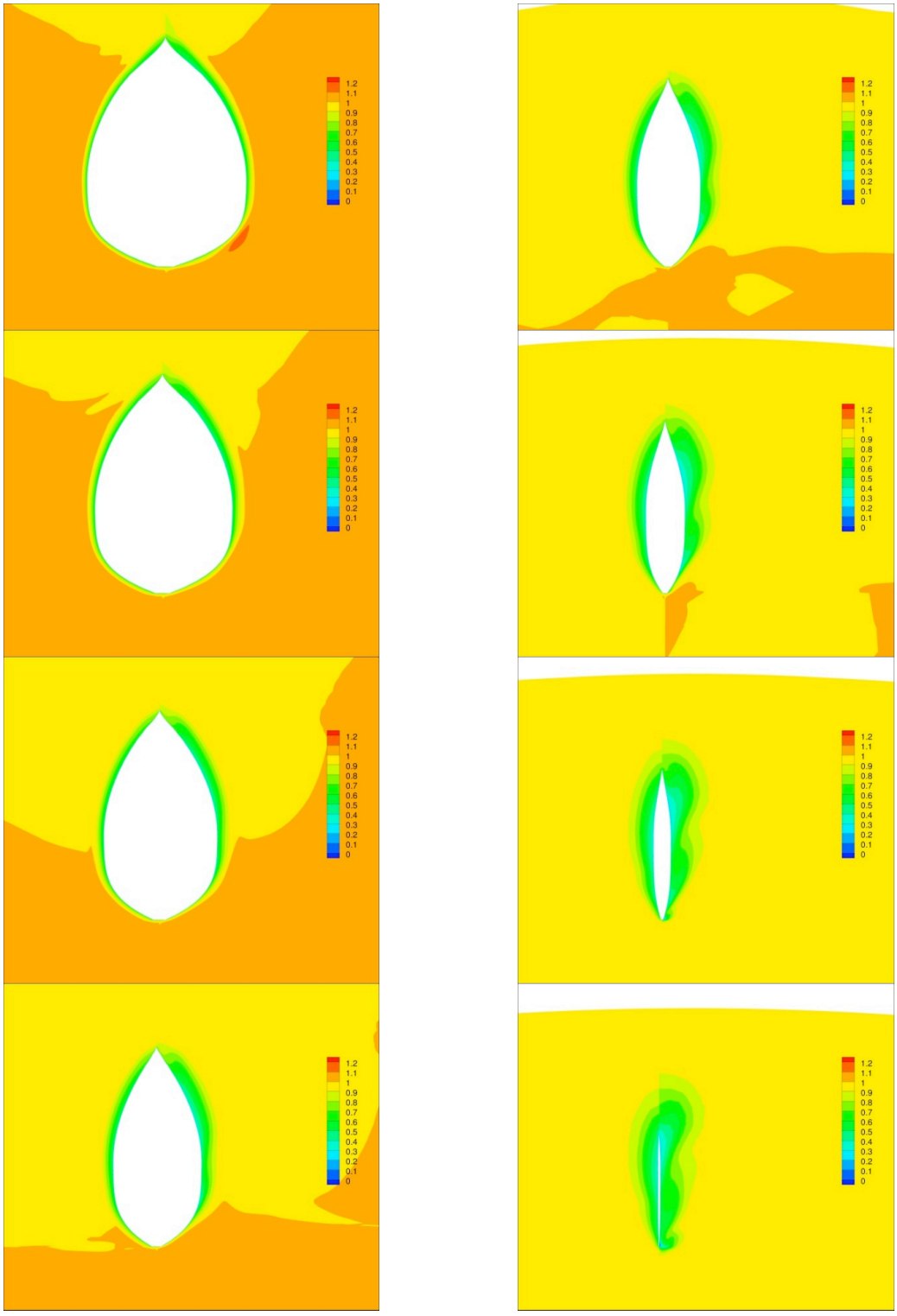
1.2
1.1
1
0.9
0.8
0.7
0.6
0.5
0.4
0.3
0.2
0.1
0

APPENDIX 5

The velocity plots of the initial design and the optimised design. The flow vectors are also plotted in white.

Initial design (u-velocities)

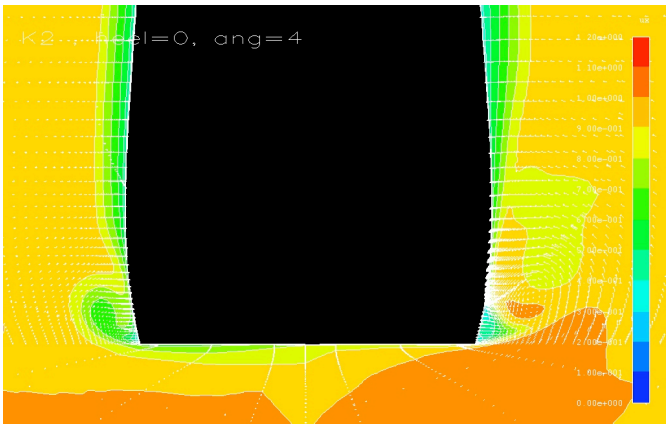

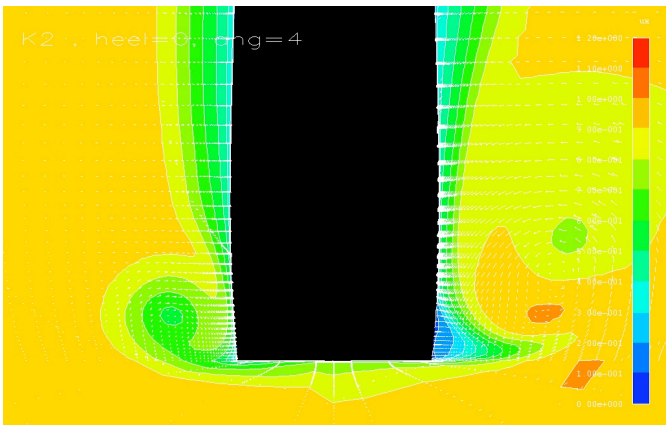

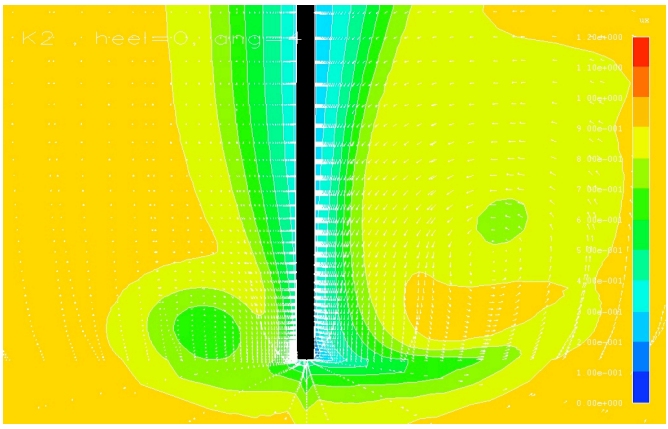

Optimised design (u-velocities)

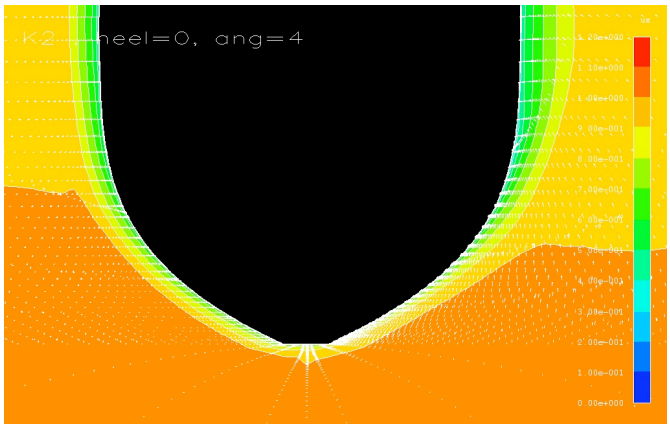

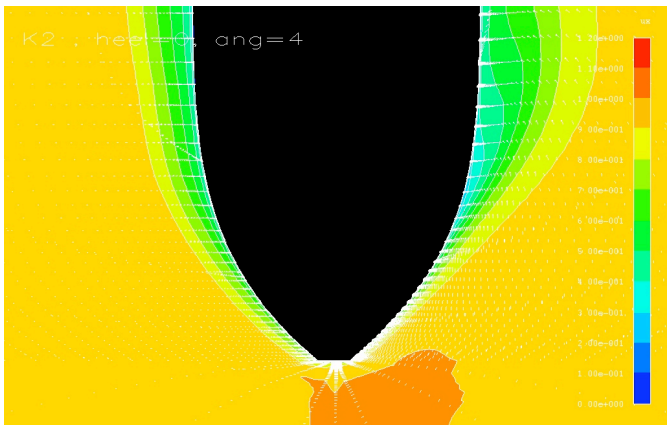

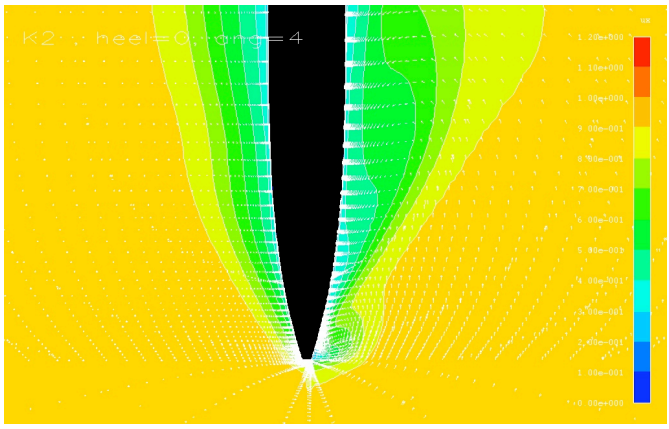

APPENDIX 6

The convergence plots of all different design variables together with the plots of the convergence of the weight and moment.

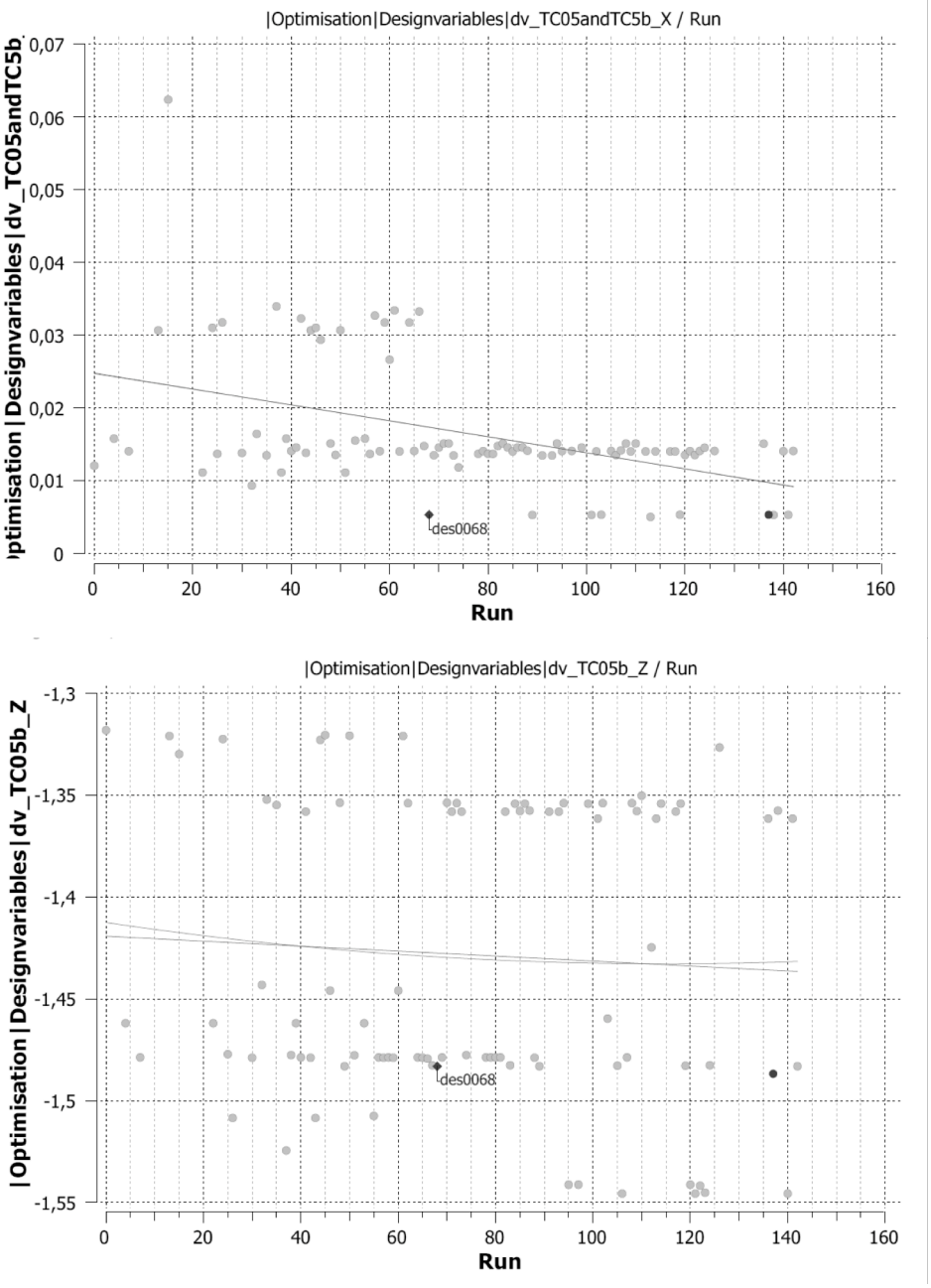

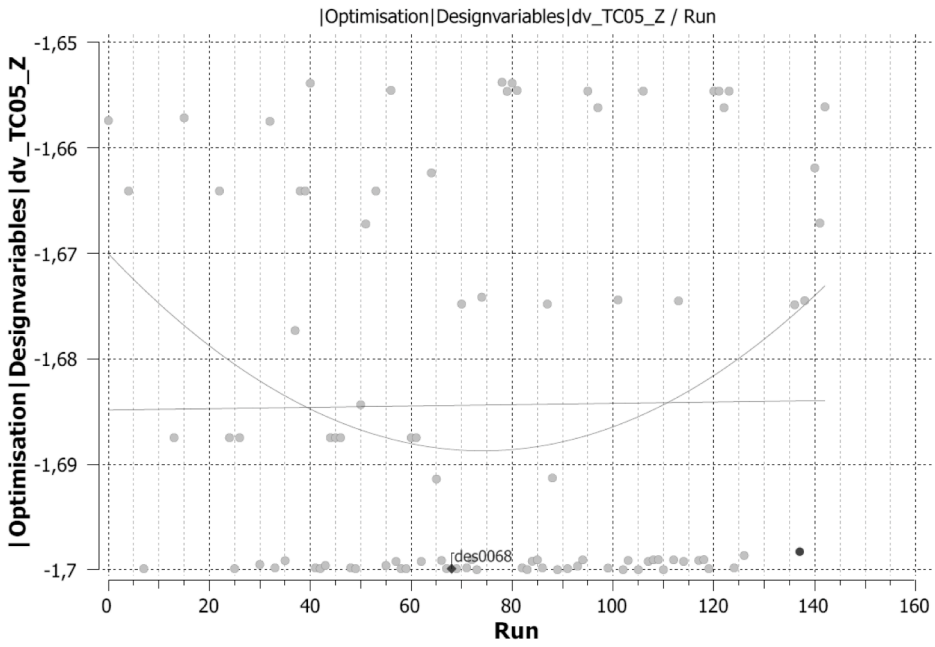
|Optimisation|Designvariables|dv_TC05_Z / Run
|Optimisation|Designvariables|dv_TC05_Z
-1,65
-1,66
-1,67
-1,68
-1,69
-1,7
des0068
0
20
40
60
80
100
120
140
160
Run

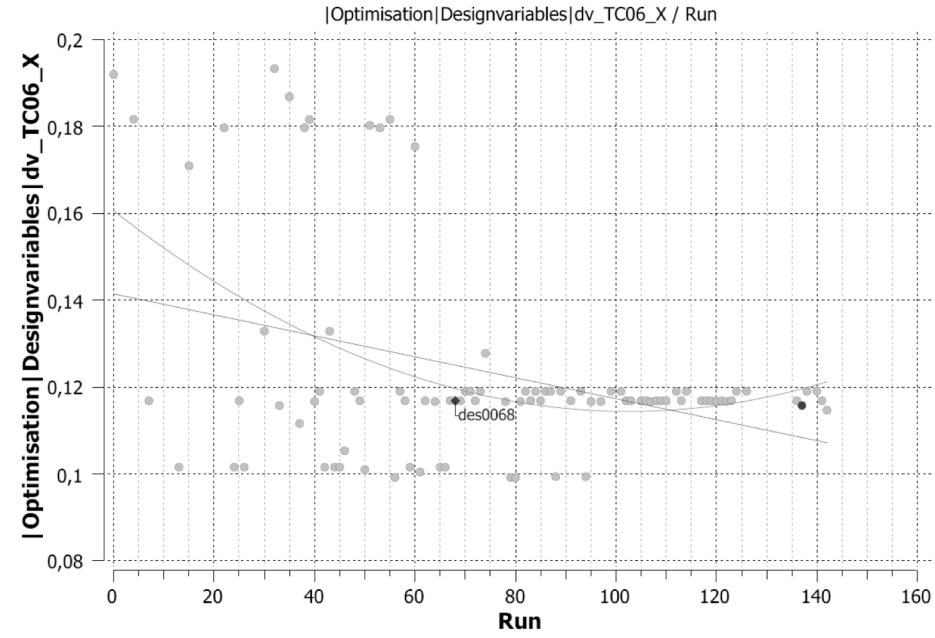
|Optimisation|Designvariables|dv_TC06_X / Run
|Optimisation|Designvariables|dv_TC06_X
0,2
0,18
0,16
0,14
0,12
0,1
0,08
des0068
0
20
40
60
80
100
120
140
160
Run

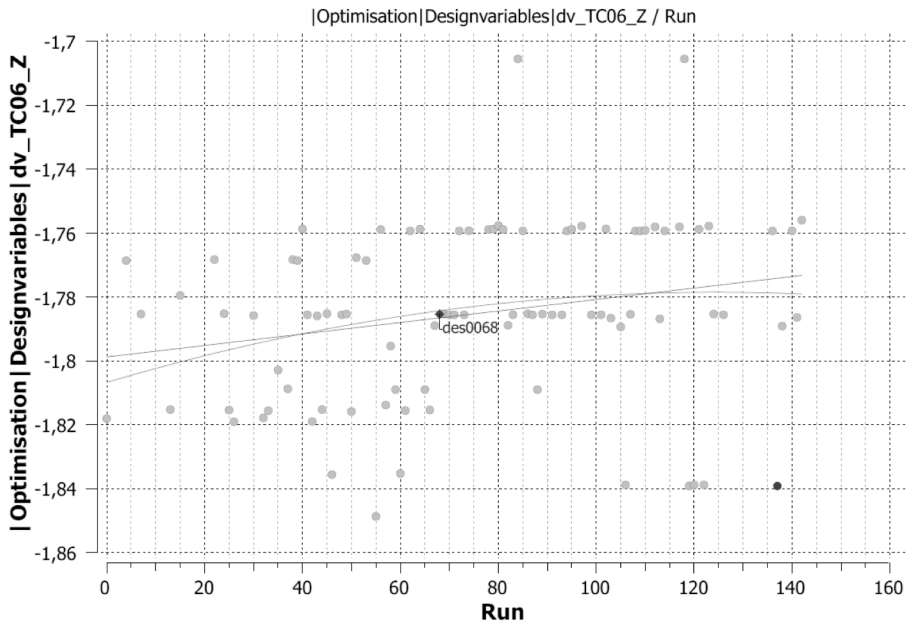
|Optimisation|Designvariables|dv_TC06_Z / Run
|Optimisation|Designvariables|dv_TC06_Z
-1,7
-1,72
-1,74
-1,76
-1,78
-1,8
-1,82
-1,84
-1,86
des0068
0
20
40
60
80
100
120
140
160
Run

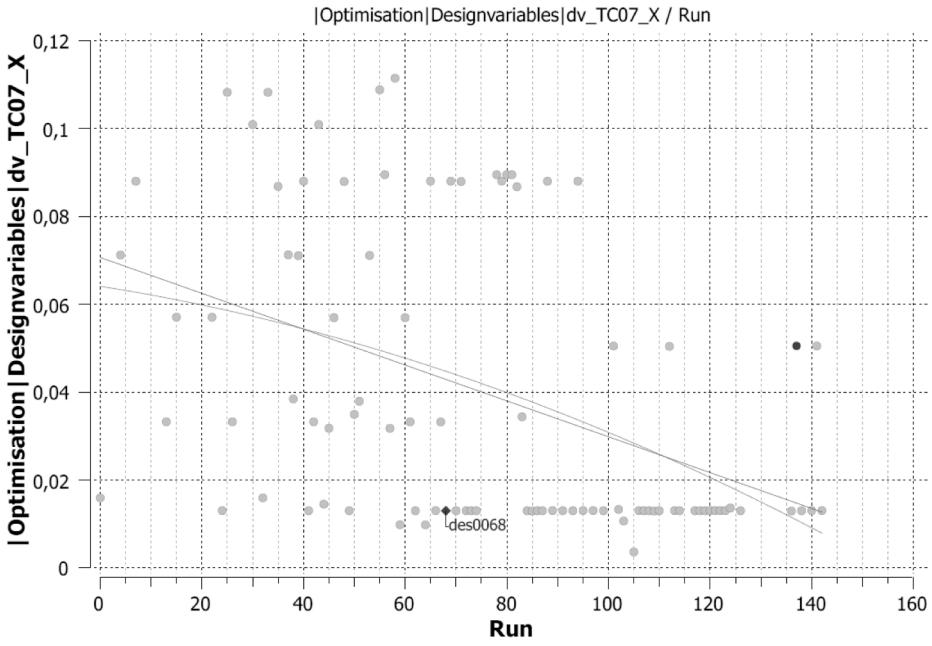
|Optimisation|Designvariables|dv_TC07_X / Run
|Optimisation|Designvariables|dv_TC07_X
0,12
0,1
0,08
0,06
0,04
0,02
0
des0068
0
20
40
60
80
100
120
140
160
Run

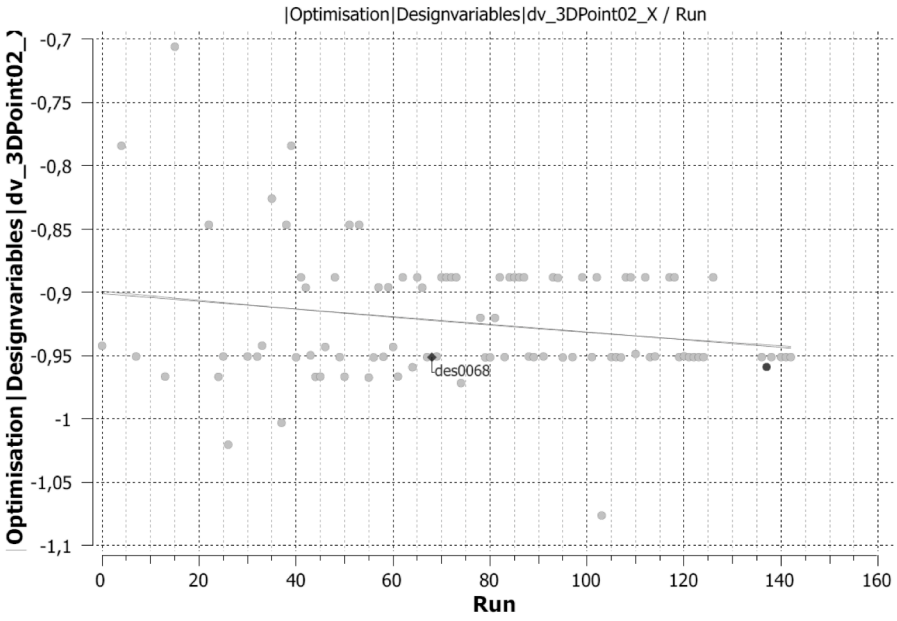
|Optimisation|Designvariables|dv_3DPoint02_X / Run
Optimisation|Designvariables|dv_3DPoint02_
-0,7
-0,75
-0,8
-0,85
-0,9
-0,95
-1
-1,05
-1,1
des0068
0
20
40
60
80
100
120
140
160
Run

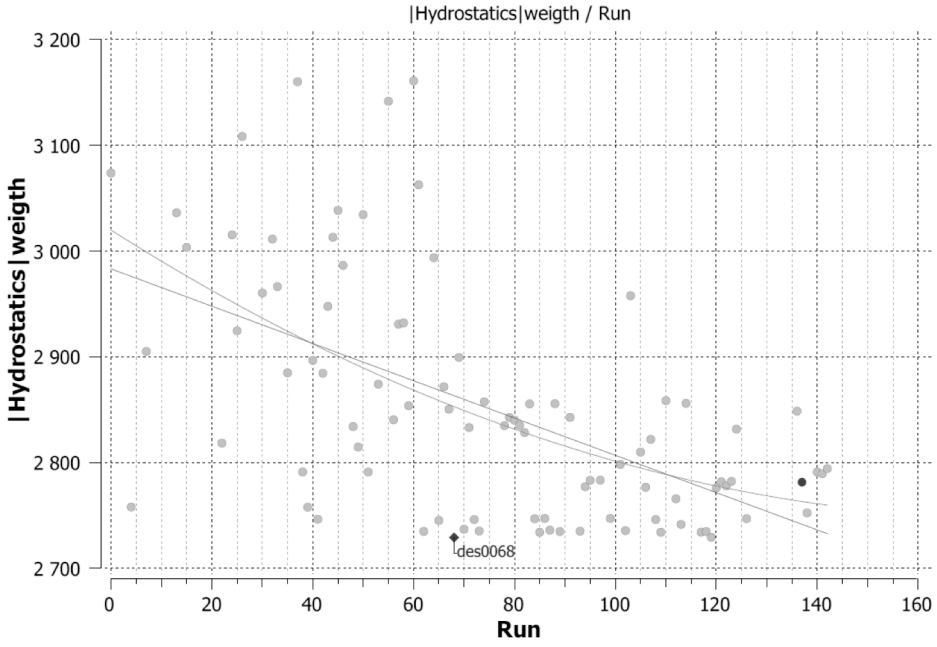
|Hydrostatics|weigth / Run
|Hydrostatics|weigth
3 200
3 100
3 000
2 900
2 800
2 700
des0068
0
20
40
60
80
100
120
140
160
Run

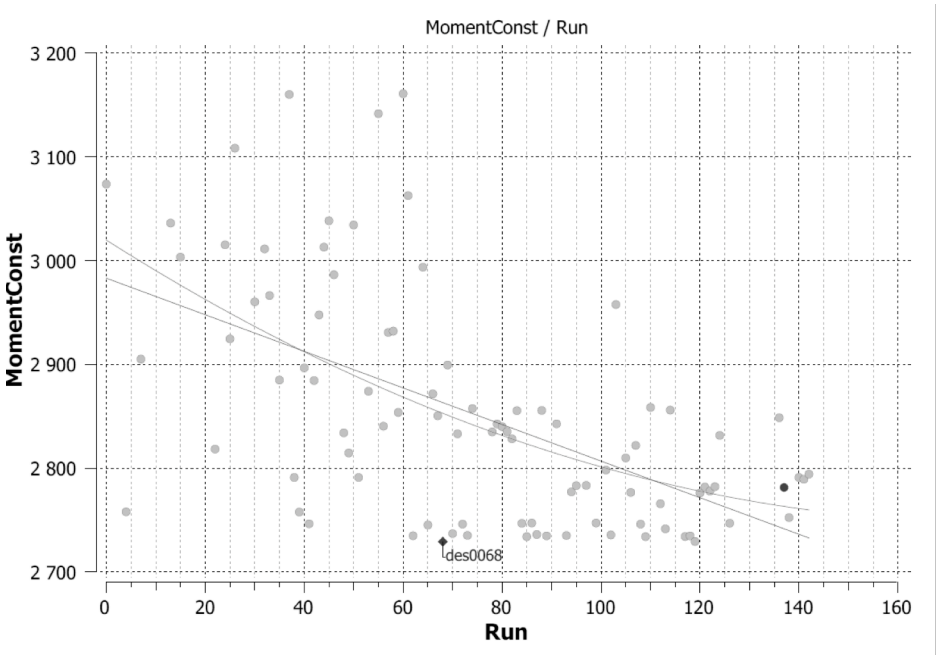
MomentConst / Run
MomentConst
Run
3 200
3 100
3 000
2 900
2 800
2 700
0
20
40
60
80
100
120
140
160
des0068